

AD_____

Award Number:
W81XWH-10-1-0506

TITLE:
Imaging Molecular Signatures of Breast Cancer with X-ray-Activated
Nanophosphors

PRINCIPAL INVESTIGATOR:
Colin M. Carpenter

CONTRACTING ORGANIZATION:
The Leland Stanford Junior University,
Stanford CA, 94305-2004

REPORT DATE: 03/2010

TYPE OF REPORT: N^A Summary Report

PREPARED FOR: U.S. Army Medical Research and Materiel Command
Fort Detrick, Maryland 21702-5012

DISTRIBUTION STATEMENT:

Approved for public release; distribution unlimited

The views, opinions and/or findings contained in this report are those of the author(s) and should not be construed as an official Department of the Army position, policy or decision unless so designated by other documentation.

REPORT DOCUMENTATION PAGE			Form Approved OMB No. 0704-0188		
Public reporting burden for this collection of information is estimated to average 1 hour per response, including the time for reviewing instructions, searching existing data sources, gathering and maintaining the data needed, and completing and reviewing this collection of information. Send comments regarding this burden estimate or any other aspect of this collection of information, including suggestions for reducing this burden to Department of Defense, Washington Headquarters Services, Directorate for Information Operations and Reports (0704-0188), 1215 Jefferson Davis Highway, Suite 1204, Arlington, VA 22202-4302. Respondents should be aware that notwithstanding any other provision of law, no person shall be subject to any penalty for failing to comply with a collection of information if it does not display a currently valid OMB control number. PLEASE DO NOT RETURN YOUR FORM TO THE ABOVE ADDRESS.					
1. REPORT DATE %>Ub`8\$%4`		2. REPORT TYPE Annual SUMMARY REPORT		3. DATES COVERED (From - To) 01Sep2010 - 31Dec2013	
4. TITLE AND SUBTITLE Imaging Molecular Signatures of Breast Cancer with X-ray-Activated Nanophosphors			5a. CONTRACT NUMBER		
			5b. GRANT NUMBER W81XWH-10-1-0506		
			5c. PROGRAM ELEMENT NUMBER		
6. AUTHOR(S) COLIN CARPENTER go cneqrk pectr gpwgtB ucphqtf Qf w'			5d. PROJECT NUMBER		
			5e. TASK NUMBER		
			5f. WORK UNIT NUMBER		
7. PERFORMING ORGANIZATION NAME(S) AND ADDRESS(ES) The Leland Stanford Junior University Stanford CA, 94305-2004			8. PERFORMING ORGANIZATION REPORT NUMBER		
9. SPONSORING / MONITORING AGENCY NAME(S) AND ADDRESS(ES) U.S. ARMY MEDICAL RESEARCH AND MATERIEL COMMAND FORT DETRICK, MARYLAND 21702-5012			10. SPONSOR/MONITOR'S ACRONYM(S)		
			11. SPONSOR/MONITOR'S REPORT NUMBER(S)		
12. DISTRIBUTION / AVAILABILITY STATEMENT APPROVED FOR PUBLIC RELEASE; DISTRIBUTION UNLIMITED					
13. SUPPLEMENTARY NOTES					
14. ABSTRACT This research program developed the foundation for Radioluminescence Imaging (RLI) and Radioluminescence Tomography (RLT) as new imaging tools for breast cancer screening and therapy monitoring. Numerous milestones were met including the development of reconstruction theory for RLI, the implementation of a software reconstruction for creating molecular images from both simulated and experimental data, instrumentation development, and demonstration of RLI in a small animal imaging cancer model. In dong so, aims 1-4 have been completed, and RLI endoscopic and full body (small animal) scanners remain as shared-resources for future ongoing research. Arising from this endeavour are several recommendations for successful research in RLI: phosphor brightness is paramount to successful imaging, as phosphors were tested that varied in light output by 3-4 orders of magnitude; control of ambient light is also paramount, and light-tight boxes are essential; multiplexing is straightforward with RLI, as emission peaks can be less than 15nm, however proper filtering is required; excitation source is very flexible, with radionuclides, x-ray sources, linear accelerators providing sufficient fluence for imaging, however, non-specific background luminescence is a confounder when very bright sources are used. In total, this project generated 12 journal publications, including 4 first author (2 more under consideration), 20 conference abstracts, and 4 courses taken. Several postdoctoral fellows are now being mentored and are working on RLI.					
15. SUBJECT TERMS BREAST CANCER, IMAGING, MOLECULAR IMAGING, X-RAY, NANOPARTICLES					
16. SECURITY CLASSIFICATION OF:			17. LIMITATION OF ABSTRACT UU	18. NUMBER OF PAGES 75	19a. NAME OF RESPONSIBLE PERSON USAMRMC
a. REPORT U	b. ABSTRACT U	c. THIS PAGE U			19b. TELEPHONE NUMBER (include area code)

Table of Contents

	<u>Page</u>
Introduction.....	4
Body.....	5
Key Research Accomplishments.....	16
Reportable Outcomes.....	17
Conclusion.....	21
References.....	22
Appendices.....	23

INTRODUCTION

Improved molecular imaging tools to further research and development and to translate into the clinic are needed to improve breast cancer disease diagnosis and treatment. Radioluminescence Imaging (RLI) / Tomography (RLT) have been developed in this grant to accomplish these goals. RLI utilizes optical light emitted from either radionuclides or radio-luminescent biologically-compatible phosphor nanoparticles (RLNPs) to produce images of molecular contrasts; these molecular contrasts are intended to provide expansive disease-specific information. This has particularly relevance for breast cancer because of the limited specificity of current breast cancer imaging tools. Because radiation sources commonly used in medicine, such as radionuclides, x-ray sources, and linear accelerators provide the excitation, RLI has the potential to function online during conventional imaging procedures or surgical procedures.

The work completed in this fellowship completed the following aims:

***Aim 1:** Select and characterize the optimal nano-scintillators for X-ray imaging in tissue*

***Aim 2:** Develop an adaptable optical imaging system, functional under X-ray irradiation, to enable the detection of emitted light from nano-scintillators. Develop the reconstruction imaging software to perform the X-ray/optical reconstruction.*

***Aim 3:** Analyze the performance characteristics of Nano-scintillator imaging with tissue-simulating phantoms. Compare to Optical Fluorescence Imaging.*

***Aim 4:** Determine the feasibility of injectable nano-scintillators in vivo.*

This grant has not only provided for extensive investigation into specific techniques, parameters, and limits of RLI as a tool to accomplish these goals, but has also led to the grantee's intensive study in molecular targeting of cancer, medical physics and radiation therapy, and an opportunity to mentor undergraduates, graduate students, and postdoctoral fellows in RLI and molecular imaging. Aims 1–4 were completed. These efforts resulted in 13 journal publications, including 5 first author (2 under consideration), 12 conference abstracts, and 8 oral presentations.

BODY

1.1. Nanophosphor characterization

To meet the milestones of Aim1, the feasibility of X-ray luminescence with Gadolinium oxysulfide particles was investigated. We examined the practical aspects of this new modality, including phosphor concentration, light emission linearity, detector damage, and spectral emission characteristics. Finally, the contrast produced by these phosphors was compared to that of X-ray fluoroscopy.

Figure 1 shows the characteristics of gadolinium (GOS) and lanthanum (LOS) oxysulfide phosphors doped with terbium (green), europium (red), thulium (NIR), and Praseodymium (NIR). These phosphors were studied, due to their anticipated brightness. Figure 1a demonstrates the GOS:Tb emission. The light emission was imaged in a clinical X-ray scanner with a cooled CCD camera and a spectrophotometer; dose measurements were determined with a calibrated dosimeter; the setup is shown in Figure 1b.

Dose to the CCD camera in the chosen imaging geometry was measured at less than 0.02cGy/sec. Emitted light was found to be linear with dose ($R^2 = 1$) and concentration ($R^2=1$), as shown in Figure 1c. Phosphor emission peaks were all less than 20nm full-width at half-maximum, and

less than 3nm full-width at half-maximum for Eu and Tb, as was expected from lanthanide dopants, as shown in Figure 1d. The minimum practical concentration necessary to detect luminescent phosphors was dependent on dose; it was estimated that sub-picomolar concentrations are detectable at the surface of the tissue with typical mammographic doses, with the minimum detectable concentration increasing with depth and decreasing with dose. In a reflection geometry, X-ray luminescence had nearly a 430-fold greater contrast to background than X-ray contrast.

The outcome of this aim was a successful demonstration and feasibility assessment of this modality using Gadolinium Oxysulfide. However, due to difficulties in making these phosphors biocompatible, the phosphor platform was switched to BaYF_4 , which may be more easily bioconjugated and tagged to molecular markers. Indeed, in a preliminary study, these phosphors were targeted to the Folate receptor (commonly expressed in breast cancer), and uptaken by live cells (data not shown).

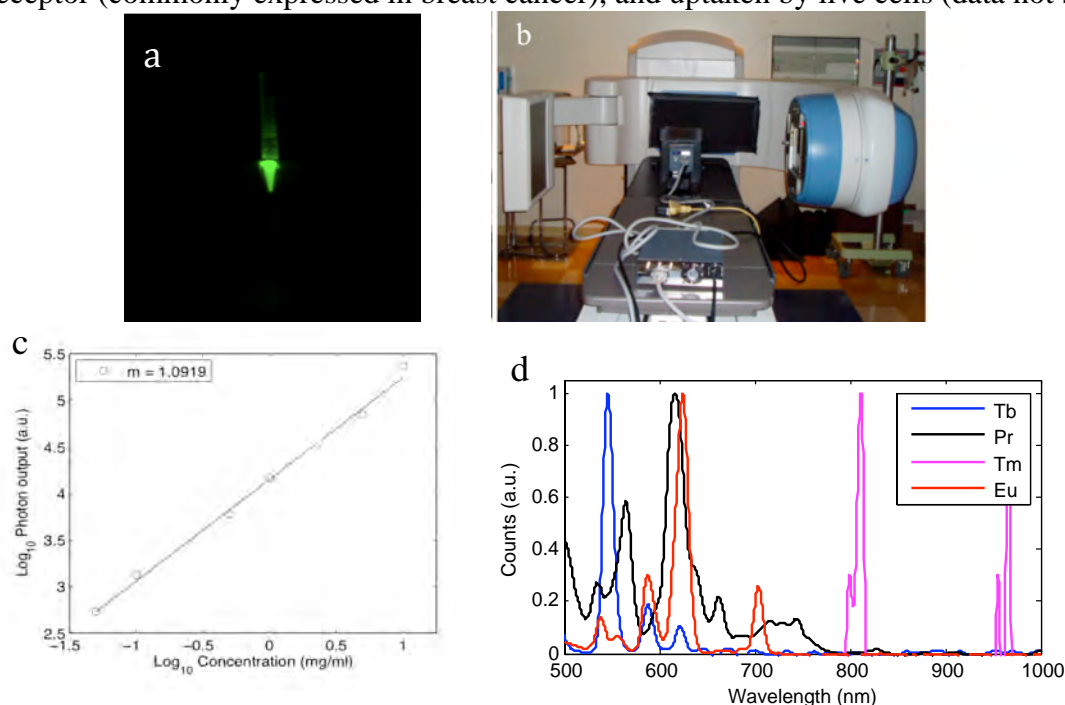


Figure 1 (a) Image of a vial of RLNP mixed with agarose excited by x-ray. (b) Excitation setup for image in (a). (c) Concentration vs. photon emission linearity. (d) Normalized emission spectra from LaOS: doped with Terbium (Tb), Praseodymium (Pr), Thulium (Tm), and Europium (Eu).

1.2: Nanophosphor characterization

In performing these tasks, the investigator was been exposed to the field of molecular imaging, a new direction for this PI. This research education was aided with participation in BioE222: Molecular Imaging, which brought together the molecular imaging faculty at Stanford to teach aspects in the hardware, chemistry, and biology of molecular imaging. In addition, the PI was exposed to nanoparticle fabrication, including the processes in making nanoparticles stable in human serum with low toxicity. Also, the PI gained knowledge in molecular targets, and the advantages and disadvantages of targeting to peptides, hormones, antibodies, affabodies, and other targeting agents. This program has been aided by working at benchside with these materials scientists, biologists, and nuclear imaging experts.

2.1: Imaging Hardware Development

Aim 2 extended the utility of Radioluminescent Imaging with the construction of a fully functioning small-animal imaging scanner, shown in Figure 2, which has full spectral and imaging capabilities to image small-animals injected with nanophosphors with high resolution. Figure 2 shows the small-animal imaging scanner, with a rod-lens installed. The system was created by repurposing a retired commercial optical imaging scanner, by adding a more sensitive camera (EM-CCD, Pro-EM, Princeton Instruments), a controllable ambient light source, and filters appropriate for RLNP phosphors.



Figure 2: Small-animal imaging box fabricated to provide proof-of-concept and aid in technique and nanoparticle

H₂O were nearly indistinguishable from the noise of about 200 counts, due to the high X-ray noise from the incident irradiation, and the dark counts from thermal noise on the CCD. After connecting the chiller and installing the leaded glass in front of the CCD lens, we then repeated the experiment with ideal settings. As shown in Figure 3, signal for the phosphor was increased by a factor of 8 over the old setup.

In addition, we improved the sensitivity of Radioluminescent Imaging by incorporating leaded glass in front of the camera, a chiller, and a filter wheel. The 3/8" thick glass sheet was custom machined (Ray-bar, Inc) to attach to our RLI imager, and attenuates the X-rays by >99.999% before they hit the CCD and cause increased noise in the pixels. Due to this improvement, we have seen a dramatic decrease in the stochastic X-ray noise in the CCD; this has enabled integration times of over 20 seconds. The liquid chiller for the CCD camera brings the CCD temperature down to -85C.

We demonstrated the improvements to the RLI system by imaging an organic phosphor (PDOT) and water (H₂O) with the old setup and the new setup. We placed the samples in our imaging box and irradiated them with 50 and 80 kVp x-rays using a superficial X-ray irradiator. For the old samples, we shut off the chiller and removed the X-ray glass. Using ideal gain and integration settings, signal for the PDOTs and

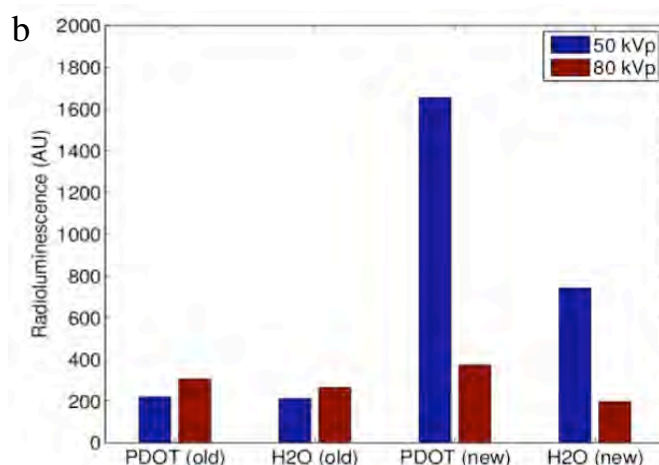
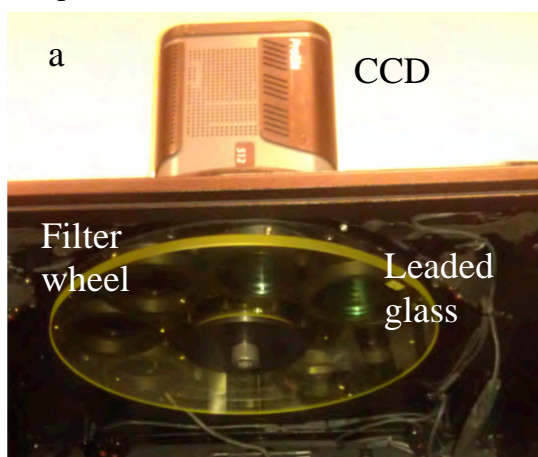


Figure 3: RLT system with improved sensitivity. (a) 3/8" thick leaded glass prevents X-ray noise from hitting the CCD, and enables longer integration times. The filter wheel enables spectral selectivity. (b) Intensity emitted from phosphors (PDOT) and water. The increase in intensity of the (new) vs (old) samples demonstrates the longer integration times possible.

2.2: Imaging Software Reconstruction Development

In addition, this aim resulted in the development of a novel algorithm which incorporated a diffuse optical photon propagation model into the reconstruction algorithm to recover unresolved dimensions in an X-ray limited angle (LA) geometry. This sophisticated technique enables such applications as image-guided surgery, where the ability to resolve lesions at depths of several centimetres, which can be the key to successful resection.

The goal of X-ray Luminescence Tomography is to determine the phosphor distribution. This spatial distribution can be determined by minimizing the difference between the measured photon flux from the camera, $\phi_M(r)$, and the simulated photon flux, $\phi_S(r)$ at identical sample locations. This is accomplished by minimizing the L2-norm of the objective function in an optimization routine:

$$\Omega = (\phi_S - \phi_M)^2$$

where Ω is the objective function to minimize. This is an underdetermined problem, as measurements are made only at the boundary. Because this problem is underdetermined, the model, G , is linearized with a Taylor approximation and formed into an iterative algorithm as:

$$G(c_i) = G(c_{i-1}) + G' \Delta c$$

where G' is the partial differential of the model with respect to the concentration, also known as the Jacobian, J . Minimizing Ω with respect to c and substituting $G(c_i)$ into ϕ_S and J for G' yields:

$$2J(G(c_{i-1}) + J\Delta c - \phi_M) = 0$$

Solving for the concentration yields:

$$\Delta c = -[J^T J]^{-1} J^T (\phi_S - \phi_M)$$

This problem is ill-posed, so it is solved using the Levenberg-Marquardt algorithm, which includes a stabilization parameter, λ , in the inversion to avoid singularities:

$$\Delta c = -[J^T J + \lambda I]^{-1} J^T (\phi_S - \phi_M)$$

This is iterated until a minima is reached (the L2 norm of the update is less than 1% of the previous iteration), or until 15 iterations are performed, whichever occurs earlier. The stabilization parameter is reduced at each iteration as the algorithm approaches the minimum and converges on the solution.

The hybrid X-ray / diffuse optical model was demonstrated in a breast-sized phantom, simulating a breast lumpectomy geometry. Both numerical and experimental phantoms were tested, with lesion-simulating objects of various sizes and depths. Results showed localization accuracy with median error of 2.2mm, or 4% of object depth, for small 2-14mm-diameter lesions positioned from 1cm to 4.5cm in depth. This compares favorably with fluorescence optical imaging, which is not able to resolve such small objects at this depth. The recovered lesion size had lower size-bias in the X-ray excitation direction than the optical direction, which was expected due to the optical scatter. However, shown in Figure 4, the technique was shown to be quite invariant in recovered size with respect to depth, as the standard deviation was less than 2.5mm. Sensitivity was a function of dose (shown in Figure 4a); radiological doses were found to provide sufficient recovery for $\mu\text{g/ml}$ concentrations, while therapy dosages provided recovery for ng/ml concentrations. Experimental phantom results agreed closely with

the numerical results, with positional errors recovered within 8.6% of the effective depth for a 5mm object, and within 5.2% of the depth for a 10mm object. Object size median error was within 2.3% and 2% for the 5mm and 10mm objects, respectively. For shallow-to-medium depth applications where optical and radio-emission imaging modalities are not ideal, such as in intra-operative procedures, this new technique, LAXLT, may be a useful tool to detect molecular signatures of disease. For this aim, the software and hardware proof-of-principle experiments were performed.

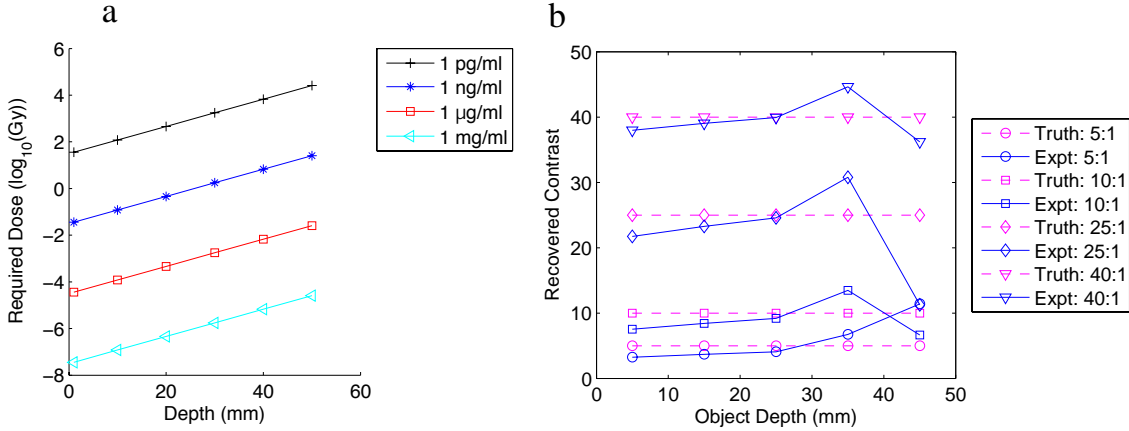


Figure 4: (a) Numerical phantom experiment examining the effect of: (a) variable object to background contrast and (b) variable concentration, of a 6mm-diameter object vs. depth from the detection plane.

2.3: Imaging Hardware Training

In performing these tasks, the investigator explored various methods of multimodality imaging, by fusing X-ray and optical photon propagation models. This work was carried out under guidance from Dr. Lei Xing, as proposed, who is an expert in X-ray modeling in tissue. A numerical photon propagation model was built, and integrated into the PI's existing code for optical photon modeling. The system development for pre-clinical imaging was a first for this PI: a small-animal system devoted to testing modality feasibility, and one that may have potential for high-resolution small-animal imaging.

2.4: Imaging Software Multiplexing Development

The ability to image multiple nanoparticle-based contrast agents simultaneously is a key advantage of RLI over other molecular imaging modalities, such as PET, and many types of fluorescence imaging. Since the radioluminescent nanoparticles emit optical light at unique wavelengths, depending on their lanthanide dopant, we are able to selectively image the unique phosphors with the use of optical filters. We demonstrated this technique by separating two distinct nanophosphor contrast agents in gelatin phantoms and a small animal phantom.

To enable multiplexed imaging, both hardware and software were developed. A filter wheel (Caliper Life Sciences, Alameda, CA) was mounted on our imager with 2 filters for 2 different phosphor nanoparticles (548nm: CaF₂:Tb, 700nm: CaF₂: Eu). Lead glass was placed above the subject. To form images of the concentrations, c , of each of these particles, the light emitted, ϕ , was recorded over the several optical spectral regions defined by filter f_1 and filter f_2 to form images of the subject, $i_1 = \phi(f_1)$ and $i_2 = \phi(f_1)$. These images, and the pre-recorded reference spectra, ϵ , for Ba_{0.55}Y_{0.3}F₂:Tb³⁺, (ϵ_{Tb}),

$\text{Ba}_{0.55}\text{Y}_{0.3}\text{F}_2:\text{Eu}^{3+}$, (ε_{Eu}), were input into a linear-least squares algorithm to extract the contributions from each nanophosphor. Reference spectra were collected with a calibrated spectrometer, thus enabling a quantitative comparison between the nanophosphors.

To validate the ability of this method to image multiple nanophosphors simultaneously, five phantoms (99% DI water, 1% agarose) were fabricated containing Tb^{3+} and Eu^{3+} doped RLNPs of linearly varying concentrations (in units of mg/ml) and mixed in the following ratios: (0:10; 2.5:7.5; 5:5; 7.5:2.5; and 10:0). Figure 5(a) displays the unmixed images for linearly increasing (top-to-bottom) amounts of Tb^{3+} -doped RLNPs on the left, and decreasing (top-to-bottom) Eu^{3+} -doped RLNPs on the right, at each concentration. The median values for each region of interest were plotted with respect to concentration. Figure 5(b) shows the median raw signal detected from each nanophosphor concentration. Figure 5(c) demonstrates this method's efficacy in separating the nanophosphors; the correlation between the samples was ($r = -0.98$).

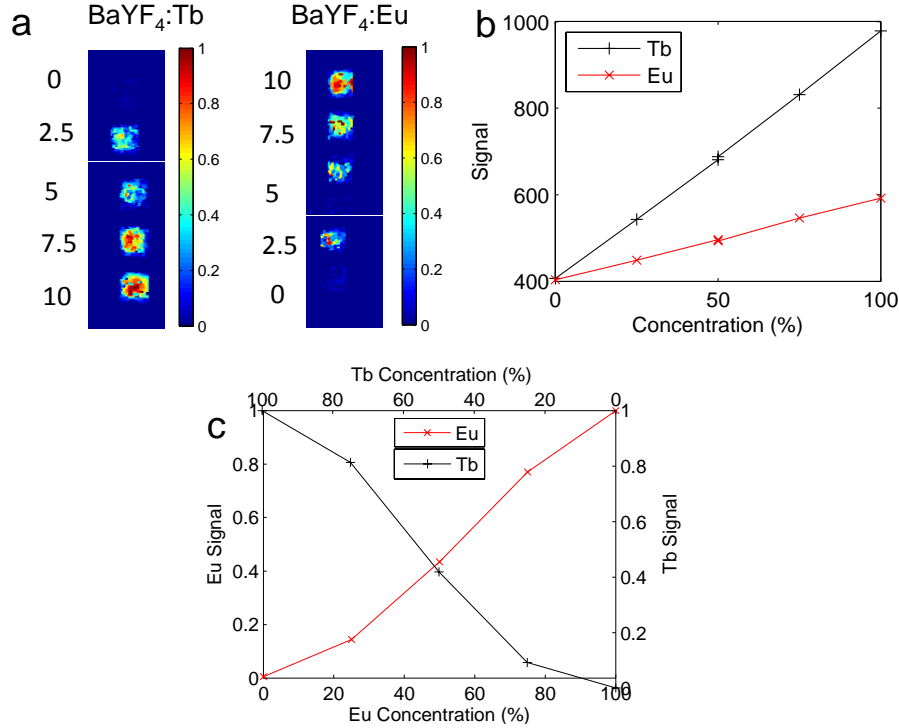


Figure 5: (a) Shown are the $\text{Ba}_{0.55}\text{Y}_{0.3}\text{F}_2:\text{Tb}^{3+}$ and $\text{Ba}_{0.55}\text{Y}_{0.3}\text{F}_2:\text{Eu}^{3+}$ phosphor concentrations with increasing/decreasing concentration (top-to-bottom) of $\text{Ba}_{0.55}\text{Y}_{0.3}\text{F}_2:\text{Tb}^{3+}$ / $\text{Ba}_{0.55}\text{Y}_{0.3}\text{F}_2:\text{Eu}^{3+}$, respectively. (b) The raw signal detected for each respective nanophosphor. (c) The relative median recovered concentration in each ROI plotted with respect to concentration.

To demonstrate this method in a pre-clinical mouse model, four batches of RLNPs were each mixed with 52 μCi (Curie) of activity of 18-F and Matrigel (BD Biosciences, Sparks, MD) and injected into both forelegs and flanks of a euthanized nude mouse, with Eu^{3+} -doped RLNPs (Eu) only on the left foreleg, Tb^{3+} -doped RLNPs (Tb) only on the left flank, an equal mixture of Eu^{3+} -doped RLNPs and Tb^{3+} -doped RLNPs (Mix) on the right flank, and an inactive undoped nanophosphor control (Ctrl) on the right foreleg. The locations of the subcutaneously injected RLNPs are shown in Figure 6(a). The feasibility of this method in a pre-clinical subject with X-ray excitation is shown in Figure 6(b)-(d). Tb^{3+} -doped RLNPs embedded in the left and right flanks are shown successfully recovered in Figure 6(b). The Eu^{3+} -doped RLNPs in the left foreleg and the right flank are shown successfully recovered in

Figure 6(c). As a control, inactive RLNPs in the right foreleg did not luminesce. Figure 6(d) shows the results of the spectral unmixing algorithm, with the Eu^{3+} -doped RLNPs shown in red, and the Tb^{3+} -doped RLNP shown in green. The yellow in the multiplexed image indicates the presence of both types of nanophosphors.

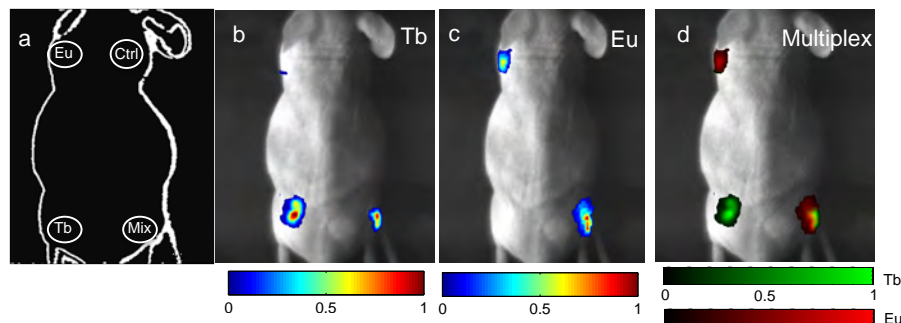


Figure 6: X-ray Luminescence: (a) Schematic of the locations of each type of RLNP. The inactive particles are indicated with the abbreviation (Ctrl). (b,c) The unmixed signal from the $\text{Ba}_{0.55}\text{Y}_{0.3}\text{F}_2\text{:Tb}$ and $\text{Ba}_{0.55}\text{Y}_{0.3}\text{F}_2\text{:Eu}$ particles, respectively. (d) The unmixed multiplexed image with colorbars for the relative concentrations of $\text{Ba}_{0.55}\text{Y}_{0.3}\text{F}_2\text{:Tb}$ and $\text{Ba}_{0.55}\text{Y}_{0.3}\text{F}_2\text{:Eu}$.

2.5: Imaging Hardware: Biopsy Needle – based RLI

Currently, biopsy is guided by X-ray fluoroscopy or ultrasound; these imaging modalities do not offer the ability to image molecular contrasts of tissue, and thus are limited in their ability to localize cancer. This shortcoming is especially true in small cancerous lesions, where structure visible by X-rays or ultrasound is not yet established; there is no current suitable means to localize cancers at this critical stage.

To meet this need, as outlined in Aim 2, a custom biopsy RLI catheter was fabricated to demonstrate proof-of-principle for phosphor image-guided biopsy procedures. The specifications were to provide a < 10 gauge imaging instrument that would fit down the needle bore. The ability to image is paramount to enable a visualization of the target mass, and to enable the search for the molecular beacon. The schematic of this instrument, shown in Figure 7, utilizes a water-cooled electron multiplied CCD (ProEM, Princeton Instruments) attached to the appropriate 4:1 magnification lenses (35mm and 8mm, Edmunds Optics, Megapixel) to project the proximal end of a leached fiber bundle (Schott, Inc.) onto the full CCD field of view. This fiber bundle is protected by a heat shrink catheter made of PTFE to prevent kinking and breaking of the individual fibers.

Images of the detection hardware and lens-coupled fiber are shown in Figure 8. The biopsy imaging system was tested for focus by imaging a business card under white-light illumination; an example image is shown in Figure 8c.

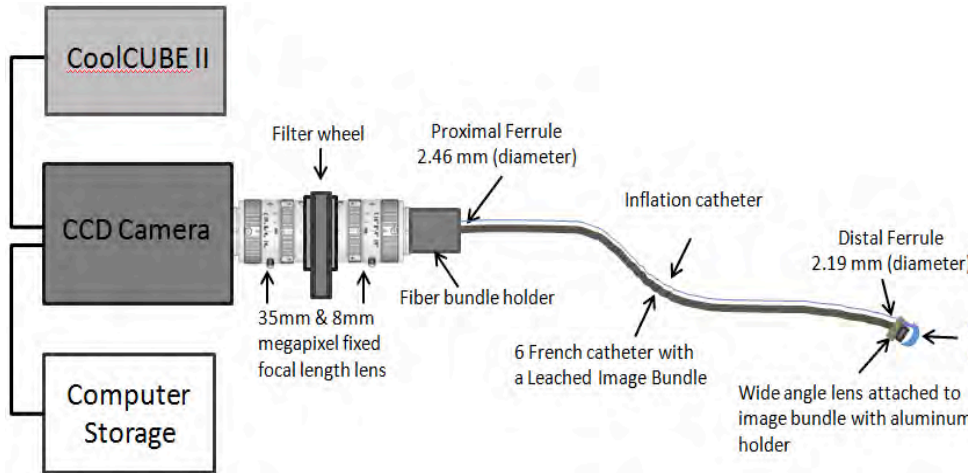


Figure 7: Schematic of the RLI biopsy device, consisting of a cooled CCD, a filter wheel for multiplexing ability, and a lens at the distal tip.

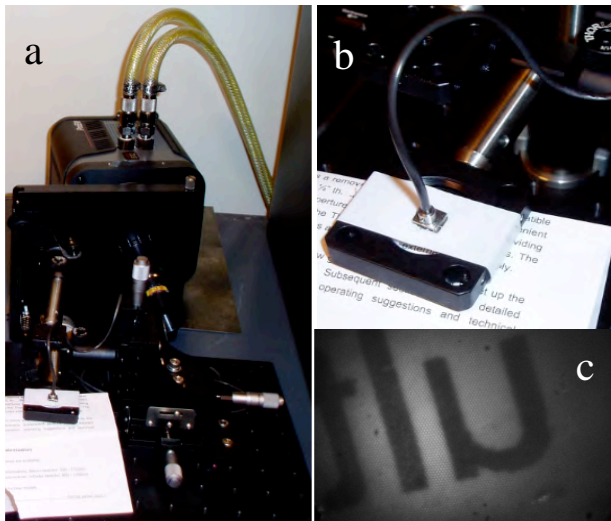


Figure 8: (a,b) Photographs of the Radioluminescent Biopsy Imaging device, specifically of (a) the CCD camera, filter wheel, and coupling optics; (b) a close-up of the distal tip of the catheter. (c) white-light image of text from a business card taken with the RLI biopsy device.

2.6: Imaging Hardware: RLI Endoscopy

With a similar goal for interventional imaging, a larger bore fiber-based system was built utilizing an imaging optical fiber coupled to a highly sensitive ICCD camera. This system had a larger aperture, and thus was more sensitive to Radioluminescence. Images of the system are shown in Figure 9 a-b. A cartoon of the application of this system for surgical oncology guidance is detailed in Figure 9c. Specifically, a micro-imaging lens (Schneider Cinegon, F/1.4, 12mm focal length) was coupled at the distal end of an optical imaging fiber bundle that was 108 mm long, with a 5×6.7 mm active area. The pixels of the fiber bundle are made of discrete $10\mu\text{m}$ fibers (Schott, IG154). At the proximal end, a Pentax (F/1.4) lens provided relay optics to the camera. The camera, an image-intensified CCD (Stanford Photonics Inc., Turbo 640-Z), had 640×480 pixels and single-photon imaging capability. To minimize background light and to emulate a light-tight anatomical cavity, all images were taken in a dark box. In addition, images were post-processed with a software thresholding technique that removed

pixel values below a manufacturer-recommended value; this optimal value was chosen to remove low-intensity pixels which corresponded to thermal and read noise on the CCD. These steps reduced the noise to ~20 counts per second.

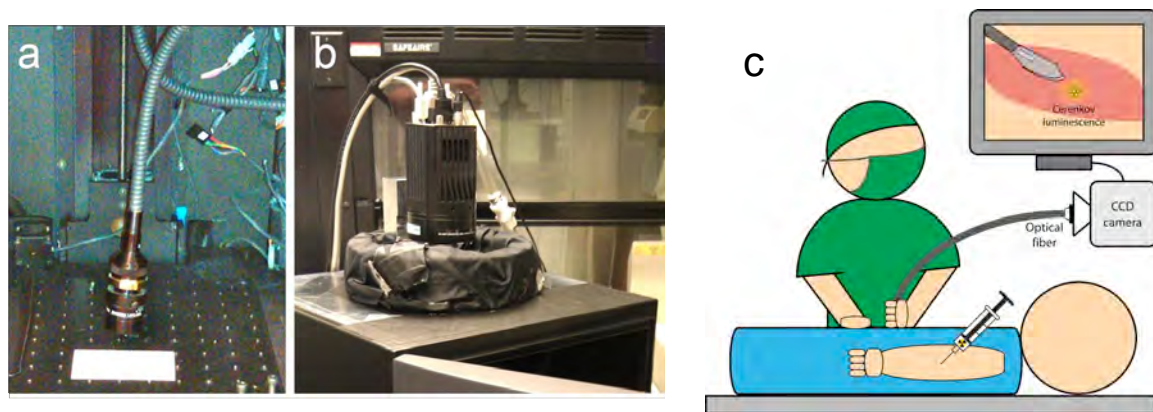


Figure 9. A prototype of fiber based system for endoscopic and laparoscopic Cerenkov Luminescence Imaging applications. An optical fiber with micro-imaging lens (a) was coupled to an image-intensified CCD (b). (c) A suggested application for the fiber based system for endoscopic and laparoscopic Radioluminescence Imaging.

We investigated the feasibility of RNLP-free Radioluminescence Imaging with the interventional system shown in Figure 10 for guiding cancer imaging by performing spatial resolution, sensitivity, and proof-of-concept experiments.

The spatial resolution of the system was characterized using a standard PET/SPECT phantom (Micro Hot-spot phantom, Data Spectrum Corporation, Hillsborough, NC) filled with 15.2 MBq (410 μ Ci) of ^{18}F -FDG; this phantom is also commonly used to evaluate the spatial resolution of PET systems. Both the 2.4 and 1.6 mm cylindrical holes were used to form line profiles, taken from the fiber-based images. Two images were acquired: an ambient-light image, and a functional CLI image. The exposure time for all ambient images was <1 sec, while the functional image acquisition time was 5 minutes. The subject was located 5cm from the optical system. The photographic and Cerenkov images taken using the standard optical imaging system are similar to the photographic and Cerenkov images taken with the fiber-based system (Figure 10A). The line profiles demonstrate a high correlation between the Cerenkov and photographic line profiles. For the 2.4 mm holes (Figure 10B), the line profile limits depicted by the large green stars in Figure 10A, had a Pearson correlation coefficient of $r = 0.78$ (significance: $p < 1e-5$). For the 1.6 mm holes, the line profile limits depicted by the smaller red stars, the correlation between the line profiles of $r = 0.71$ (significance: $p < 1e-5$). The peaks were also in near identical locations; the difference in peak locations between the holes for the line profiles of the photographic and Cerenkov-emission images was 3.8%, a difference of only a few pixels.

Figure 10F shows the reduction in signal during ^{18}F -FDG decay over time for two wells: one filled with ^{18}F -FDG, and one filled with a water/glycerol mixture only. With a 5 min integration time, a minimum of ~45 KBq (1.21 μ Ci) of activity can be identified as different than the control well containing the water/glycerol solution (signal to noise ratio > 1). Note the decrease in signal in the control well; this change in signal was due to stray gamma photons from the ^{18}F -FDG well interacting with the optical fiber and creating scintillation background light in the image.

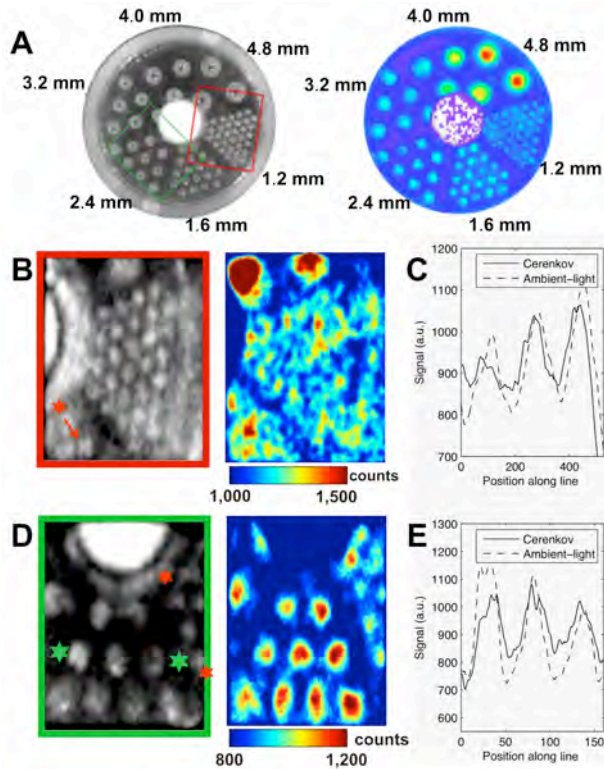
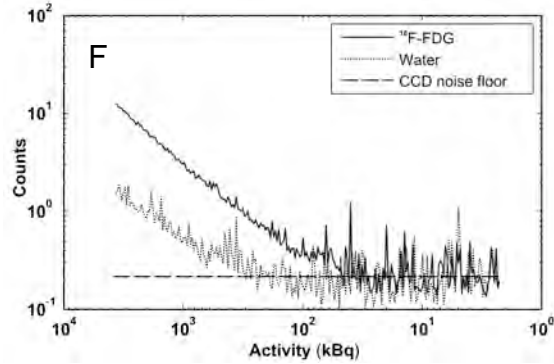


Figure 10. Characterization of the fiberscopic system spatial resolution. (A) Respective ambient (left) and Radioluminescence images (right) of a (4.3 cm inner diameter phantom). (B-E) Quantitative line profiles of the ambient and Cerenkov images for the 1.6mm & 2.4mm holes, respectively; the line sampled is indicated by the boxes in (A). (F) Sensitivity with FDG.



2.7: Imaging Hardware Development

In performing these tasks, the investigator gained valuable training in optical systems and catheter-based devices. This experience will be useful for future device development. In addition, the investigator gained valuable experience in working with small-animal phantoms (post-mortum) for more biologically appropriate phantom demonstration, where the tissue properties and geometries match that of the living subjects.

3.1: Imaging Hardware Development: Sensitivity Comparison

Towards meeting aim 3, we investigated the sensitivity of RLI and compared it to the current state-of-the-art in fluorescence molecular imaging. To capture sensitivity for the RLI system, we imaged decreasing concentrations of CaF₂:Eu, coated with Au, phosphor mixed with 1% agar. As shown in Figure 11a, we were able to linearly recover concentrations of phosphor to 10 μ g/ml, or about 15nM. This compares favourably to fluorescence imaging, shown in Figure 11b [1], which has a sensitivity limitation of about 5nM.

However, RLI can be improved. As is apparent in Figure 11a, our investigations have uncovered a potential limit to sensitivity. While irradiating water-soluble phosphor samples, we discovered that X-rays create optical luminescence in water [2,3], which has been attributed to hydroxide radicals and hydrated electrons in the literature. This signal adds background signal to RLI, potentially limiting sensitivity to 20 μ g/ml, or 30nM, as shown below.

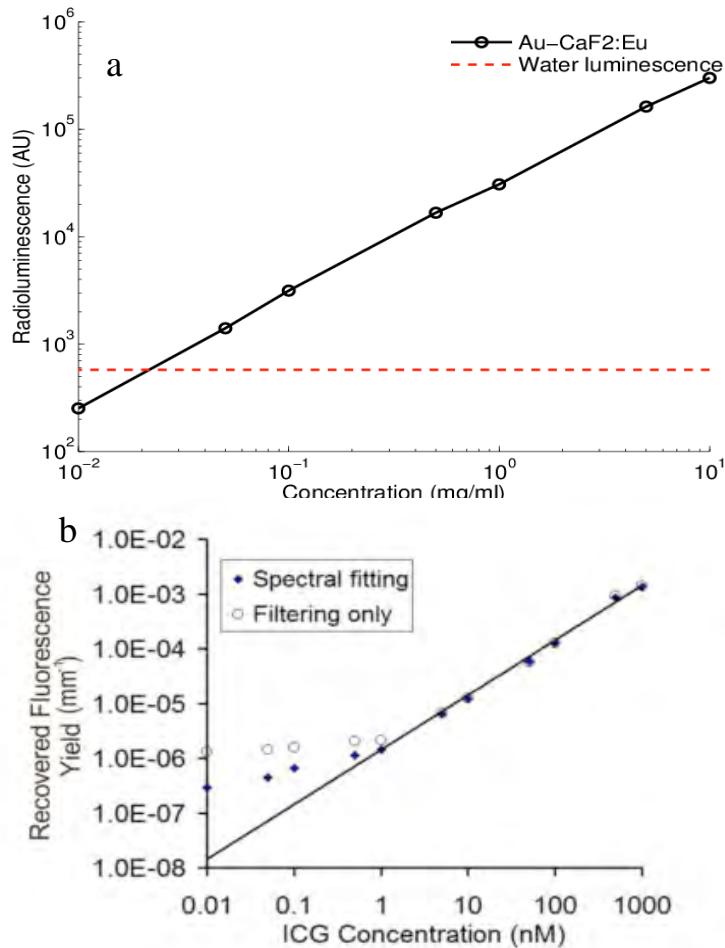


Figure 11: (a) Sensitivity of Radioluminescence imaging. The signal from several phantoms with concentrations ranging from 10 μ g/ml to 10 mg/ml is shown in black. The background water luminescence is shown in red. (b) Sensitivity of fluorescence imaging for two different filtering strategies (from [1]). The fluorescence sensitivity is limited by the autofluorescence in the tissue, or in this case, the autofluorescence of lipid in the intralipid / Indocyanine green phantom.

4.1: Feasibility of injectable nano-scintillators in vivo

Significant effort was dedicated to RLNP Radioluminescence Imaging; work is ongoing. Due to the difficulty in fabricating biocompatible, stable nanoparticles, progress was hindered. In addition, during our investigation of illumination sources, we noticed that the light emitted from injected FDG was nearly as bright as that from RLI nanoparticles (see Figure 12), depending on the efficiency of the nanophosphor. After literature investigation, it emerged that the light emitted from the radiotracer was Cerenkov light. As shown in Figure 12, the Cerenkov light was able to be unmixed from the RLNP signal. Thus, an investigation into the utility of Radioluminescence (Cerenkov) imaging for interventional imaging was launched, utilizing the same instrumentation designed for RLNP imaging. We believe that RLNP-free RLI imaging has significant potential in several niche clinical applications, such as surgical guidance for the removal of breast cancer. Below are our investigations into RLNP-free RLI.

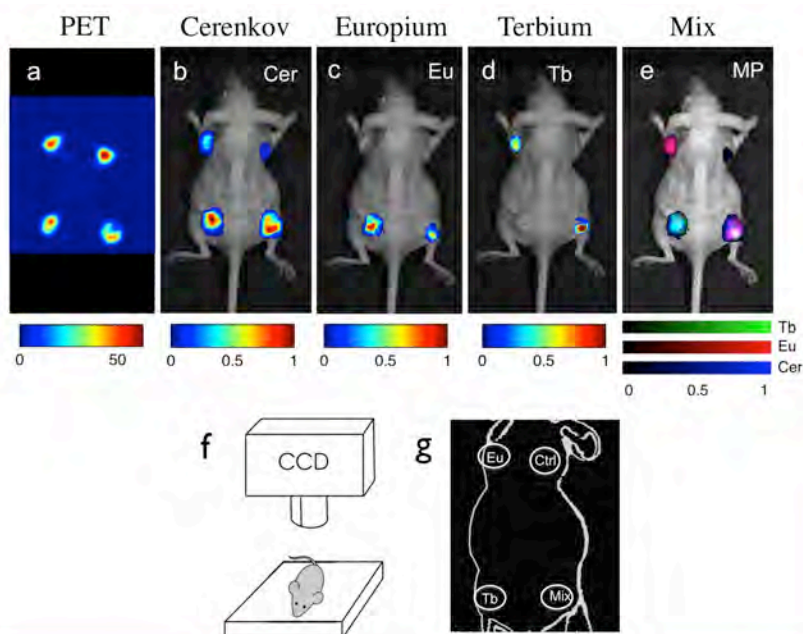


Figure 12: X-ray Luminescence: (a) Schematic of the locations of each type of RLNP. The inactive particles are indicated with the abbreviation (Ctrl). (b,c) The unmixed signal from the $\text{Ba}_{0.55}\text{Y}_{0.3}\text{F}_2\text{:Tb}$ and $\text{Ba}_{0.55}\text{Y}_{0.3}\text{F}_2\text{:Eu}$ particles, respectively. (d) The unmixed multiplexed image with colorbars for the relative concentrations of $\text{Ba}_{0.55}\text{Y}_{0.3}\text{F}_2\text{:Tb}$ and $\text{Ba}_{0.55}\text{Y}_{0.3}\text{F}_2\text{:Eu}$.

4.2: Feasibility of RLNP-free Radioluminescence imaging

For this investigation, we studied the feasibility of RLNP-free Radioluminescence Imaging with the interventional system shown in Figure 13 for guiding in-vivo cancer imaging. Specifically, ^{18}F -FDG was produced by Radiochemistry Facility at Stanford University (Stanford, CA). Rat glioma cell line C6 was obtained from American Type Culture Collection (Manassas, VA). Female athymic nude mice (nu/nu) (N=5) obtained from Charles River Laboratories, Inc. (Cambridge, MA) were 4-6 weeks of age. A CRC-15R PET dose calibrator (Capintec Inc., Ramsey, NJ) was used for all radioactivity measurements. All animal studies were carried out in compliance with federal and local institutional guidelines for the conduct of animal experimentation. C6 cells were cultured in DMEM medium supplemented with 10% fetal bovine serum (FBS) and 1% penicillin/streptomycin (Invitrogen Life Technologies, Carlsbad, CA). The cell line was maintained in a humidified atmosphere of 5% CO_2 at 37°C , with the medium changed every other day. A 75% confluent monolayer was detached with trypsin and dissociated into a single cell suspension for further cell culture. Approximately 1×10^6 C6 cells suspended in phosphate buffered saline (PBS, 0.1M, pH=7.2, Invitrogen, Carlsbad, CA) were implanted subcutaneously in the left legs of nude mice. Tumors were allowed to grow to a size of 150 to 200 mm^3 (2-3 weeks), and the tumor-bearing mice were imaged *in vivo*. Validation was performed with an IVIS Spectrum system (Caliper Life Science, Hopkinton, MA). For all *in vivo* studies, radionuclides were diluted in PBS. Animals were placed in a light-tight chamber under isoflurane anesthesia. Each acquisition took 3 min for all studies without filters. Images were acquired and analyzed using Living Image 3.0 software (Caliper life sciences, Hopkinton, MA). The mice were fasted overnight prior to ^{18}F -FDG imaging and kept anesthetized by inhalation of 2% isoflurane during the experiment.

The RLI images comparing both systems before removal of the tumor for mouse 1 are shown in Figure 13; the IVIS system produced Figures 13A, while the fiber-based CLE system produced Figures 13B. Comparing images in Figure 13B quantitatively, the Cerenkov signal in the tumor to background for the excised tumor tissue for the fiber-based CLE system was determined by computing a ratio between the median value in the region of interest (ROI) encircling the tumor to the median value in the cleared tumor cavity. For the removed tumor, the tumor-to-background was 1.28 (for comparison, the

tumor-to-background in the IVIS was 1.16 for the 3 minute scan). For Mouse 2-5, the tumor-to-background for the removed tumor was 1.41, 1.21, 1.02, and 1.17, respectively. Tumor tissue light emission was significantly higher than the exposed cavity for all mice (Student t-test for paired samples, $p < 0.05$ for all). Much of the low tumor-to-background value in Mouse 4 can be explained by the reflection of the light emitted from the tumor by the tumor cavity which was directly adjacent. Residual tumor tissue after surgery is also possible.

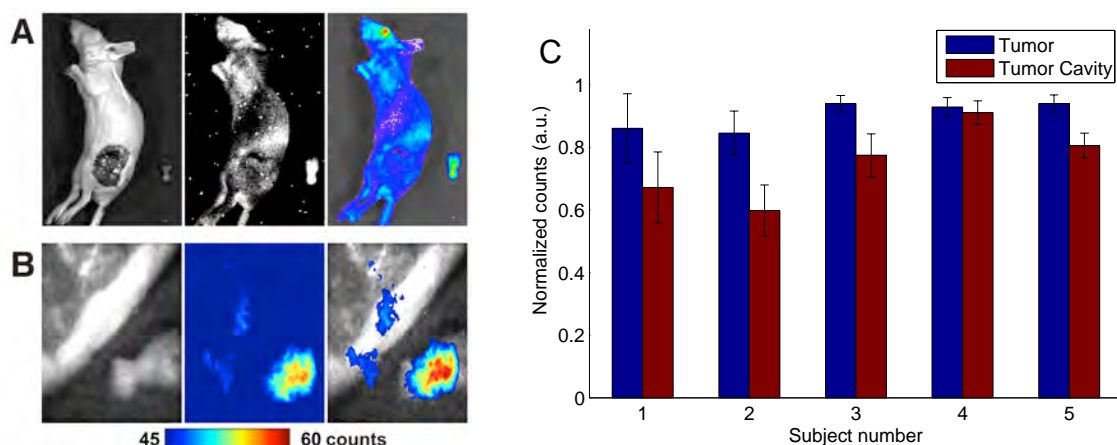


Figure 13. Mouse 1 imaged by (A) the IVIS optical system, consisting of an ambient-light image (left), the luminescent image (middle), and the fused image (right); and (B) fiber based system after surgery to remove tumor tissues, consisting of an ambient-light image (left), the luminescent image (middle), and the fused image (right). (C) Comparison of tumor to background for all mice in the study.

4.3: Small-Animal in-vivo Imaging Training

In performing these tasks, the investigator gained valuable training in handling small-animal mouse models and performing in-vivo experiments. This experience will be useful for future molecular imaging ventures.

KEY RESEARCH ACCOMPLISHMENTS

- Established the feasibility of Radioluminescent Tomography in reflection mode.
- Developed a hybrid X-ray/Optical photon propagation model to perform high resolution Radioluminescent Tomography, in an appropriate geometry for Intraoperative Radiation Therapy.
- Characterized nanophosphors suitable for RLT, including Gadolinium oxysulfide and Barium Yttrium Fluoride.
- Fabricated a small-animal pre-clinical RLT imaging box to enable automated, controlled, RLT experiments.
- Improved instrumentation through leaded glass and emission filters to enable sensitivity of Radioluminescent Imaging to 30 nM.

- Developed strategy to remove water-luminescent component to improve sensitivity.
- Demonstrated multiplexing ability of RLI in phantoms and small animal phantoms, and completed both hardware and software requirements.
- Fabricated two imaging fiber-based RLI systems, including a biopsy system and a hand-held system to demonstrate proof-of-concept.
- Fully characterized an RLNP-free RLI (Cerenkov) imaging system in terms of sensitivity and spatial resolution.
- Demonstrated RLNP-free RLI (Cerenkov) imaging in successfully removing cancerous tissue from a small-animal mode.

REPORTABLE OUTCOMES:

12 journal publications; 20 conference abstracts, and 9 conference presentations; several postdoctoral fellows are now being mentored and working in RLI; 4 courses taken, including BioE222: Molecular Imaging, Med374: Medical Device Design (taken after the grant was accepted, before it was funded), the Comprehensive Cancer Training Program, and SIE: The Stanford Institute for Entrepreneurs, and 3 patent applications.

Publications resulting from this fellowship:

	Authors	Publication	Volume	Number	Pages	Year
1	Carpenter, CM; Sun, C; Pratx, G; Xing, L;	Medical Physics	40	6	400-400	2013
2	Pratx, Guillem; Chen, Kai; Sun, Conroy; Axente, Marian; Sasportas, Laura; Carpenter, Colin; Xing, Lei;	Journal of Nuclear Medicine	54	10	1841-1846	2013
3	Xiang, L; Ahmad, M; Carpenter, C; Pratx, G; Nikoozadeh, A; Khuriâ€ Yakub, B; Xing, L;	Medical Physics	40	6	522-522	2013
4	Xiang, Liangzhong; Han, Bin; Carpenter, Colin; Pratx, Guillem; Kuang, Yu; Xing, Lei;	SPIE BIOS			85811I-85811I-7	2013

5	Carpenter, C; Liu, H; Sun, C; Pratx, G; Chang, Z; Xing, L;	International Journal of Radiation Oncology* Biology* Physics	84	3	S869	2012
6	Carpenter, C; Sun, C; Pratx, G; Chen, K; Senadheera, L; Xing, L;	Medical Physics	39	6	3888-3888	2012
7	Carpenter, Colin M;					2012
8	Carpenter, Colin M; Sun, Conroy; Pratx, Guillem; Liu, Hongguang; Cheng, Zhen; Xing, Lei;	Optics express	20	11	11598-11604	2012
9	Liu, Hongguang; Carpenter, Colin M; Jiang, Han; Pratx, Guillem; Sun, Conroy; Buchin, Michael P; Gambhir, Sanjiv S; Xing, Lei; Cheng, Zhen;	Journal of Nuclear Medicine	53	10	1579-1584	2012
10	Liu, Hongguang; Carpenter, Colin M; Jiang, Han; Pratx, Guillem; Sun, Conroy; Buchin, Michael P; Gambhir, Sanjiv S; Xing, Lei; Cheng, Zhen;	ABSTRACTS OF PAPERS OF THE AMERICAN CHEMICAL SOCIETY	243			2012
11	Pratx, Guillem; Chen, Kai; Sun, Conroy; Martin, L; Carpenter, C;	International Journal of Radiation Oncology*	84	3	S668	2012

	Xing, L;	Biology* Physics				
12	Pratx, Guillem; Chen, Kai; Sun, Conroy; Martin, Lynn; Carpenter, Colin M; Olcott, Peter D; Xing, Lei;	PloS one	7	10	e46285	2012
13	Xiang, Liangzhong; Han, Bin; Carpenter, Colin; Pratx, Guillem; Kuang, Yu; Xing, Lei;	Medical physics	40	1	10701	2012
14	Carpenter, CM; Pratx, G; Sun, C; Liu, H; Xing, L;	Medical Physics	38	6	3836-3836	2011
15	Carpenter, CM; Pratx, G; Sun, C; Xing, L;	Physics in medicine and biology	56	12	3487	2011
16	Carpenter, CM; Pratx, G; Sun, C; Xing, L;	International Journal of Radiation Oncology* Biology* Physics	81	2	S90	2011
17	Carpenter, Colin M; Xing, Lei; Pratx, Guillem; Sun, Conroy Ghin Chee;					2011
18	Carpenter, Colin M; Xing, Lei; Sun, Conroy Ghin Chee; Pratx, Guillem;					2011
19	Kuang, Y; Pratx, G; Sun, C; Carpenter, C; Xing, L;	Medical Physics	38	6	3746-3746	2011
20	Pratx, G;	Medical	38	6	3836-3836	2011

	Carpenter, C; Sun, C; Xing, L;	Physics				
21	Sun, Conroy; Carpenter, Colin; Pratz, Guillem; Xing, Lei;	Nanoscale Res. Lett	6		24	2011
22	Sun, Conroy; Carpenter, Colin; Pratz, Guillem; Xing, Lei;	Nanoscale research letters NRL	2011			2011
23	Sun, Conroy; Pratz, Guillem; Carpenter, Colin M; Liu, Hongguang; Cheng, Zhen; Gambhir, Sanjiv Sam; Xing, Lei;	Advanced Materials	23	24	H195-H199	2011
24	Carpenter, CM; Pratz, G; Sun, C; Xing, L;	International Journal of Radiation Oncology* Biology* Physics	78	3	S91-S92	2010
25	Carpenter, CM; Pratz, G; Sun, C; Xing, L; Ravilisetty, P;	Medical Physics	37	6	3437-3437	2010
26	Carpenter, CM; Sun, C; Pratz, G; Rao, R; Xing, L;	Medical physics	37	8	4011-4018	2010
27	Carpenter, Colin M; Senadheera, Lasitha; Pratz, Guillem; Sun, Conroy; Ravilisetty, Padmanabha R; Xing, Lei;	Biomedical Optics			BTuE5	2010
28	Pratz, G; Carpenter, C;	Medical Physics	37	6	3357-3358	2010

	Sun, C; Xing, L;					
29	Pratx, G; Carpenter, CM; Sun, C; Rao, R; Xing, L;	International Journal of Radiation Oncology* Biology* Physics	78	3	S641-S642	2010
30	Pratx, Guillem; Carpenter, Colin M; Sun, Conroy; Rao, Ravi P; Xing, Lei;	Optics letters	35	20	3345-3347	2010
31	Pratx, Guillem; Carpenter, Colin M; Sun, Conroy; Xing, Lei;	Medical Imaging, IEEE Transactions on	29	12	1992-1999	2010
32	Sun, C; Liu, H; Pratx, G; Carpenter, C; Xing, L; Cheng, Z;	Medical Physics	37	6	3358-3358	2010
33	Sun, CG; Ravilisetty, P; Carpenter, C; Pratx, G; Xing, L;	International Journal of Radiation Oncology* Biology* Physics	78	3	S653	2010

CONCLUSION

This grant has enabled the grantee to focus on the task of developing, characterizing, and implementing new molecular imaging strategies, and perform imaging *in vivo*. In particular, the Radioluminescence Imaging modality was thoroughly investigated. The incorporation of hardware and software innovations has resulted in high sensitivity which is demonstrated as suitable for small animal imaging. The additional innovation of multiplexed imaging methods will aid the research and development of RLI of RLNPs, by enabling multiple molecular targets to be simultaneously imaged. In addition, this funding period has resulted in experience in mentoring other fellows.

The research and training completed are significant for the eradication of breast cancer, and for training for future novel tools for early detection of breast cancer. The coursework and experience

gained by this PI will be critical in his goal to translate breast cancer treatment technology into the clinic.

REFERENCES

[1] Davis, SC, “Diffuse Tomography of Absorbing Fluorescent Optical Exogenous Contrast Guided by Simultaneously Acquired Magnetic Resonance Images,” Thesis, Dartmouth College Thayer School of Engineering, 2008.

[2] Quickenden, TI and Que Hee, SS. “The Luminescence of Water Excited by Ambient Ionizing Radiation,” Radiation Research, 46 (1) 1971.

[3] Tarasov, MD., El'yash, SL., Goncharova, VF., Petrushin, ON., Savel'ev, YA., Tarakanov, MY., Shigaev, YS. “Efficiency of Radioluminescence of Water under the Action of Accelerated Electrons,” Instruments and Experimental Techniques, 50(6), 1997.

APPENDIX

**Limited-Angle X-ray Luminescence Tomography: Methodology and Feasibility
Study**

CM Carpenter¹, G Pratz¹, C Sun¹, and L Xing¹

*¹Department of Radiation Oncology, School of Medicine, Stanford University, Stanford,
CA USA 94305*

(Email: colincarpenter@stanford.edu)

Short Title: Limited Angle X-ray Luminescence Tomography

PACS Codes: 41.50.+h, 42.25.Dd, 87.85.Rs

Abstract:

X-ray Luminescence Tomography (XLT) has recently been proposed as a new imaging modality for biological imaging applications. This modality utilizes phosphor nanoparticles which luminesce near-infrared light when excited by X-ray photons. The advantages of this modality are that it uniquely combines high sensitivity of radioluminescent nanoparticles and high spatial localization of collimated X-ray beams. Currently, XLT has been demonstrated using X-ray spatial encoding to resolve the imaging volume. However, there are applications where the X-ray excitation may be limited by geometry, where increased temporal resolution is desired, or where a lower dose is mandatory. This paper extends the utility of XLT to meet these requirements by incorporating a photon propagation model into the reconstruction algorithm to recover dimensions remaining in an X-ray limited angle (LA) geometry. This enables such applications as image-guided surgery, where the ability to resolve lesions at depths of several centimeters can be the key to successful resection. The hybrid X-ray / diffuse optical model is first formulated and then demonstrated in a breast-sized phantom, simulating a breast lumpectomy geometry. Both numerical and experimental phantoms are tested, with lesion-simulating objects of various sizes and depths. Results show localization accuracy with median error of 2.2mm, or 4% of object depth, for small 2-14mm-diameter lesions positioned from 1cm to 4.5cm in depth. This compares favorably with fluorescence optical imaging, which is not able to resolve such small objects at this depth. The recovered lesion size has lower size-bias in the X-ray excitation direction than the optical direction, which is expected due to the increased optical scatter. However, the technique is shown to be quite invariant in recovered size with respect to depth, as the standard deviation is less than 2.5mm. Sensitivity is a function of dose; radiological doses are found to provide sufficient recovery for $\mu\text{g/ml}$ concentrations, while therapy dosages provide recovery for ng/ml concentrations. Experimental phantom results agree closely with the numerical results, with positional errors recovered within 8.6% of the effective depth for a 5mm object, and within 5.2% of the depth for a 10mm object. Object size median error is within 2.3% and 2% for the 5mm and 10mm objects, respectively. For shallow-to-medium depth applications where optical and radio-

emission imaging modalities are not ideal, such as in intra-operative procedures, LAXLT may be a useful tool to detect molecular signatures of disease.

1. Introduction

Imaging plays a vital role in the management of cancer care, for detection, staging, intervention, and monitoring of treatment response. Despite its ubiquitous use elsewhere, the role of imaging in surgery is limited, as it is dominated by C-arm fluoroscopy and optical endoscopy. These tools are appropriate for visualizing tissue structure, yet are limited in their sensitivity to microscopic disease. This limitation affects such procedures as surgical breast lumpectomy, as many studies have found that surgeons are unable to remove all tumor tissue present in the surgical field (for example, Gibson et al. identified residual tumor in 55% of the cases[1]). The risks of local failure are high, as local failure often leads to distant metastasis [2]. Thus, there is a need for tools to provide surgeons with more sensitive, more specific image-guidance.

This need may be fulfilled with molecular imaging, which promises to image molecular and cellular processes, and may allow the early identification of disease or status of disease progression and treatment [3]. Developing these tools for the operating room would aid a physician during an intervention, by allowing the clinician to identify near-microscopic regions of disease, such as at the tumor margin. Ideally, this tool would be able to image at a depth of several centimeters, so that disease buried beneath the superficial layers could be identified. Several potential applications for this technology could be in removing occult disease in breast[4, 5], brain[6] and hepatic tumors[7], where imaging is currently being incorporated into the clinic, and new innovations may be readily translated.

This paper develops and demonstrates a novel X-ray Luminescence Tomographic (XLT) method that is uniquely suited for image-guided surgical applications. This method, Limited-Angle XLT (LAXLT), utilizes a photon propagation model to enable XLT for surgical guidance, where XLT's advantages are the clearest for translation into the clinic. XLT has been recently introduced[8] and demonstrated in simulation and in phantoms [9, 10]. This imaging modality utilizes nano-sized phosphors which emit optical near-infrared light upon X-ray excitation [11, 12]. Attaching these phosphors to

molecular probes (e.g. antibodies and peptides) that target molecular markers specific to tumors, such as angiogenesis markers like epidermal growth factor receptor[13], or $\alpha_v\beta_3$ -integrin [14, 15] expression could allow the surgeon to differentiate between normal and cancerous tissue. XLT has several advantages to current molecular-sensitive imaging modalities: emission imaging techniques, such as gamma cameras, are limited in their ability to discriminate depth due to the limited angles that may be imaged during surgical procedures[16]; optical imaging, on the other hand, has the ability to provide depth localization, and is currently under investigation for surgical guidance [6, 4, 17], yet is limited in its ability to image deeper than $\sim 1\text{cm}$ [18]. Depth is important to discern to determine occult lesions lying under the superficial layer, and to determine the feasibility of surgical removal of a lesion.

XLT utilizes the extremely low-scatter of X-rays compared to optical fluorescence imaging to enable higher spatial resolution. A thin pencil-beam of collimated X-rays may be maintained while the X-rays propagate through tissue of several cm; this spatial localization is in contrast to optical excitation, which is highly attenuated and scattered[19]. By rotating the X-ray (or similarly the phantom) to cover all angular projections, the resolving power is limited merely by the width of the beam (up to the diffraction of the X-ray). A numerical analysis demonstrated that 2.25cm deep objects as small as 1mm (using a 1mm beam width) with a nanoparticle concentration of 0.4pM could be resolved; increasing dose increased the sensitivity[9]. However, there are applications where the X-ray excitation may be limited by geometry, where increased temporal resolution is desired, or where a lower dose is mandatory; one such application is intraoperative breast cancer lumpectomy, where it may not be possible or desirable to irradiate over the full projection space. In these cases, it would be beneficial to irradiate over a limited projection space, and use the ability of the optical detectors to resolve the remaining dimensions. This technique could also have utility in decreasing dose to the tissue, as fewer irradiation beamlets are needed to resolve the volume.

This paper develops a reconstruction methodology for utilizing XLT to perform depth-resolved imaging in a geometry appropriate for tumor-resection applications. This method develops a hybrid X-ray/optical reconstruction, which allows XLT spatial encoding in a limited angle geometry, and diffuse optical spatial discrimination for the

remaining dimensions. This technique augments that of Pratz et al, who encoded all spatial dimensions [9]; such a technique is more suitable for such applications as small-animal imaging. The advantage of this new approach is that enables XLT in surgical applications such as breast or brain excision, and may reduce dose. The performance of this technique is examined in both numerical and experimental phantoms for various object sizes and positions, within a geometry that mimics breast and brain intraoperative geometries.

2. Methods

2.1 Experimental Setup

The equipment used for this study consisted of an X-ray radiation source to excite the phosphors, and an optical detector to sample the photon fluence. During acquisition, the radiation source is collimated into a thin slice as described by Pratz et al.[9] to excite a plane shaped volume. An optical camera samples the emitted light. This schematic is shown in Figure 1a. The experimental setup is shown in Figure 1b.

The X-ray source used for the measurements in this paper was a 50kVp X-ray superficial unit (Pantak Therapax-150, Elimpex, AT) with a 10cm exit-diameter cone applicator. This cone was placed 17.5cm from surface of the phantom. The beam was collimated to 1mm wide (verified optically) by carefully positioned 50mm thick lead bricks. A high sensitivity EM-CCD camera (Pro-EM, Princeton Instruments, NJ) with a F/1.4 lens was positioned ~20 cm from the surface of the phantom. This distance was chosen to minimize X-ray photon noise[8]. As an alternative, optically clear leaded acrylic or leaded glass could be placed between the camera and the sample and used to reduce X-ray noise on the CCD and allow the camera to be placed closer to the sample to collect more light.

2.2 Image Formation

2.2.1 X-ray Luminescence Emission Forward Model

To determine the concentration of nanophosphors, the radiation (X-ray and optical) must be modeled. The emission of X-ray excitable nanophosphors is linearly dependent on the dose imparted to the tissue [8], d (units of Gy), the fractional efficiency of the phosphor

in converting ionizing energy to optical emission, Γ , and the concentration, c (units of mg/ml). The luminescent photon density from the nanophosphors, Φ , due to an incident radiation beam is therefore:

$$\Phi = \Gamma dc \quad (1)$$

Determining the total ionization energy imparted to the tissue (dose) is a procedure that requires calibration to incorporate the properties of the radiation emitted by the X-ray system. This calibration is system-specific, taking into account tube potential, geometry, X-ray tube target, and filter material; these factors taken together form an X-ray spectrum, known as the beam quality. The dose at depth is determined using measurements from a calibrated ionization chamber in a phantom and composed into a look-up-table, the Percent Depth Dose (PDD) curves. This system-wide calibration is performed periodically[20]. Using the PDD curves, dose at a specific depth in the tissue can be determined by knowing the source-to-surface distance between the X-ray tube and the tissue. This method can have high quantitative accuracy of 1-2% [21]. Another method to accurately determine dose is through Monte-Carlo methods, which model the system, including the above factors and also including patient anatomy. This method can calculate dose with high accuracy as long as comprehensive modeling of beam quality is performed[22]. In this study, we used the PDD curves to determine dose.

2.2.2 Diffuse Optical Forward Model

Images acquired at the tissue surface are input into a photon propagation model to determine the phosphor distribution. The images from the CCD camera are first processed to remove X-ray noise using a simple gradient-threshold algorithm, and then input into the algorithm as the data. The propagation of optical light can be approximated by the lossy photon Diffusion Equation (DE) [23], which yields the photon density in tissue. The DE is valid for many soft human tissues, including the breast, lung, prostate, brain, etc. [24]. Following excitation from X-ray radiation, the time-independent luminescence photon density emitted from the nanophosphors is:

$$\Phi(r) = -\nabla \cdot D(r) \nabla \phi(r) + \mu_a(r) \phi(r) \quad (2)$$

where $\phi(r)$ is the photon fluence at position r , in units of photons per area per time, and $\Phi(r)$ is the photon density, in units of photons per volume per time. Photon propagation

is affected by the absorption and diffusion coefficients of the tissue, μ_a and D , respectively, which are dependent on wavelength. The diffusion coefficient, D , is defined as $D = \frac{1}{3(\mu_a + \mu_s')}$, where μ_s' is the reduced scattering coefficient of the emitted photons. A type III boundary condition is used to model the photon fluence at the boundary, $-D\nabla\phi \cdot \hat{n} = \alpha\phi$, where α defines the internal reflection of the light at the tissue boundary due to the index of refraction mismatch between tissue and air[25][26], and the unit vector n is normal to the surface of the phantom. Because no unique solution exists for (2) with arbitrary boundaries, equation (2) is approximated with the Finite Element Method(FEM)[23]. This problem is similar to the diffuse optical fluorescence model introduced by Jiang[27], and is adapted here.

As described by Jiang, the photon emission may be approximated with the FEM by:

$$[A]\{\phi\} = \{b\} \quad (3)$$

where A is the FEM approximation of the physics of photon propagation (the right-hand-side of equation (2)) and b is the approximation to the light source (the left-hand-side of equation (2)). More specifically, the physics of the photon propagation is approximated with the FEM by:

$$A_{i,j} = \left\langle -D\nabla\psi_j \cdot \nabla\psi_i - \mu_a\psi_j\psi_i \right\rangle \quad (4)$$

where $\psi_{i,j}$ are the volume elements that discretize the imaging domain and form a geometrical mesh defined over the entire imaging domain. A is integrated over this imaging domain. The source (in this case, the light emitted from the phosphors which were excited by the X-ray source) and boundary integral are approximated with the FEM by:

$$b_i = -\left\langle \sum_{j=1}^N \Phi_j \psi_j \psi_i \right\rangle + \alpha \sum_{j=1}^M \phi_j \oint_{boundary} \psi_j \psi_i ds \quad (5)$$

The time component of the luminescence lifetime is ignored since the measurements in this work are from an integrating CCD camera, and the measurement time is much greater than the luminescence lifetime; effects from the minimal afterglow of the phosphors are ignored.

The FEM model, G , is used to generate estimates for the photon fluence given the optical properties of the tissue, the concentration of phosphors, c , and the FEM mesh. An estimate for the photon fluence, ϕ , can be calculated by solving equation (3):

$$\phi = G = [A]^{-1}\{b\} \quad (6)$$

In this paper, the imaging domain is known, and is assumed that the endogenous optical tissue properties are known, so the model is dependent only on the unknown, c . Figure 2 shows the optical photon fluence for a numerical phantom with 100:1 phosphor concentration between an object and the background. Two different source configurations are shown, each with the X-ray direction of propagation in the horizontal (left/right) direction. In Figure 2a-b, the X-ray source, indicated by the red circle, irradiates a horizontal line passing through the background, whereas in Figure 2c-d, the X-ray irradiates the horizontal line passing through the middle of the phosphor-containing object.

2.2.3 X-ray Nanophosphor Concentration Reconstruction

The goal of X-ray Luminescence Tomography is to determine the phosphor distribution. This spatial distribution can be determined by minimizing the difference between the measured photon flux from the camera, $\phi_M(r)$, and the simulated photon flux, $\phi_S(r)$ at identical sample locations. This is accomplished by minimizing the L2-norm of the objective function in an optimization routine:

$$\Omega = (\phi_S - \phi_M)^2 \quad (7)$$

where Ω is the objective function to minimize. Because of the large dynamic range, the first term in (7) is formulated from the natural logs of the photon fluxes. This is an underdetermined problem, as measurements are made only at the boundary. Because this problem is underdetermined, the model, G , is linearized with a Taylor approximation and formed into an iterative algorithm as:

$$G(c_i) = G(c_{i-1}) + G' \Delta c \quad (8)$$

where G' is the partial differential of the model with respect to the concentration, also known as the Jacobian, J . Minimizing equation (7) with respect to c and substituting $G(c_i)$ from equation (8) into ϕ_S and J for G' yields:

$$2J\left((G(c_{i-1}) + J\Delta c) - \phi_M\right) = 0 \quad (9)$$

Solving for the concentration yields:

$$\Delta c = -[J^T J]^{-1} J^T (\phi_S - \phi_M)$$

This problem is ill-posed, so it is solved using the Levenberg-Marquardt [28] algorithm, which includes a stabilization parameter, λ , in the inversion to avoid singularities:

$$\Delta c = -[J^T J + \lambda I]^{-1} J^T (\phi_S - \phi_M) \quad (10)$$

Equation (5) is iterated until a minima is reached (the L2 norm of the update is less than 1% of the previous iteration), or until 15 iterations are performed, whichever occurs earlier. The stabilization parameter is reduced at each iteration as the algorithm approaches the minimum and converges on the solution.

Although this study focused on applications where a single angle is ideal, note that this algorithm is not limited to a single angle. Thus, this algorithm is appropriate for any sparse-angle geometry.

2.3 Phantom Study

The performance of the experimental setup and the reconstruction algorithm were tested by varying the size and location of a lesion-simulating object. The relationships between source-object and detector-object distance on resolving an object of various sizes were determined with both numerical and experimental phantoms. The metrics used to determine system performance were object location and object size. Location error in both the X-ray excitation and optical read-out dimensions was determined by calculating the distance between the true centroid of the lesion and the location of the maximum recovered value of the phantom. Object size in both the X-ray excitation and optical read-out dimensions were determined by calculating the full width at half maximum (FWHM) of the object in these dimensions. Concentration sensitivity and contrast recovery were also examined.

2.3.1 Numerical Phantoms

Numerical phantoms were utilized to test the position-accuracy, object size-accuracy, and sensitivity of the algorithms. The position and object-size phantoms investigated the

recovery of simulated tumors with 10:1 contrast between the object and the background and phosphor concentrations of 10 μ g/ml. These lesions varied in size between 2-14mm, and were placed at different locations in the phantom, as depicted in Figures 3a and 4a (note the multiple arrows, which indicate the minimum and maximum extent of the object locations investigated). Sufficient dose (1cGy) was given to yield signal-to-noise (SNR) greater than 10 for each object position - this methodology allowed a performance test of the algorithm for all object positions.

The sensitivity phantom included an object with varying concentration (Figure 5a), and varying contrast (Figure 5b). The 6mm-diameter object was placed at the center of the phantom along the dimension of the detectors (the long-axis), and moved at various depths away from the detectors. We used the phosphor properties from Kandarakis et al. [29] to obtain quantification of the emitted light efficiency for their lanthanum oxysulfide:terbium phosphor, which was 1.39×10^{15} optical photons / (Gy x mg). We incorporated solid-angle losses as well as losses due to lens inefficiency (DO-1795, Navitar Imaging Solutions, Rochester, NY). SNR below 10 was assumed to be too low to detect.

All phantoms were 2-dimensional, and measured 12cm x 6cm. Detectors were placed along the long-axis of the phantom, while the collimated X-ray source, 1mm wide, was scanned along the short axis. The phosphor used for this experiment mimicked GOS:Eu, demonstrated in X-ray luminescence imaging in a previous study, which has a strong luminescence emission at ~618nm. Background optical properties were similar to that of breast tissue [30] ($\mu_a = 0.0027$, $\mu_s' = 0.717$).

2.3.2 Experimental Phantom

The experimental phantom is shown in Figure 6. Figure 6a-b show the relative layout of the objects in the phantom, while Figure 6c shows the camera-eye view of the phantom. Figure 6d shows an image of the phantom while the phantom is irradiated by the X-ray beam. The optically clear acrylic phantom, measuring 12cm x 6cm, was filled with india ink to mimic optical absorption, and intralipid to mimic optical scatter, at the appropriate concentrations. The optical properties were: ($\mu_a = 0.0027$, $\mu_s' = 0.717$, as determined from a diffuse optical spectroscopy system). GOS:Eu phosphor at a concentration of

10mg/ml was added to two cylindrical inclusions, one 5mm in diameter, and one 10mm in diameter, which were located 3cm and 9cm from the edge nearest the X-ray source, respectively. The inclusions were both imaged at various depths from the edge nearest the detector: 10mm, 15mm, 20mm, 30mm; these dimensions are shown more clearly in Figure 7a. The exposure times and gains were 1.5s at gain 500, 3.5s at gain 800, 3s at gain 1000, and 7.5s at gain 1000, for increasing depth. Dose to the phantom varied depending on the phosphor depth, so that a high SNR could be acquired while the phosphors were irradiated. The doses to the phantom were 6.7 cGy, 15.6 cGy, 13.4 cGy, and 33.4 cGy, for increasing depth.

3. Results

3.1 Numerical phantom results

As described above, a lesion-simulating object was placed in various locations in the volume so that the performance of LAXLT could be analyzed. The lesion location was varied with respect to the source-axis and detection-axis separately to determine the effects of source-object distance and detector-object distance on the ability to resolve the object. Figure 3 shows the results of maintaining a fixed detector-object distance while varying the source-object distance (varying depth with respect to the X-ray). These dimensions are depicted in Figure 3a. The location error for the 2-14mm objects is shown in Figure 3b. This result demonstrates the excellent ability of the algorithm to spatially resolve an object, as all errors in distance are lower than 3.5mm. Figure 3c shows the recovered object size in the direction of the X-ray excitation, which demonstrates the insensitivity with respect to depth, with an average standard deviation in the error in recovered size of 0.82mm for varying source-object distances. In Figure 3d, the recovered size of the object in the optical dimension is examined as a function of source-object depth. The algorithm is able to distinguish the varying sizes of the objects, with a standard deviation in the error in recovered size of 0.83mm for the varying source-object distance. There is a slight tendency for blurring in the optical dimension due to the scattering of the optical photons.

Figure 4 shows the effects of varying the depth of an object with respect to the optical dimension. Figure 4a shows the physical dimensions of the phantom. The object

was moved from 0.5cm to 4.5cm from the detector, while remaining at a fixed distance from the X-ray source. Figure 4b shows the recovered location error of the centroid of the object with respect to depth from the optical detector. In this experiment, the ability to resolve an object of ~2mm was at the limit of the system with the 1mm collimated X-ray beam that was used. However, the objects sized 4mm and larger were resolved with higher accuracy. As expected, location error increases slightly as the depth increases, and larger objects are resolved more accurately than smaller objects. The advantage of using the X-ray is highlighted here, as even at 4.5cm in depth, the object is resolved with less than 1cm total error. Figure 4c shows the recovery of object size in the X-ray dimension, similar to Figure 3c. The mean standard deviation for the error in recovered object size was 1.36mm. Figure 4d shows that the ability to determine the size of the object in the optical dimension has increased variability compared to the X-ray dimension, as the mean standard deviation of the error in recovered size with respect to depth is 2.4mm. This larger standard deviation is consistent with object-blurring at depth from the optical detector; this is expected due to the ill-posed nature of the algorithms needed for the optical photon modeling. Similar to Figure 3d, this system is able to distinguish between the different sized objects in the optical dimension, although again, there is a tendency for dilation in the optically-resolved dimension.

Overall, the numerical phantom results show localization accuracy with median error of 2.2mm (mean of 6.3mm), or 4.1% (mean of 11.5%) of object depth for all lesions. The recovered lesion size has lower size-bias, with median error of -8.1% vs. 87.5% (mean of 19.4% and 118.3%, respectively), in the X-ray excitation direction vs. the optical direction, respectively. Again, this optical dilation is expected due to the increased optical scatter compared to X-ray. This technique is invariant in recovered size with respect to depth, as the standard deviation is less than 2.5mm.

The concentration phantom is shown in Figure 5a. The required dose (in Gy) to reach an SNR of 10 is plotted for varying concentrations. It is apparent from this calculation that a 6mm-diameter object with $\mu\text{g/ml}$ concentration is detectable in this geometry with standard CT doses. With the doses currently used in IORT, concentrations to ng/ml are detectable at depth. As shown in Figure 5b, with sufficient signal, contrast can be recovered for all contrast to background ratios tested, for depths up

to 45mm. Here, the advantage of the ability of the collimated X-ray to selectively excite the phosphors is clear.

3.2 Experimental phantom results

Photographs of the experimental phantom are shown in Figure 6; the schematic of the experimental phantom is shown in Figure 7a, and the results are shown in Figure 7b-d. Reconstructions for each case are shown in Figure 8, with increasing depth with each row. In this experiment, a 1- 5mm object, and a 1- 10mm object were imaged at various depths. For all depths, the recovered location error for both objects is less than 6mm, and is independent of object size. Positional errors are recovered within 8.6% of the effective depth for a 5mm object, and within 5.2% of the depth for a 10mm object. Similar to the results from the numerical phantom, the ability to discern object size is highly accurate in the X-ray dimension, and is invariant with depth. The ability to resolve the object in the optical dimension is accurate to within 2mm. Object size median error is within 2.3% and 2% for the 5mm and 10mm objects, respectively.

4. Discussion

Molecular imaging has long been identified as potentially a vital tool in surgery to aid in the identification of important tissue structures and tumor tissue[31]. Until recently, the use of molecular imaging in surgery has been limited, both due to the lack of appropriate imaging tools, as well as the lack of highly-specific contrast agents (the problem with most endogenous fluorescence agents in the body). Recent developments in both of these areas have increased the interest of molecular surgical-guidance [3]. For instance, Fluorescence Molecular Tomography (FMT) shows great promise in positively affecting surgical outcomes, as it is non-ionizing, has a wealth of knowledge of contrast agents, and can be implemented at low cost. FMT has found utility in tumor-margin excision [32], sentinel lymph-node mapping [4], and avoidance of critical structures such as nerves[33]. Alternatively, sentinel lymph node identification with radio-emission imaging is widely adopted[5]; its use in surgical resection is not well established.

The lack of wide-adoption of molecular imaging in surgical applications can partly be blamed on the limited flexibility of these imaging technologies. While FMT is

ideal for structures at the surface and several millimeters beyond, its limitations in depth penetration preclude its ability to unmask disease that exists several centimeters beneath the surface. Radio-emission imaging is limited because of the need to image gamma photons which are highly penetrating in tissue – this prevents the identification of lesion depth, and increases the burden on the surgeon to patiently dig through the tissue until the object is identified. In the case of a sub-millimeter sized tumor tissue, this practice would be overly laborious.

Clearly, a void exists in the ability of molecular instrumentation to resolve millimeter or sub-millimeter objects at depths of several centimeters. LAXLT may be able to fill this void. Its advantage is the ability to resolve objects at several centimeters of deep. Figure 9 demonstrates this ability, as it is shown that both the 5mm and 10mm objects in the experimental phantom were able to be resolved at a detector-object depth of beyond 3cm. This is a stark contrast to FMT, as Kepshire et al. [18] demonstrated that depth linearity degrades beyond 1cm. If the depth penetration of the X-ray source is considered, LAXLT is linear beyond 10cm. This increased performance is due to the low scatter and high penetrability of the X-ray excitation, which allows more ideal imaging geometries to be chosen for surgical guidance.

The benefit of the technique developed in this study compared to previous developments with XLT is three-fold: increased temporal resolution is possible because of the optical read-out of two-dimensions, which eliminates X-ray encoding in those dimensions; lower dose is possible because of the decreased X-ray excitation; most importantly, this technique is suitable for geometries where full angular X-ray encoding is not possible. Therefore, this technique enables XLT to be used for surgeries such as breast lumpectomy; we foresee applications such as this to be one of the most important future applications in imaging. In breast lumpectomy, a full-angular encoding with X-ray is not desirable because deep critical structures are irradiated. By instead implementing a limited-angle technique, only the breast may be irradiated. For lumpectomy, this technique would be desirable to verify the position of the lesions in the surgical supine position, and to visualize remaining disease after resection.

In comparing this technique to other image-guided surgical modalities such as FMT, the advantages of LAXLT are clear. LAXLT was able to resolve 4mm objects at

detector-object depths greater than 4.5cm, compared to FMT which is limited in to about 1cm in resolving object dimensions[18]. The most impressive aspect indicated by these results is the reduction in the blurring of the object with respect to depth; this highlights the advantage of incorporating the X-ray excitation, which due to its relatively insignificant scatter at these depths, can pinpoint the depth of the object with respect to the optical depth dimension. The optical read-out is then used to determine the other dimensions. Since the depth is known to high accuracy (shown in Figure 4), the diffuse algorithm properly models the diffuse nature of the light, and significantly reduces object blurring, as presented in Figure 5. Thus, with LAXLT, dose and imaging time are reduced significantly compared to XLT.

It is intuitive that the resolution will be limited by the width of the X-ray beam, at shallower depths. At deeper depths, the scatter of the X-ray beam should be taken into account. In this study, a 1mm collimated X-ray beam was able to successfully visualize a 2mm object up to 2cm, and a 4mm object up to 4.5cm. Higher resolution should be attained with a narrower beam; we are currently investigating this effect. The ability to resolve an object at depth is instead limited by dose.

Although this study was adapted to geometries best suitable to tumor resection, it should be noted that the algorithm presented in this work is generalizable to any geometry; it is especially useful for sparse-angle geometries. An additional use for this technique would be for intraoperative probes, where simple coregistration (assuming the catheter is radio-opaque) between the X-ray source and the optical detection catheter could provide assessment of molecular status at a remote location.

An increase in dose to potentially healthy tissue is one disadvantage of this technique. Although we calculated that the maximum dose to the phantom was 33.4 cGy, this dose will be reduced to 6cGy with a more favorable optical setup where the camera is closer to the object. This dose may be reduced further with a contact optical setup. Still, this dose may preclude its use in a screening setting, especially due to the increasing awareness of increasing radiation exposure in medicine[34]. However, post-surgical radiation therapy is commonly prescribed as a means to destroy cancer cells that may not have been removed around the margin [35, 36]. In Accelerated Partial Breast Irradiation, 5-20 Gy of radiation is given to the resected cavity in 1-5 fractions, to reduce the

morbidity of whole breast radiation therapy [37]. In this context, LAXLT may have great utility to identify larger regions that may have been missed during surgery, and may require subsequent surgical investigation. Its sensitivity at this dose might enable the identification of micro-disease, or a very low concentration to be injected.

The other disadvantage of this technique is its use of nanoparticles. Although we have demonstrated low-toxicity of our nanoparticles in cells, nanoparticles will have different effects in a living system. This topic is beyond the scope of this paper, but it is important to recognize that cancer nanotechnology is a major venture in the National Cancer Institute, and this technique will benefit from the knowledge gained from this program.

5. Conclusions

Limited Angle X-ray Luminescence Tomography has been developed as a means to image molecular deeper than is available with Fluorescence Molecular Tomography. A reconstruction algorithm, based on a hybrid X-ray excitation/diffuse optical emission model, was tested in a numerical and experimental phantom that had dimensions similar to the human breast. It was found that objects as small as 2mm in diameter could be resolved at depths of up to 4-5cm. It was shown that the depth of the object with respect to the X-ray source position had little effect on object recovery in this volume. It was then demonstrated experimentally that both a 5mm and 10mm object could be resolved at depths of at least 3cm – these results agreed with the numerical phantom results, thus validating the simulation. If the challenges to engineering biocompatible phosphors can be resolved, LAXLT may have utility in surgical applications where small lesions must be imaged at depth of a few centimeters, such as during breast lumpectomy surgery.

6. Acknowledgements

The authors gratefully acknowledge the Department of Defense Breast Cancer Postdoctoral Fellowship BC097779, the National Institutes of Health ICMIC P50CA114747, the Center for Biomedical Imaging at Stanford, and the Friends for Early Breast Cancer Detection for funding.

References

- ¹G. R. Gibson, B. A. Lesnikoski, J. Yoo, L. A. Mott, B. Cady, and R. J. Barth, Jr, "A comparison of ink-directed and traditional whole-cavity re-excision for breast lumpectomy specimens with positive margins," *Ann Surg Oncol* **8** (9), pp. 693-704 (2001).
- ²A. Fortin, M. Larochelle, J. Laverdière, S. Lavertu, and D. Tremblay, "Local failure is responsible for the decrease in survival for patients with breast cancer treated with conservative surgery and postoperative radiotherapy," *J Clin Oncol* **17** (1), pp. 101-9 (1999).
- ³R. Weissleder and M. J. Pittet, "Imaging in the era of molecular oncology," *Nature* **452** (7187), pp. 580-9 (2008).
- ⁴E. Tanaka, H. S. Choi, H. Fujii, M. G. Bawendi, and J. V. Frangioni, "Image-guided oncologic surgery using invisible light: completed pre-clinical development for sentinel lymph node mapping," *Ann Surg Oncol* **13** (12), pp. 1671-81 (2006).
- ⁵J. C. Alex and D. N. Krag, "Gamma-probe guided localization of lymph nodes," *Surg Oncol* **2** (3), pp. 137-43 (1993).
- ⁶W. Stummer, H.-J. Reulen, T. Meinel, U. Pichlmeier, W. Schumacher, J.-C. Tonn, V. Rohde, F. Oppel, B. Turowski, C. Woiciechowsky, K. Franz, T. Pietsch, and {ALA-Glioma Study Group}, "Extent of resection and survival in glioblastoma multiforme: identification of and adjustment for bias," *Neurosurgery* **62** (3), pp. 564-76; discussion 564-76 (2008).
- ⁷G. Torzilli, T. Takayama, A. M. Hui, K. Kubota, Y. Harihara, and M. Makuuchi, "A new technical aspect of ultrasound-guided liver surgery," *Am J Surg* **178** (4), pp. 341-3 (1999).
- ⁸C. Carpenter, C. Sun, G. Pratz, R. Rao, and L. Xing, "Hybrid X-ray/Optical Luminescence Imaging; Characterization of Experimental Conditions," *Medical Physics* **37** (8), pp. (2010).
- ⁹G. Pratz, C. Carpenter, C. Sun, and L. Xing, "X-Ray Luminescence Computed Tomography via Selective Excitation: A Feasibility Study," *IEEE Trans Med Imaging* **in**

press, pp. (2010).

¹⁰G. Pratz, C. Carpenter, C. Sun, P. Ravilsetty, and L. Xing, "Tomographic Molecular Imaging using X-Ray-Excitable Nanoparticles," *Optics Letters* **in press**, pp. (2010).

¹¹W. Chen, "Nanoparticle fluorescence based technology for biological applications," *J Nanosci Nanotechnol* **8** (3), pp. 1019-51 (2008).

¹²C. Sun, C. Carpenter, G. Pratz, and L. Xing, "Facile Synthesis of Amine-Functionalized Eu³⁺-Doped La(OH)₃ Nanophosphors for Bioimaging," *Nanoscale Research Letters* , pp. (2010).

¹³K. Sokolov, M. Follen, J. Aaron, I. Pavlova, A. Malpica, R. Lotan, and R. Richards-Kortum, "Real-time vital optical imaging of precancer using anti-epidermal growth factor receptor antibodies conjugated to gold nanoparticles," *Cancer Res* **63** (9), pp. 1999-2004 (2003).

¹⁴R. Haubner, H. J. Wester, W. A. Weber, C. Mang, S. I. Ziegler, S. L. Goodman, R. Senekowitsch-Schmidtke, H. Kessler, and M. Schwaiger, "Noninvasive imaging of alpha(v)beta3 integrin expression using 18F-labeled RGD-containing glycopeptide and positron emission tomography," *Cancer Res* **61** (5), pp. 1781-5 (2001).

¹⁵X. Chen, P. S. Conti, and R. A. Moats, "In vivo near-infrared fluorescence imaging of integrin alphavbeta3 in brain tumor xenografts," *Cancer Res* **64** (21), pp. 8009-14 (2004).

¹⁶H. H. Barrett, "Limited-angle tomography for the nineties.[comment]," *Journal of Nuclear Medicine* **31** (10), pp. 1688-92 (1990).

¹⁷D. W. Roberts, P. A. Valdés, B. T. Harris, K. M. Fontaine, A. Hartov, X. Fan, S. Ji, S. S. Lollis, B. W. Pogue, F. Leblond, T. D. Tosteson, B. C. Wilson, and K. D. Paulsen, "Coregistered fluorescence-enhanced tumor resection of malignant glioma: relationships between delta-aminolevulinic acid-induced protoporphyrin IX fluorescence, magnetic resonance imaging enhancement, and neuropathological parameters," *J Neurosurg* , pp. (2010).

¹⁸D. S. Kepshire, S. C. Davis, H. Dehghani, K. D. Paulsen, and B. W. Pogue, "Subsurface diffuse optical tomography can localize absorber and fluorescent objects but recovered image sensitivity is nonlinear with depth," *Appl Opt* **46** (10), pp. 1669-78 (2007).

¹⁹M. A. O'Leary, D. A. Boas, B. Chance, and A. G. Yodh, "Experimental images of heterogeneous turbid media by frequency-domain diffusing-photon tomography," *Opt.*

Lett. **20** (5), pp. 426-428 (1995).

²⁰C. M. Ma, C. W. Coffey, L. A. DeWerd, C. Liu, R. Nath, S. M. Seltzer, J. P. Seuntjens, and {American Association of Physicists in Medicine}, "AAPM protocol for 40-300 kV x-ray beam dosimetry in radiotherapy and radiobiology," *Med Phys* **28** (6), pp. 868-93 (2001).

²¹P. Munck af Rosenschöld, P. Nilsson, and T. Knöös, "Kilovoltage x-ray dosimetry--an experimental comparison between different dosimetry protocols," *Phys Med Biol* **53** (16), pp. 4431-42 (2008).

²²F. Verhaegen, A. E. Nahum, S. Van de Putte, and Y. Namito, "Monte Carlo modelling of radiotherapy kV x-ray units," *Phys Med Biol* **44** (7), pp. 1767-89 (1999).

²³S. R. Arridge, M. Schweiger, M. Hiraoka, and D. T. Delpy, "A Finite-Element Approach for Modeling Photon Transport in Tissue," *Medical Physics* **20** (2), pp. 299-309 (1993).

²⁴W. F. Cheong, S. A. Prahl, and A. J. Welch, "A review of the optical properties of biological tissues," *IEEE J. of Quant. Electr.* **26** (12), pp. 2166-2185 (1990).

²⁵M. Schweiger, S. R. Arridge, M. Hiraoka, and D. T. Delpy, "The finite element method for the propagation of light in scattering media: Boundary and source conditions," *Medical Physics* **22** (11), pp. 1779-1792 (1995).

²⁶R. Aronson, "Boundary-conditions for diffusion of light," *J. Opt. Soc. Am. A* **12** (11), pp. 2532-2539 (1995).

²⁷H. B. Jiang, "Frequency-domain fluorescent diffusion tomography: a finite- element-based algorithm and simulations," *Applied Optics* **37** (22), pp. 5337-5343 (1998).

²⁸D. W. Marquardt, "An Algorithm for Least-Squares Estimation of Nonlinear Parameters," *Journal of the Society for Industrial and Applied Mathematics* **11** (2), pp. 431-441 (1963).

²⁹I. Kandarakis, D. Cavouras, G. Panayiotakis, T. Agelis, C. Nomicos, and G. Giakoumakis, "X-ray induced luminescence and spatial resolution of La₂O₂S:Tb phosphor screens," *Phys Med Biol* **41** (2), pp. 297-307 (1996).

³⁰V. G. Peters, D. R. Wyman, M. S. Patterson, and G. L. Frank, "Optical properties of normal and diseased human breast tissues in the visible and near infrared," *Phys. Med. Biol.* **35**, pp. 1317-1334 (1990).

³¹H. B. Gregorie, Jr, E. O. Horger, J. L. Ward, J. F. Green, T. Richards, H. C. Robertson, Jr, and T. B. Stevenson, "Hematoporphyrin-derivative fluorescence in malignant neoplasms," *Ann Surg* **167** (6), pp. 820-8 (1968).

³²W. Stummer, A. Novotny, H. Stepp, C. Goetz, K. Bise, and H. J. Reulen, "Fluorescence-guided resection of glioblastoma multiforme by using 5-aminolevulinic acid--induced porphyrins: a prospective study in 52 consecutive patients," *J. Neurosurg.* **93**, pp. 1003-1013 (2000).

³³L. B. Boyette, M. A. Reardon, A. J. Mirelman, T. D. Kirkley, J. J. Lysiak, J. B. Tuttle, and W. D. Steers, "Fiberoptic imaging of cavernous nerves in vivo," *J Urol* **178** (6), pp. 2694-700 (2007).

³⁴E. M. Caoili, R. H. Cohan, J. H. Ellis, J. Dillman, M. J. Schipper, and I. R. Francis, "Medical decision making regarding computed tomographic radiation dose and associated risk: the patient's perspective," *Arch Intern Med* **169** (11), pp. 1069-71 (2009).

³⁵F. M. Dirbas, "Accelerated partial breast irradiation: where do we stand?," *J Natl Compr Canc Netw* **7** (2), pp. 215-25 (2009).

³⁶A. Munshi, "External hypofractionated whole-breast radiotherapy: now where does accelerated partial breast irradiation stand?," *J Cancer Res Ther* **3** (4), pp. 231-5 (2007).

³⁷G. Ross, "Accelerated partial breast irradiation: technically feasible but who will benefit?," *Breast Cancer Res* **7** (3), pp. 110-2 (2005).

Figure Captions

Figure 1: (a) Schematic of LAXLT while imaging a phantom with a single spherical object (b) Experimental setup used in this study. A black-box was used to enclose the phantom (not shown) and eliminate ambient light from the experiment.

Figure 2: (a) Numerical phantom with a single object located at the center of the domain, and a 10:1 contrast in phosphor between the object and background. The X-ray source irradiates the domain along the long-axis of the phantom at a position of $X=10$, $Y=-60:60$. (b) The emission fluence field of (a). (c) Numerical phantom with the X-ray source irradiating at a position of $X=40$, $Y=-60:60$. (d) The emission fluence field of (c).

Figure 3: (a) Numerical phantom experiment examining the effect of moving a variable sized object away (4 positions, indicated by the arrows) from the X-ray source plane (S), while keeping the distance from the detection plane (D) fixed. (b) Recovered object location error. (c) Recovered object diameter FWHM with respect to the X-ray source dimension. (d) Recovered object diameter FWHM with respect to the optical detection dimension.

Figure 4: (a) Numerical phantom experiment examining the effect of moving a variable sized object away (8 positions, indicated by the arrows) from the optical detection plane (D), while keeping the distance from the X-ray source plane (S) fixed. (b) Recovered object location error. (c) Recovered object diameter FWHM with respect to the X-ray source dimension. (d) Recovered object diameter FWHM with respect to the optical detection dimension.

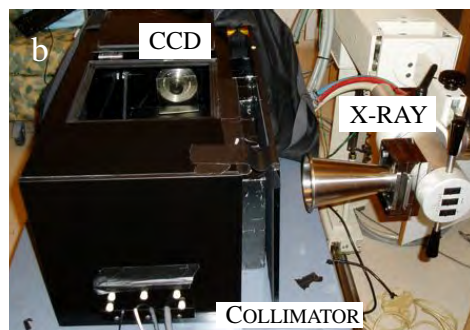
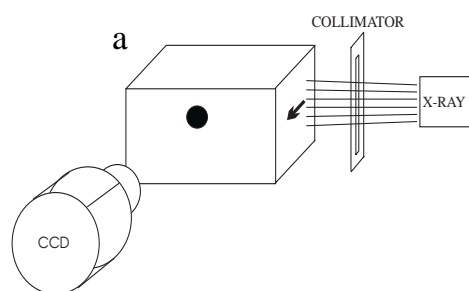
Figure 5: (a) Numerical phantom experiment examining the effect of: (a) variable object to background contrast and (b) variable concentration, of a 6mm-diameter object vs. depth from the detection plane.

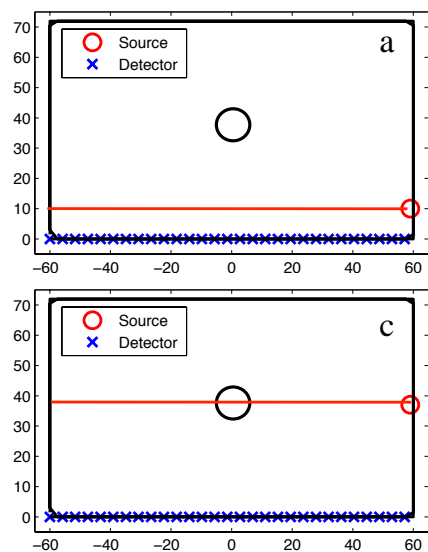
Figure 6: Experimental phantom: (a-b) Two views from above the black-box including the phantom and collimator bricks. (c) Image taken by the high-sensitivity CCD camera of the phantom under ambient light and no irradiation, (d) CCD image with no ambient light and X-ray irradiation.

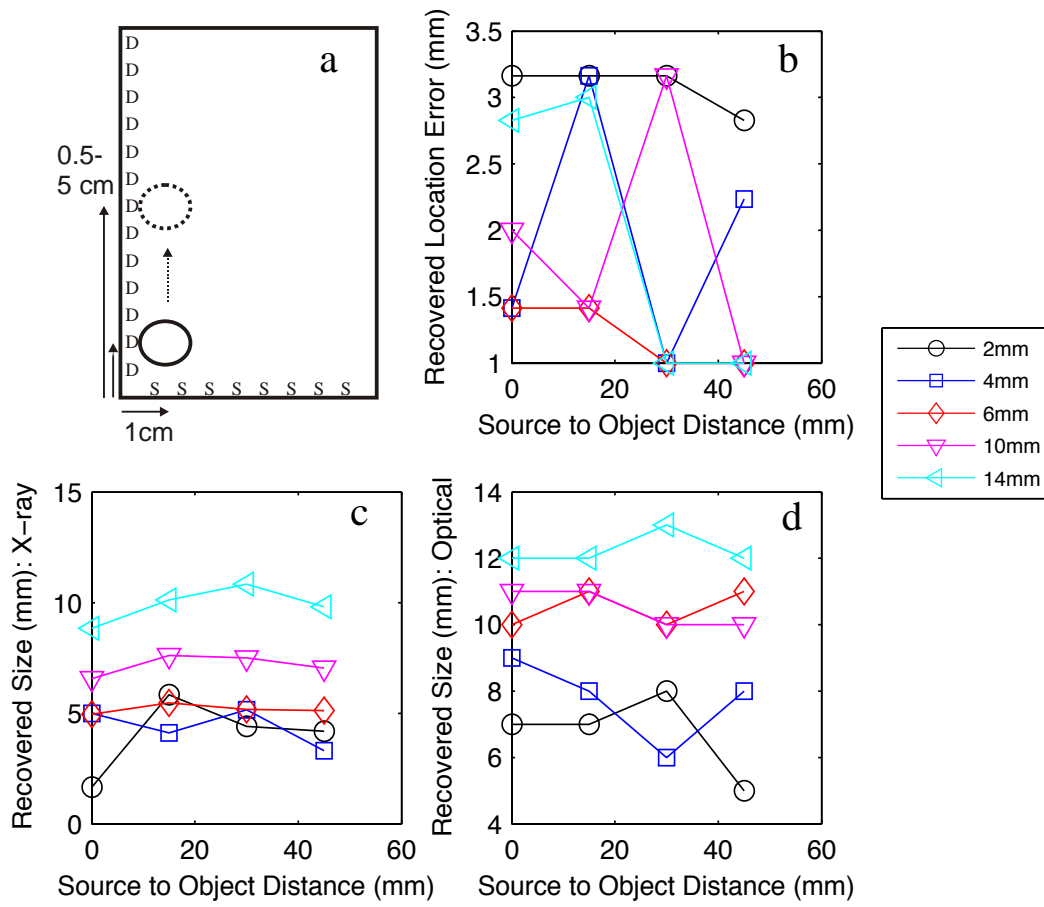
Figure 7: (a) Experimental phantom of two objects moved away from the optical detection plane (D) at 4 positions. (b) Recovered object location error. (c) Recovered object diameter FWHM with respect to the X-ray source dimension. (d) Recovered object diameter FWHM with respect to the optical detection dimension.

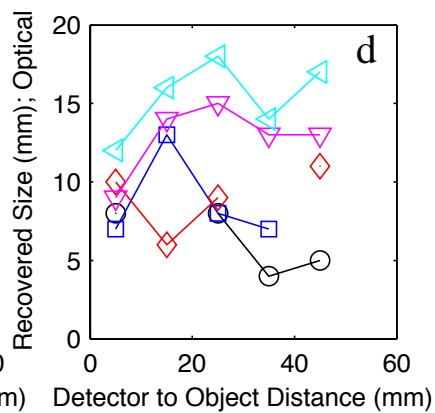
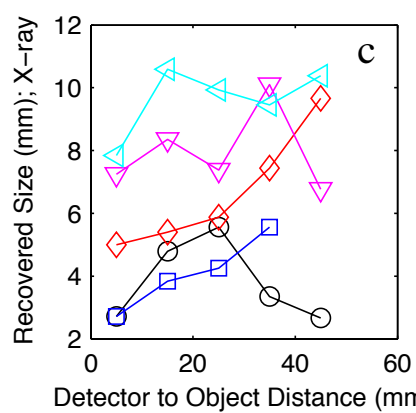
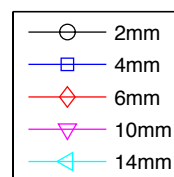
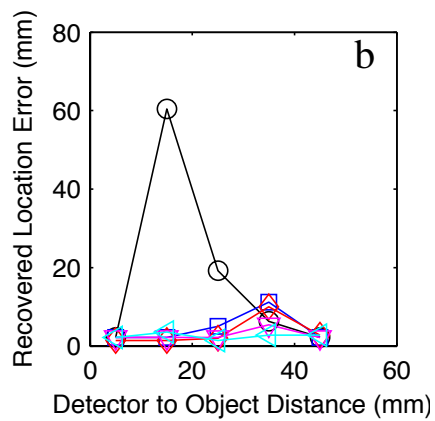
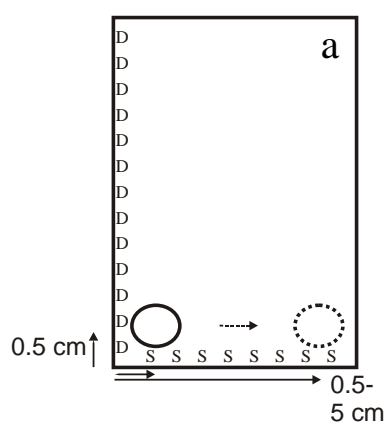
Figure 8: Image reconstructions of 2 objects with depths of (a) 10mm, (b) 15mm, (c) 20mm, and (d) 30mm from the detection plane.

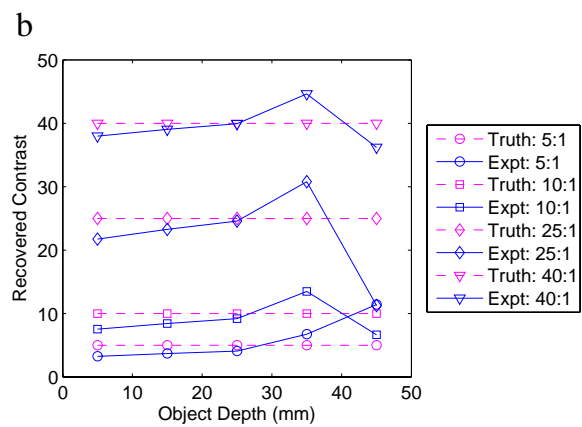
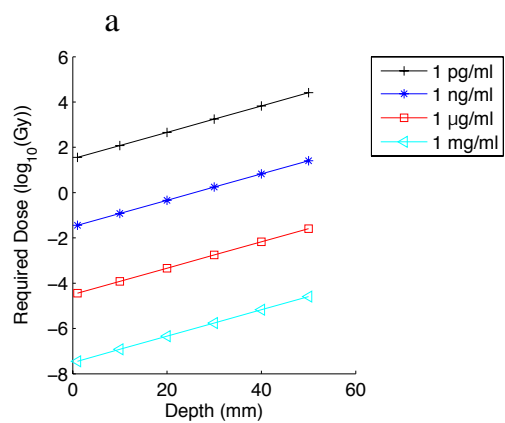
Figure 9: (a) Object location linearity of the depth of the object with respect to the detection plane. (b) Object location linearity of both the depth of the object with respect to the detection plane summed with distance with respect to the source plane.

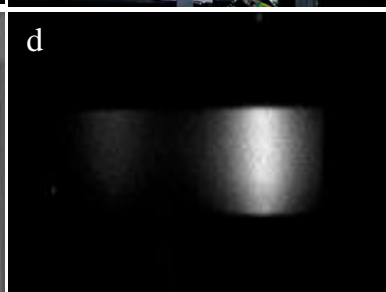
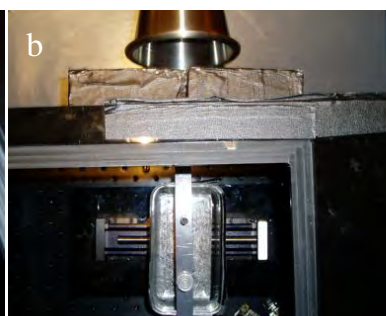
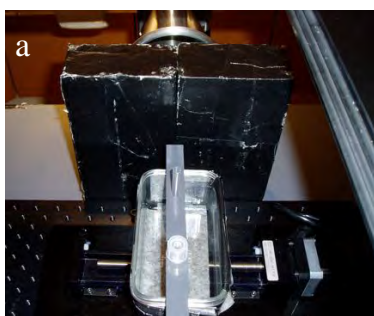


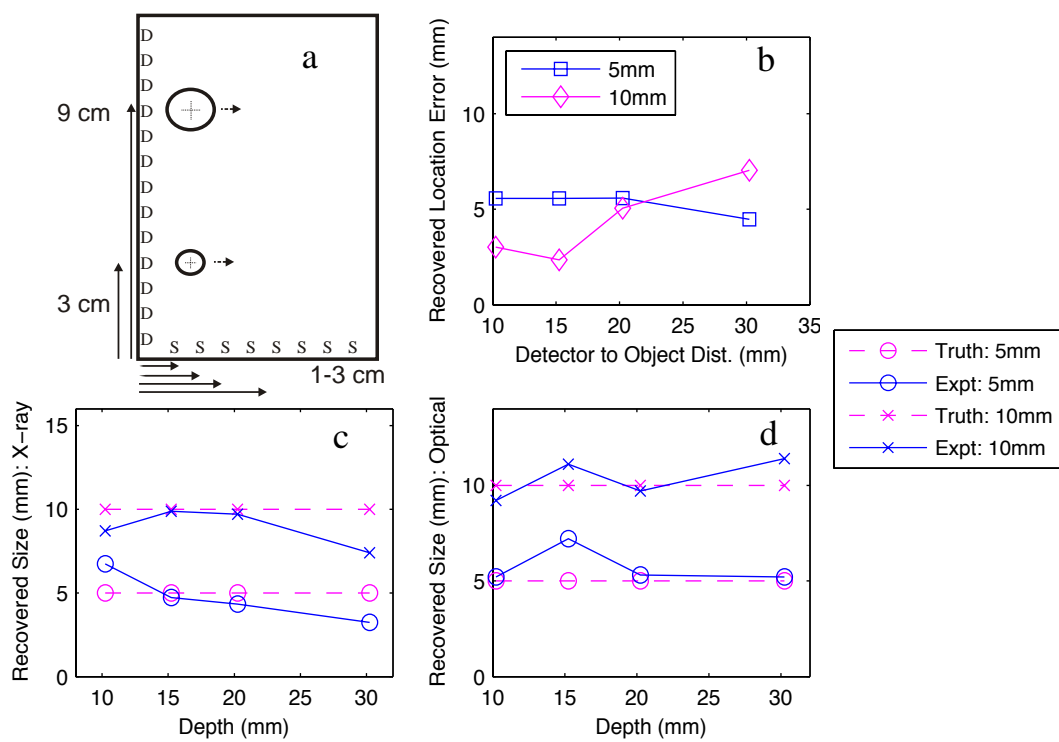




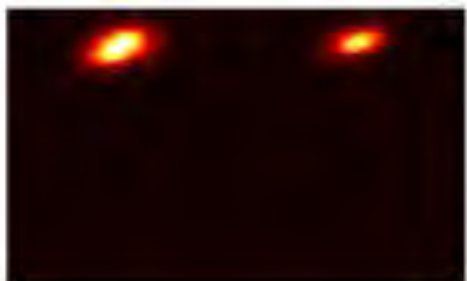








a



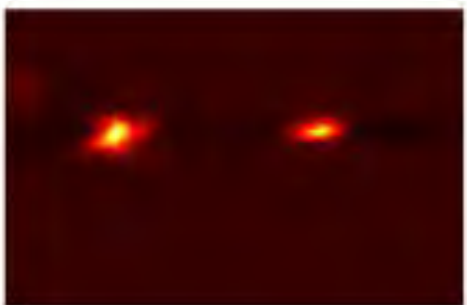
b

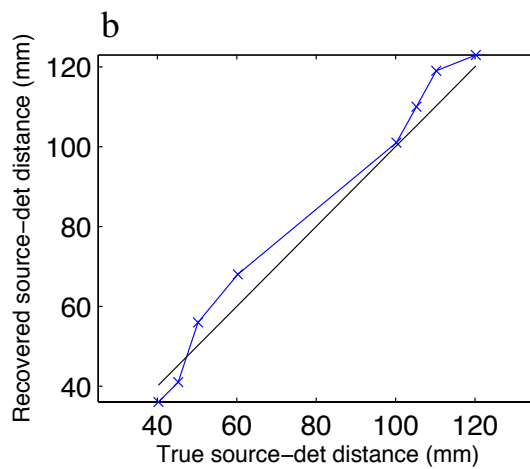
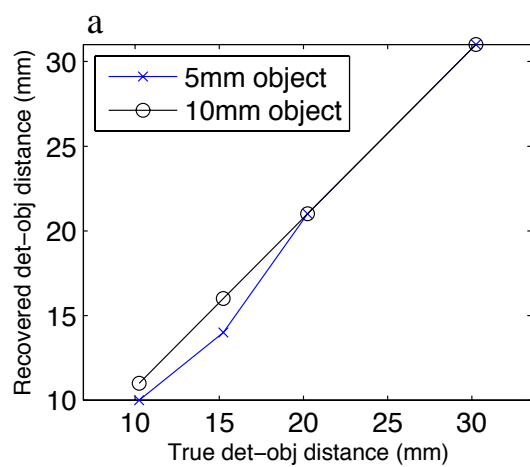


c



d





Radioluminescent nanophosphors enable multiplexed small-animal imaging

Colin M Carpenter,¹ Conroy Sun,¹ Guillem Pratx,¹ Hongguang Liu,² Zhen Cheng,² and Lei Xing^{1*}

¹Department of Radiation Oncology, School of Medicine, Stanford University, Stanford, CA USA 94305

²Molecular Imaging Program at Stanford (MIPS), Department of Radiology and Bio-X Program, Canary Center at Stanford for Cancer Early Detection, Stanford University, California, 94305-5344

*lei@stanford.edu

Abstract: We demonstrate the ability to image multiple nanoparticle-based contrast agents simultaneously using a nanophosphor platform excited by either radiopharmaceutical or X-ray irradiation. These radioluminescent nanoparticles emit optical light at unique wavelengths depending on their lanthanide dopant, enabling multiplexed imaging. This study demonstrates the separation of two distinct nanophosphor contrast agents in gelatin phantoms with a recovered phosphor separation correlation of -0.98. The ability to distinguish the two nanophosphors and a Cerenkov component is then demonstrated in a small animal phantom. Combined with the high-resolution potential of low-scattering X-ray excitation, this imaging technique may be a promising method to probe molecular processes in living organisms.

©2012 Optical Society of America

OCIS codes: (110.4234) Multispectral and hyperspectral imaging; (170.0170) Medical optics and biotechnology; (160.4236) Nanomaterials.

References and links

1. M. Stroh, J. P. Zimmer, D. G. Duda, T. S. Levchenko, K. S. Cohen, E. B. Brown, D. T. Scadden, V. P. Torchilin, M. G. Bawendi, D. Fukumura, and R. K. Jain, "Quantum dots spectrally distinguish multiple species within the tumor milieu in vivo," *Nat. Med.* **11**, 678-82 (2005).
2. X. Wu, H. Liu, J. Liu, K. N. Haley, J. A. Treadway, J. P. Larson, N. Ge, F. Peale, and M. P. Bruchez, "Immunofluorescent labeling of cancer marker Her2 and other cellular targets with semiconductor quantum dots," *Nat. Biotechnol.* **21**, 41-6 (2003).
3. W. Cai, D.-W. Shin, K. Chen, O. Gheysens, Q. Cao, S. X. Wang, S. S. Gambhir, and X. Chen, "Peptide-labeled near-infrared quantum dots for imaging tumor vasculature in living subjects," *Nano. Lett.* **6**, 669-76 (2006).
4. F. G. Blankenberg, "In vivo detection of apoptosis," *J. Nucl. Med.* **49** Suppl 2, 81S-95S (2008).
5. X. Gao, W. C. W. Chan, and S. Nie, "Quantum-dot nanocrystals for ultrasensitive biological labeling and multicolor optical encoding," *J. Biomed. Opt.* **7**, 532-7 (2002).
6. I. L. Medintz, H. T. Uyeda, E. R. Goldman, and H. Mattoussi, "Quantum dot bioconjugates for imaging, labelling and sensing," *Nat. Mater.* **4**, 435-46 (2005).
7. A. P. Alivisatos, W. Gu, and C. Larabell, "Quantum dots as cellular probes," *Annu Rev Biomed. Eng.* **7**, 55-76 (2005).
8. C. Sun, C. Carpenter, G. Pratx, and L. Xing, "Facile Synthesis of Amine-Functionalized Eu³⁺-Doped La(OH)₃ Nanophosphors for Bioimaging," *Nanoscale Res Lett.* **6**(24), (2011).
9. H. Chander, "Development of nanophosphors - A review," *Mat Sci Eng R.* **49**, 113-155 (2005).
10. J. Shen, L.-D. Sun, and C.-H. Yan, "Luminescent rare earth nanomaterials for bioprobe applications," *Dalton Trans.* , 5687-97 (2008).

11. C. M. Carpenter, C. Sun, G. Pratz, R. Rao, and L. Xing, "Hybrid x-ray/optical luminescence imaging: characterization of experimental conditions," *Med. Phys.* **37**, 4011-8 (2010).
12. G. Pratz, C. Carpenter, C. Sun, and L. Xing, "X-Ray luminescence computed tomography via selective excitation: A feasibility study," *IEEE Trans. Med. Imaging* **29**, 1992-1999 (2010).
13. C. Sun, G. Pratz, C. M. Carpenter, H. Liu, Z. Cheng, S. S. Gambhir, and L. Xing, "Synthesis and radioluminescence of PEGylated Eu(3+) -doped nanophosphors as bioimaging probes," *Adv. Mater.* **23**, H195-9 (2011).
14. H. Liu, X. Zhang, B. Xing, P. Han, S. S. Gambhir, and Z. Cheng, "Radiation-luminescence-excited quantum dots for in vivo multiplexed optical imaging," *Small* **6**, 1087-91 (2010).
15. R. S. Dothager, R. J. Goiffon, E. Jackson, S. Harpstrite, and D. Piwnica-Worms, "Cerenkov radiation energy transfer (CRET) imaging: a novel method for optical imaging of PET isotopes in biological systems," *PLoS One* **5**, e13300 (2010).
16. M. A. Lewis, V. D. Kodibagkar, O. K. Öz, and R. P. Mason, "On the potential for molecular imaging with Cerenkov luminescence," *Opt. Lett.* **35**, 3889-91 (2010).
17. J. Axelsson, S. C. Davis, D. J. Gladstone, and B. W. Pogue, "Cerenkov emission induced by external beam radiation stimulates molecular fluorescence," *Med. Phys.* **38**, 4127-32 (2011).

1. Introduction

The application of luminescent nanoparticles, such as quantum dots, in diagnostic molecular imaging is receiving much attention due to the potential to improve the differentiation between normal and malignant tissue by identifying signatures of disease [1]. For example, multicolored quantum dots enable the ability to probe multiple signatures of disease simultaneously; this is recognized to be potentially more beneficial than visualizing a single species [2]. Examples of these molecular markers include the $\alpha_v\beta_3$ integrin and VEGF receptors as indicators for vascular angiogenesis [3], and the translocation of phosphatidylserine for apoptosis [4]. The advantage of nanoparticles in this context is that they may be tuned to emit at varying wavelengths, without severely altering their physical structure [5]. Although quantum dots have been investigated extensively for biological applications [6, 7], nanophosphors have been relatively ignored. Like quantum dots, nanophosphors have high quantum efficiencies, sharp emission peaks, high photostability, and emission wavelength tunability [8, 9]. Nanophosphors have a distinct advantage in that they may emit light when irradiated by ionizing radiation, a process called radioluminescence. This work demonstrates the multiplexing potential of these nanophosphors, using an exemplary nanophosphor system.

While radioluminescence of phosphor material has long been used in radiation detectors, the use of radioluminescent nanophosphors (RLNPs) in biological contexts is just beginning to be explored [10]. Novel applications currently under investigation for radioluminescent imaging (RLI) include direct biological feedback of molecular changes and tumor burden during radiation treatment. This information may be used as a means to enhance radiation treatment efficacy. In addition, RLI may be used to probe molecular information at a superior resolution to other molecular imaging modalities, such as Fluorescence Molecular Tomography (FMT), Positron Emission Tomography (PET), and Single Photon Computed Emission Tomography (SPECT), by collimating the excitation X-ray beam. This high-resolution technique, called X-ray Luminescence (Computed) Tomography (XLCT), utilizes narrowly-collimated X-ray beams to resolve deep-seated RLNPs. This is made possible because of the very low X-ray scatter in small-animals [11, 12].

This study demonstrates the potential use of RLNPs doped with different rare-earth luminescent centers to enable multiplexed RLI after excitation by ionizing radiation. In

particular, it demonstrates the ability to recover the concentrations of each RLNP from multispectral images of the subject. To highlight the flexibility of this technique, multiplexed imaging was demonstrated using two different excitation schemes: radiopharmaceuticals (^{18}F) and X-ray radiation.

2. Methods

2.1 Imaging hardware

A custom imaging system was built to image and measure the concentrations of the nanophosphor contrast agents. A 512x512 pixel back-illuminated deep-cooled (-70C) CCD camera (ProEM, Princeton Instruments, Trenton, NJ) was outfitted with a F/#0.95 imaging lens (DO-5095, Navitar, Rochester, NY), and leaded glass was placed above the subject. Optical bandpass filters (546nm \pm 10nm for Tb^{3+} doped RLNPs, 700nm \pm 20nm for Eu^{3+} doped RLNPs; Andover Corporation, Salem, NH) were placed in front of the camera lens to selectively collect emitted light in the unique spectral regions. A motorized platform adjusted the working distance of the camera to the subject and controlled the field of view. This imaging box was placed in the path of a superficial X-ray unit (Pantax Therapax, East Haven, CT), with voltage and current set to the X-ray tube 90keV and 10mA. This system was operated remotely from the control room of the X-ray unit, outside the X-ray room [11].

Optical spectra from the RLNPs (Fig. 1(a) & Fig. 1 (b)) was collected by measuring the emission of dry powder samples in cuvettes. The distal end of a 10m 400 μm optical fiber was placed in contact with the side of cuvettes containing each sample, while the proximal end was attached to a spectrophotometer (SP2150, Princeton Instruments) connected to the CCD camera, which was operated from the X-ray control room. Optical emission spectra within the visible and NIR range was acquired with custom software written in Labview (National Instruments, Austin, TX). By acquiring vertical spectral bins for each wavelength, image processing was used to remove X-ray noise, which stochastically appeared in the CCD. Alternatively, Cerenkov spectra was recorded by fitting a quadratic curve to data collected from a commercial imaging system (IVIS Spectrum, Perkin Elmer, Waltham, MA). The signal emitted from the radiopharmaceuticals was verified via a small animal Positron Emission Tomography (PET) system (Siemens R4 Micro-PET, Malvern, PA).

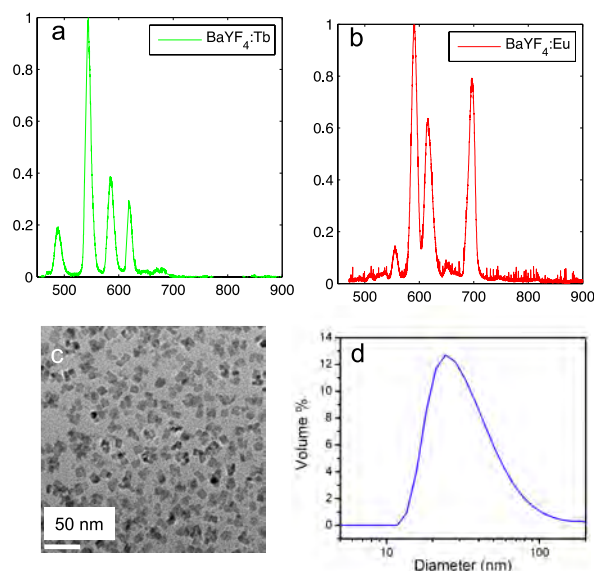


Fig 1. (a) Radioluminescent spectrum of the $\text{Ba}_{0.55}\text{Y}_{0.3}\text{F}_2\text{:Tb}^{3+}$ particles, which emit primarily in the green. (b) Radioluminescent spectrum of the $\text{Ba}_{0.55}\text{Y}_{0.3}\text{F}_2\text{:Eu}^{3+}$ particles, which emit primarily in the red and near-infrared. (c) Transmission electron microscopy image of the RLNPs. (d) Hydrodynamic size distribution of the RLNPs as determined by dynamic light scattering.

2.2 Contrast agent synthesis

In this study, we demonstrate two possible dopants, europium (Eu^{3+}) and terbium (Tb^{3+}). A detailed description of the synthesis of these particles was recently described by Sun et al. [13]. The host barium yttrium fluoride ($\text{Ba}_{0.55}\text{Y}_{0.3}\text{F}_2$) nanocrystals were doped with either terbium (0.5%) or europium (0.5%) to produce emission maxima at 541nm and 586nm, respectively. Both RLNPs emitted additional spectral peaks towards the near infrared (NIR) at 629nm and 692nm, respectively, as seen from Fig. 1(a) & Fig. 1(b); these emission wavelengths enable imaging of deeper structures. The unique signatures emitted by each phosphor enabled the ability to perform multiplexing. The surfaces of the RLNPs were modified with poly(ethylene glycol) (PEG, MW 600) through a ligand exchange process to achieve colloidal stability in aqueous solutions. These phosphors can be functionalized with a biotin linker bound to the PEG. Shown in Fig. 1(c) is the transmission electron microscopy (TEM) image of this RLNP platform with a cubic morphology and mean particle size of 14nm. The hydrodynamic size was determined by dynamic light scattering (DLS); particles with hydrodynamic size of ~27nm were the most common, as shown in Fig. 1(d).

2.3 Image multiplexing

To form images of the concentrations, c , of each of these particles, the light emitted, ϕ , was recorded over the several optical spectral regions defined by filter f_1 and filter f_2 to form images of the subject, $i_1 = \phi(f_1)$ and $i_2 = \phi(f_2)$. These images, and the pre-recorded reference spectra, ϵ , for $\text{Ba}_{0.55}\text{Y}_{0.3}\text{F}_2\text{:Tb}^{3+}$, (ϵ_{Tb}), $\text{Ba}_{0.55}\text{Y}_{0.3}\text{F}_2\text{:Eu}^{3+}$, (ϵ_{Eu}), and the Cerenkov luminescence, (ϵ_{Ch}), were input into a linear-least squares algorithm to extract the contributions from each nanophosphor. Reference spectra was collected with a calibrated spectrometer, thus enabling a quantitative comparison between the nanophosphors. Since Cerenkov light was generated from the F-18 radiotracer, it was necessary to account for the Cerenkov component for the experiments involving radiotracer excitation. For experiments involving X-ray excitation, the Cerenkov component was not present, since Cerenkov light arises from photons emitted from highly-energetic charged particles that are greater than the energy of charged particles created during X-ray excitation.

2.4 Experimental demonstration

To validate the ability of this method to image multiple nanophosphors simultaneously, five phantoms (99% DI water, 1% agarose) were fabricated containing Tb^{3+} and Eu^{3+} doped RLNPs of linearly varying concentrations (in units of mg/ml) and mixed in the following ratios: (0:10; 2.5:7.5; 5:5; 7.5:2.5; and 10:0). To demonstrate this method in a pre-clinical mouse model, four batches of RLNPs were each mixed with 52 μCi (Curie) of activity of 18-F and Matrigel (BD Biosciences, Sparks, MD) and injected into both forelegs and flanks of a nude mouse, with Eu^{3+} -doped RLNPs (Eu) only on the left foreleg, Tb^{3+} -doped RLNPs (Tb) only on the left flank, an equal mixture of Eu^{3+} -doped RLNPs and Tb^{3+} -doped RLNPs (Mix) on the right flank, and an inactive undoped nanophosphor control (Ctrl) on the right foreleg. For the radioisotope-excited experiment, the subject was imaged immediately after injection. For the X-ray-excited experiment several days later (after the 18-F had fully decayed), the same subject was placed in the imaging apparatus and excited by a 90keV X-ray source, which was transmitted through the dark-box. The same subject was imaged with the X-ray and radiopharmaceutical excitation on separate days to allow the radioisotope to decay

thoroughly. Concentration images of the animals were normalized due to the lack of recorded tissue optical properties.

3. Results

3.1 Phantom validation

Fig. 2(a) displays the unmixed images for linearly increasing (top-to-bottom) amounts of Tb^{3+} -doped RLNPs on the left, and decreasing (top-to-bottom) Eu^{3+} -doped RLNPs on the right, at each concentration. The median values for each region of interest were plotted with respect to concentration. Fig. 2(b) shows the median raw signal detected from each nanophosphor concentration. Fig. 2(c) demonstrates this method's efficacy in separating the nanophosphors; the correlation between the samples was ($r = -0.98$).

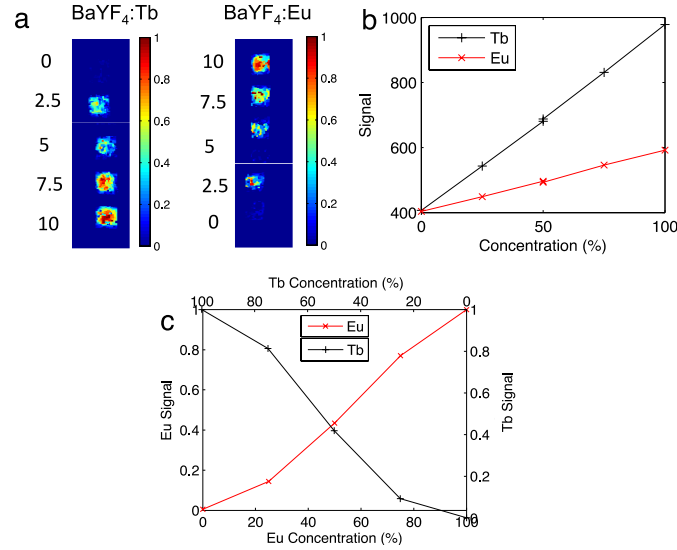


Fig 2. (a) Shown are the $\text{Ba}_{0.55}\text{Y}_{0.3}\text{F}_2:\text{Tb}^{3+}$ and $\text{Ba}_{0.55}\text{Y}_{0.3}\text{F}_2:\text{Eu}^{3+}$ phosphor concentrations with increasing/decreasing concentration (top-to-bottom) of $\text{Ba}_{0.55}\text{Y}_{0.3}\text{F}_2:\text{Tb}^{3+}$ / $\text{Ba}_{0.55}\text{Y}_{0.3}\text{F}_2:\text{Eu}^{3+}$, respectively. (b) The raw signal detected for each respective nanophosphor. (c) The relative median recovered concentration in each ROI plotted with respect to concentration.

3.2 Animal phantom validation

The locations of the subcutaneously injected RLNPs are shown in Fig. 3(a). The feasibility of this method in a pre-clinical subject with X-ray excitation is shown in Fig. 3(b)-(d). Tb^{3+} -doped RLNPs embedded in the left and right flanks are shown successfully recovered in Fig. 3(b). The Eu^{3+} -doped RLNPs in the left foreleg and the right flank are shown successfully recovered in Fig. 3(c). As a control, inactive RLNPs in the right foreleg did not luminesce. Fig. 3(d) shows the results of the spectral unmixing algorithm, with the Eu^{3+} -doped RLNPs shown in red, and the Tb^{3+} -doped RLNP shown in green. The yellow in the multiplexed image indicates the presence of both types of nanophosphors.

The results of RLI with radiopharmaceutical excitation are shown in Fig. 4 (performed several days prior but on the same mouse as Fig. 3). The PET image of the four injected regions of ^{18}F with active and inactive particles is shown in Fig. 4(a); this image is included for spatial validation. All corners illuminate in the PET image because of the injection of ^{18}F with all particles. The unmixed Cerenkov image is shown in Fig. 4(b). Note the Cerenkov signal in each region, due to the injection of ^{18}F in each region; these correspond to the

regions in the PET image. In particular, note the recovery of the Cerenkov light in the right foreleg, which contained the inactive control $\text{Ba}_{0.55}\text{Y}_{0.3}\text{F}_2$ nanocrystals along with ^{18}F . The successful recovery of Tb^{3+} -doped RLNPs and Eu^{3+} -doped RLNPs is demonstrated in Fig. 4c-d. The spectrally unmixed fused image is shown in Fig. 4e, with Eu^{3+} -doped RLNPs in red, Tb^{3+} -doped RLNPs in green, and Cerenkov light in blue. Note that the doped nanoparticles did not emit in the control foreleg.

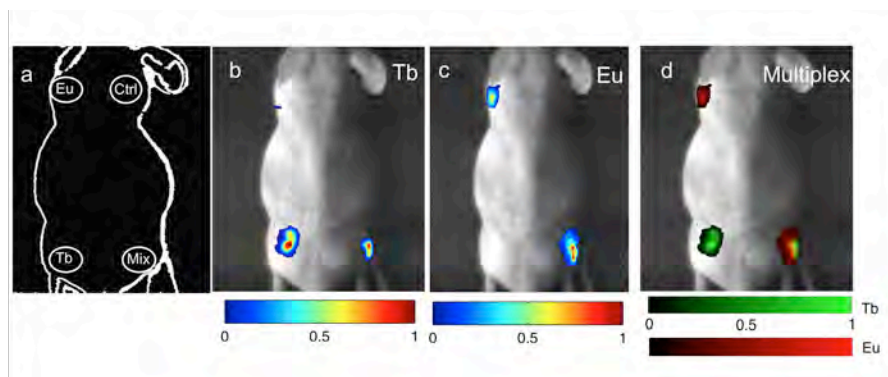


Fig 3. X-ray Luminescence: (a) Schematic of the locations of each type of RLNP. The inactive particles are indicated with the abbreviation (Ctrl). (b,c) The unmixed signal from the $\text{Ba}_{0.55}\text{Y}_{0.3}\text{F}_2\text{:Tb}$ and $\text{Ba}_{0.55}\text{Y}_{0.3}\text{F}_2\text{:Eu}$ particles, respectively. (d) The unmixed multiplexed image with colorbars for the relative concentrations of $\text{Ba}_{0.55}\text{Y}_{0.3}\text{F}_2\text{:Tb}$ and $\text{Ba}_{0.55}\text{Y}_{0.3}\text{F}_2\text{:Eu}$.

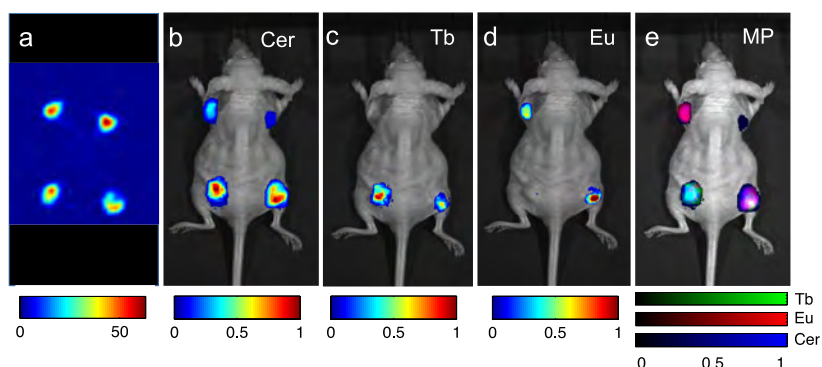


Fig 4. Radiopharmaceutical luminescence: (a) Positron emission tomography image of the relevant RLNPs. (b) The unmixed signal from Cerenkov emission. (c,d) Unmixed signal from the $\text{Ba}_{0.55}\text{Y}_{0.3}\text{F}_2\text{:Tb}^{3+}$ particles and $\text{Ba}_{0.55}\text{Y}_{0.3}\text{F}_2\text{:Eu}^{3+}$ particles, respectively. (e) Unmixed multiplexed image with colorbars for the relative contributions of $\text{Ba}_{0.55}\text{Y}_{0.3}\text{F}_2\text{:Tb}^{3+}$, $\text{Ba}_{0.55}\text{Y}_{0.3}\text{F}_2\text{:Eu}^{3+}$, and Cerenkov emission.

4. Discussion and conclusions

The methods outlined in this paper demonstrate the ability of this particle system to simultaneously be used for multiple types of RLI; these may then be attached to distinct molecular targets. RLNPs may become an important analog to the current tools dedicated to pre-clinical imaging due to their great versatility. In one application, if injected with a radiopharmaceutical, the nanoparticles introduced in this study would enable multiple-targeting; this could prove to be an important method to identify the kinetics or accumulation after drug-injection. These RLNPs may also aid in the down-conversion of Cerenkov light emitted from the radiopharmaceutical [14, 15, 16, 17]. In another application, these RLNPs may be used in conjunction with X-ray luminescence computed tomography [12] to recover high-resolution molecular-specific images. In yet another application, this RLNP system may aid in the on-line identification of response to radiation therapy. Through targeting of

molecular markers specific for tumors, this method could provide feedback during therapy as to the status of treatment; the penetration of high-energy photons in conjunction with a light detector would ensure the ability to reach a larger depth in tissue.

In conclusion, we have demonstrated a nanoparticle platform for radioluminescence imaging which may be used to image multiple nanophosphors simultaneously using both radiopharmaceutical and X-ray irradiation. We showed an inverse relationship between concentrations of the types of RLNPs, which showed successful separation of the contribution from the two emission signals. We then demonstrated this technology in a small-animal model.

Acknowledgements

The authors gratefully acknowledge the Department of Defense Breast Cancer Research Programs W81XWH-10-1-0506 (CMC), W81XWH-11-1-0087 (CS), and W81XWH-11-1-0070 (GP), the National Institutes of Health ICMIC P50CA114747, and the Center for Biomedical Imaging at Stanford-CBIS (CMC) for funding.

1 Hybrid x-ray/optical luminescence imaging: Characterization of experimental 2 conditions

3 C. M. Carpenter,^{a)} C. Sun, and G. Pratz

4 *Department of Radiation Oncology, School of Medicine, Stanford University, Stanford, California 94305*

5 R. Rao

6 *SRI International, Menlo Park, California 94025*

7 L. Xing

8 *Department of Radiation Oncology, School of Medicine, Stanford University, Stanford, California 94305*

9 (Received 21 April 2010; revised 28 May 2010; accepted for publication 6 June 2010;
10 published xx xx xxxx)

11 **Purpose:** The feasibility of x-ray luminescence imaging is investigated using a dual-modality
12 imaging system that merges x-ray and optical imaging. This modality utilizes x-ray activated
13 nanophosphors that luminesce when excited by ionizing photons. By doping phosphors with lan-
14 thanides, which emit light in the visible and near infrared range, the luminescence is suitable for
15 biological applications. This study examines practical aspects of this new modality including phos-
16 phor concentration, light emission linearity, detector damage, and spectral emission characteristics.
17 Finally, the contrast produced by these phosphors is compared to that of x-ray fluoroscopy.

18 **Methods:** Gadolinium and lanthanum oxysulfide phosphors doped with terbium (green) or eu-
19 ropium (red) were studied. The light emission was imaged in a clinical x-ray scanner with a cooled
20 CCD camera and a spectrophotometer; dose measurements were determined with a calibrated
21 dosimeter. Using these properties, in addition to luminescence efficiency values found in the litera-
22 ture for a similar phosphor, minimum concentration calculations are performed. Finally, a 2.5 cm
23 agar phantom with a 1 cm diameter cylindrical phosphor-filled inclusion (diluted at 10 mg/ml) is
24 imaged to compare x-ray luminescence contrast with x-ray fluoroscopic contrast at a superficial
25 location.

26 **Results:** Dose to the CCD camera in the chosen imaging geometry was measured at less than 0.02
27 cGy/s. Emitted light was found to be linear with dose ($R^2=1$) and concentration ($R^2=1$). Emission
28 peaks for clinical x-ray energies are less than 3 nm full width at half maximum, as expected from
29 lanthanide dopants. The minimum practical concentration necessary to detect luminescent phos-
30 phors is dependent on dose; it is estimated that subpicomolar concentrations are detectable at the
31 surface of the tissue with typical mammographic doses, with the minimum detectable concentration
32 increasing with depth and decreasing with dose. In a reflection geometry, x-ray luminescence had
33 nearly a 430-fold greater contrast to background than x-ray fluoroscopy.

34 **Conclusions:** X-ray luminescence has the potential to be a promising new modality for enabling
35 molecular imaging within x-ray scanners. Although much work needs to be done to ensure bio-
36 compatibility of x-ray exciting phosphors, the benefits of this modality, highlighted in this work,
37 encourage further study. © 2010 American Association of Physicists in Medicine.

38 [DOI: 10.1118/1.3457332]

39 I. INTRODUCTION

AQ: 40 Molecular imaging promises increased sensitivity and speci-
#1 41 ficity to disease compared to traditional anatomical imaging
42 modalities. The information gained from molecular imaging
43 has the potential to provide patient-specific selection of
44 therapy, improved prediction of outcomes, and increased
45 treatment efficacy.¹ X-ray radiography and computed tomog-
46 raphy (CT) are commonly used anatomical imaging modali-
47 ties; however, although they provide invaluable information
48 in the clinic, they have been largely unsuccessful for molecu-
49 lar imaging.² This deficiency is due to their lack of sensitiv-
50 ity to low concentrations of contrast agents; x-ray imaging is
51 commonly believed to be many orders of magnitude less
52 sensitive than optical³ or radionuclide⁴ imaging. This poor

sensitivity arises from the low x-ray stopping power of di- 53
luted contrast agents, which necessitates high concentrations 54
compared to other imaging modalities.² 55

Phosphors are well-established materials used universally 56
in cathode ray tubes and light-emitting diodes for their abil- 57
ity to emit light upon excitation by electrons or photons. 58
Phosphors consist of solid-state crystals, which are typically 59
doped with transition metals or lanthanide ions. These mate- 60
rials form a system optimized to capture higher-energy radia- 61
tion and emit downconverted energy as optical photons. In 62
the context of an x-ray scanner, x-ray photons transfer some 63
or all of their energy to electrons in the solid-state crystal 64
through Compton and photoelectric interactions.⁵ These 65
high-energy electrons progressively lose energy through in- 66
teractions with the atoms, leaving a track of excited electrons 67

behind. When the energy of the excited electrons in the conduction band is reduced to approximately two to three times the band gap, they may migrate into the luminescence center of the phosphor, the dopant, and recombine with holes to emit light.⁶ Thus, this amplification process results in effective quantum efficiencies (photons emitted divided by the photons absorbed), which can be much greater than 1. For example, on the average, 6000 photons are produced for each 100 keV x-ray photon absorbed in one particular gadolinium oxysulfide:terbium phosphor.⁷ The emitted light may then be imaged by sensitive optical detectors.

This paper investigates the use of nanosized inorganic phosphors⁷ as potential biological contrast agents for medical imaging in a combined x-ray/optical instrument. The emission from this contrast agent is evaluated to determine the practicality of this new modality. The implications for this x-ray activated contrast agent are discussed with regard to its potential to enable molecular imaging during fluoroscopy, x-ray CT, or projection x-ray imaging.

II. METHODS

II.A. Phosphor fabrication

Trivalent europium (Eu) or terbium (Tb) activated gadolinium oxysulfides (GOSs) or lanthanum oxysulfides (LOSs) were synthesized using appropriate rare earth nitrates (99.99% pure) with two standard methods: The gel-polymer combustion process and the combination capping process,⁶ respectively. After preparation, samples were heat treated at 500–600 °C for 1–3 h to aid the migration of the dopant into the crystal lattice structures. Next, the powders were ball milled with glass beads (10 μm) in the presence of the appropriate surfactant for 2–3 h.

II.B. Spectroscopy and imaging of phosphor characteristics

To facilitate spectroscopy and imaging for the analysis of the properties of the phosphors, dry phosphor was placed in plastic test tubes. For spectroscopy, the distal end of a 10 m–400 μm optical fiber was placed in contact with the side of the test tube, while the proximal end was attached to a spectrophotometer (Jaz, Ocean Optics, Dunedin, FL), which was operated from the x-ray control room. Optical emission spectra across the visible and near infrared (NIR) range were acquired with the SPECTRASUITE (Ocean Optics) software package. Imaging was performed with a 512×512 pixel backilluminated CCD camera (CCD temperature maintained at –70 °C) with a F1.4 imaging lens, exposure times varying from <1 to 60 s, and the lens aperture fully open. During data acquisition, the imaging camera was shielded with lead bricks and placed 15–20 cm outside the direct field of radiation to protect from ionizing radiation. The optics setup was placed inside a light-tight box to eliminate ambient room light. A schematic of this imaging setup is shown in Fig. 1(a), and a photograph of the setup during experimental imaging is shown in Fig. 1(b).

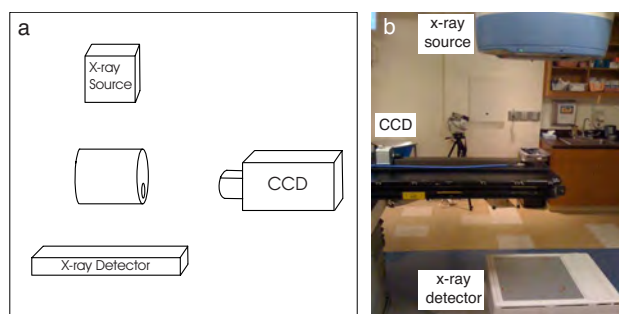


FIG. 1. (a) Schematic of the experimental setup including the CCD camera, the x-ray source and detector, and the sample. (b) Photograph of the imaging setup.

A cone beam computed tomography (CBCT) system (Acuity, Varian Medical Systems, Palo Alto, CA) was used to irradiate the sample. This system allows both CBCT and fluoroscopy at various tube voltages between 70 and 125 kV. This system was operated in fluoroscopy mode to enable continuous irradiation from a constant geometry.

II.C. Concentration evaluation

Minimum detectable concentrations were calculated, assuming a superficial location of the phosphor contrast agent (i.e., no signal loss due to tissue absorption). Including light detection losses L , the light detected Φ is

$$\Phi = \Gamma \cdot D \cdot c \cdot L, \quad (1)$$

where Γ is the emitted light efficiency, D is the dose, and c is the concentration of the phosphor. From Ref. 8, the emitted light efficiency (in a lanthanum oxysulfide:terbium phosphor) is 1.39×10^{15} optical photons/(Gy mg). We assumed 99% detection loss due to suboptimal optical collection geometry. Signal below a signal-to-noise ratio (SNR) of 10 (assuming shot-noise limited detection) was assumed to be too low to detect. To calculate the molar concentration, we assumed a spherical 10 nm diameter nanoparticle consisting of hexagonal-structured phosphors with lattice constants of $a=4.046 \text{ \AA}$ and $c=6.951 \text{ \AA}$ (Ref. 9) and density of 5.5 g/cm^3 .

II.D. Optical phantom fabrication and imaging

A small-animal sized tissue-simulating phantom was fabricated for this study. The cylindrical phantom measured 2.5 cm in diameter×4.5 cm in height, with a $1 \times 2.5 \text{ cm}^2$ cylindrical inclusion. The phantom was made from 1% agar with homogeneous optical properties using titanium oxide for scatter and India Ink for absorption using methods common to diffuse optical phantoms.¹¹ The optical properties were determined by a previously established system¹² to be $\mu_a=0.0025 \text{ mm}^{-1}$ and $\mu_s'=0.77 \text{ mm}^{-1}$ at 630. Micrometer-sized GOS:Eu phosphor particles were added to the inclusion at a concentration of 10 mg/ml, and no phosphor was added to the background. This phantom was imaged with an electron multiplied (EM)-CCD (Hamamatsu ImageEM 9100-13, Hamamatsu, Japan) with a 512

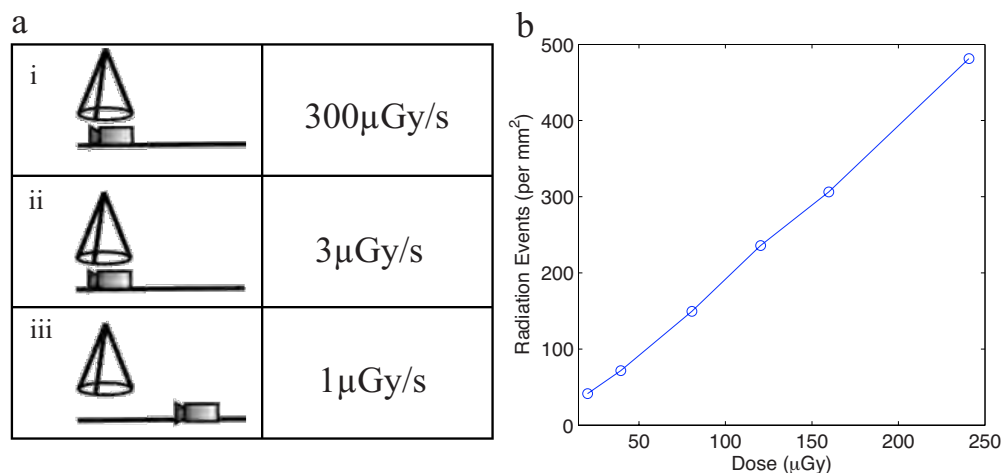


FIG. 2. (a) Radiation dose on detector for three different configurations: (i) Direct irradiation, (ii) direct irradiation with lead shielding (5 mm on top, 50 mm on each side), and (iii) indirect irradiation with lead shielding. (b) Radiation events per area per dose.

160 $\times 512$ pixel sensor cooled at -70°C , with a F1.4 imaging
 161 lens, with exposure of times less of 2 s, gain at half-
 162 maximum, and the lens aperture fully open.

163 III. RESULTS

164 III.A. CCD interaction with ionizing radiation

165 To ensure that the CCD camera would not be damaged
 166 from the ionizing radiation, an ionization chamber (PTW
 167 Farmer 30010, PTW Freiberg GMBH, Germany) was placed
 168 in the radiation field to determine the dose to air in the vi-
 169 cinity of the CCD. Several locations along the patient bed
 170 were measured to determine dose rate, as indicated in Fig.
 171 2(a). Under direct radiation, the dose was nearly
 172 300 $\mu\text{Gy/s}$; this dose rate was reduced by two orders of
 173 magnitude by placing lead around the chamber, and further
 174 by twofold, to 1.5 $\mu\text{Gy/s}$, by moving the chamber 15 cm
 175 out of the radiation field. This rate deposits dose well below
 176 levels that would likely damage the CCD.

177 To investigate camera damage further, we investigated the
 178 lingering effects of radiation on the CCD. The interaction of
 179 an x-ray photon with the CCD camera appears in the image
 180 as a bright pixel at near-maximum intensity. These hot pixels
 181 appear similar to cosmic ray interactions, which are common
 182 with CCD cameras. We investigated the incidence of these
 183 events for a typical setup using a CCD to radiation field
 184 distance of 15 cm and 6 mm of lead shielding above the
 185 camera to protect from x-ray collimator leakage. Radiation
 186 events were determined by performing an intensity threshold
 187 on an image acquired with the lens cap on. It is clear from
 188 Fig. 2(b) that the number of radiation events is linear with
 189 dose, and thus there were no lingering effects from the ra-
 190 diation. To improve image quality, denoising strategies may
 191 be employed utilizing this linearity, such as an automatic
 192 selection of a hot-pixel threshold, which is dependent on
 193 camera dose. Further consideration of the damage limits of
 194 CCD cameras is given in Sec. IV.

III.B. Phosphor characterization

III.B.1. Spectral emission

A large body of knowledge exists on phosphors due to
 over a half-century of study of optimizing phosphors for
 such applications as light-emitting diodes, cathode ray tubes,
 and scintillators for medical imaging. This work has resulted
 in a library of crystals and dopants from which one may
 select an emission wavelength that is ideal for a particular
 application.⁶ We investigated the feasibility of GOS phos-
 phors, which were doped with either terbium (GOS:Tb) or
 europium (GOS:Eu), because of their absorption K-edge in
 the diagnostic energy regime at approximately 50 keV.¹³ Fig-
 ure 3(a) shows the emission of these phosphors under 100
 kV x-ray irradiation. The GOS:Tb phosphor had a maximum
 peak emission of 545 nm in green, whereas the GOS:Eu
 phosphor had several peaks of longer wavelengths in the
 NIR, including 596, 618, 627, and 707 nm, with an emission
 maximum at 627 nm. The flexibility enabled by modifying
 the dopant is of great value for matching the emission wave-
 length to a particular application, such as the absorption peak
 of a phototherapeutic drug,¹⁴ or the tissue absorption mini-
 mum for optical imaging in deep tissue.¹⁵

III.B.2. Light output vs dose

To determine the linearity of light output from phosphor,
 GOS:Tb was dispersed in a cuvette containing 1% agar at a
 concentration of 10 mg/ml. The phosphor solution was
 placed at the same source-target distance as the ionization
 chamber. The x-ray system was operated in fluoroscopy
 mode and the tube voltage was set to 100kV. The dose was
 linearly increased by two methods. First, the tube current
 was increased from 5 to 20 mA with a constant tube voltage.
 Second, the tube voltage and current remained constant, and
 dose was linearly increased by adjusting the irradiation time.
 Images were acquired with a CCD camera, with the exposure

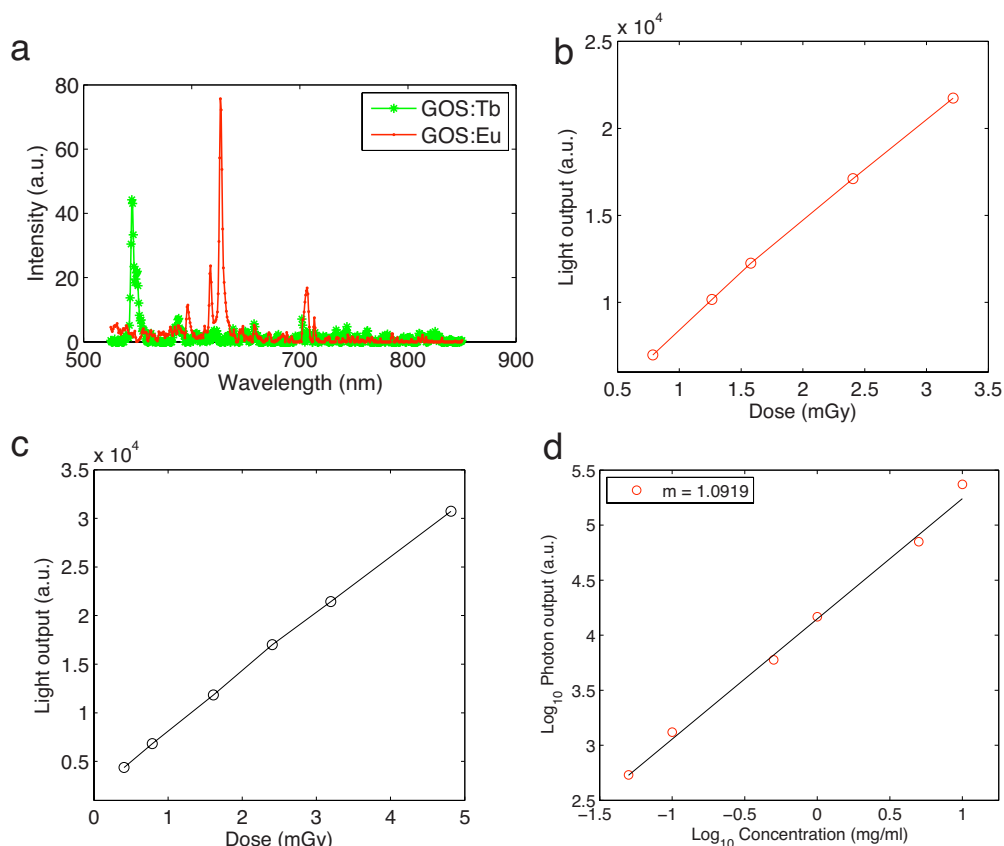


FIG. 3. (a) Emission spectra of GOS phosphors under x-ray excitation. GOS:Tb, with an emission peak at 545 nm, is labeled with asterisks (*), and GOS:Eu, with emission peaks at 596, 618, 627, and 707 nm. (b) X-ray induced GOS:Tb Photon output vs dose with dose varied by increasing tube current. (c) Photon output vs dose with dose varied by increasing irradiation time. For both methods, photon output is linear with dose shown in terms of current ($r=1$, $p<0.001$, $R^2=1$). (d) Photon output vs concentration for the GOS:Eu phosphor. Concentrations were measured via microcuvette and dispersed in 1% agar. Photon output is linear with concentration ($r=0.99$, $p=1.9\times 10^{-7}$).

time optimized. All measurements were denoised for hot spots and identical regions of interest (ROIs) were selected for analysis.

AQ: #3 Both current/dose and time/dose linearity were confirmed by running a linear correlation analysis (correlation coefficient of 1.0, $p<0.001$). Figure 3(b) shows the linearity in dose using the first method, which showed significant linearity (correlation coefficient of 1.0, $p<0.001$), while Fig. 3(c) confirms linearity with the second method (correlation coefficient of 1.0, $p<0.001$).

III.B.3. Light output vs concentration

To assess the light output due to various phosphor concentrations, dilutions of GOS:Eu phosphors from 5 $\mu\text{g}/\text{ml}$ to 10 mg/ml were dispersed in 1% agar. Cuvettes were placed in a 50 kV, 30 mA x-ray source and imaged with a CCD camera. ROIs were selected to contain similar areas of the cuvettes, and the signal was normalized according to exposure time. Hot spots were removed from the images prior to analysis.

The results shown in Fig. 3(d) demonstrate a strong linearity (linear correlation coefficient of 0.99, $p<0.001$) with a slope of 1.09. The slight departure of the slope from unity is most likely due to errors in selecting identical ROIs for the

different cuvettes and may have resulted in the inclusion of the cuvette wall in the ROI, which exhibited some light piping.

III.C. Minimum detectable concentrations

We calculated the minimum detectable concentration according to the methodology outlined in Sec. II C, for doses ranging from 1 cGy (less than the typical mammographic dose) to 20 Gy (a typical dose delivered in single-dose intra-operative radiation therapy). In addition, we calculated the minimum detectable concentration for several phosphor efficiencies, scaled according to that reported by Kandarakis *et al.*⁸ (i.e., 100% is equivalent to the efficiency reported). Figure 4 shows the minimum detectable concentrations for these scenarios. According to these calculations, picomolar (ng/ml) concentrations are detectable (SNR of 10) with a LOS phosphor for mammographiclike dose, while therapy doses allow femtomolar (pg/ml) concentrations to be detected.

III.D. Contrast comparison between x-ray/optical and fluoroscopy

The recovered contrast between an inclusion with phosphor and a background without phosphor was investigated to

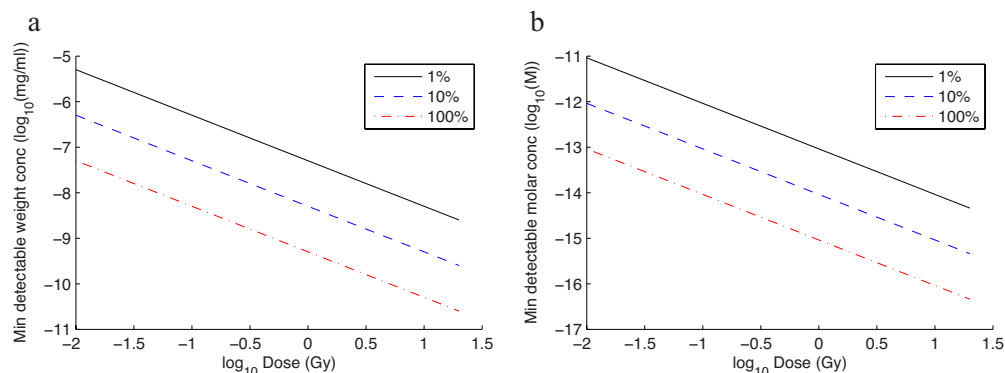


FIG. 4. Minimum estimated phosphor concentrations calculated from the literature and our own data. Lines represent phosphor luminescence efficiencies; the 100% line is based on efficiency data from a La₂O₂S:Tb phosphor reported by Kandarakis *et al.* (a) Minimum weight concentration (in mg/ml) vs dose (Gy). (b) Minimum molar concentration (in M) vs dose (Gy).

compare the contrast differences between x-ray fluoroscopy and x-ray/optical luminescence imaging in the small-animal imaging phantom described in Sec. II D. The phantom was imaged during fluoroscopy operation with the tube voltage at 100 kV and the tube current at 10 mA. The x-ray source was placed above the phantom to evenly irradiate the volume. The CCD camera was placed within 15 cm of the phantom and oriented orthogonal to the direction of irradiation. The fluoroscopy image was taken simultaneously. It is important to note that gadolinium is a strong absorber of 100 keV x-ray energy, with a mass attenuation coefficient of 3.109 cm²/g (compared to common x-ray contrast agents such as barium at 2.196 cm²/g and iodine at 1.942 cm²/g). Since gadolinium has a higher mass attenuation coefficient for x-ray photons than water (mass attenuation coefficient of 0.1707 cm²/g), it should exhibit slight contrast.

The images from the phantom are shown in Fig. 5. Figure 5(a) shows a white light image taken by the CCD camera with background illumination from the room lights. The corresponding fluoroscopy image is shown in Fig. 5(b). The phosphor inclusion is indicated by the red arrow and shows slight increased x-ray absorption (the smaller dark circle is a bolt hole in the aluminum optical table). Figure 5(c) shows a raw optical image taken of the x-ray luminescent phosphor. This image is overlaid on the white light image in Fig. 5(d). The contrast between the inclusion and the background is very slight, at 0.6% for the fluoroscopy image, while it is over 260% for the luminescence image. In addition, the signal-to-noise ratio for the phosphor emission was 23 vs 2.4 for the fluoroscopy image.

IV. DISCUSSION

We found that dose distributed to the shielded camera was measured at less than 3 μGy/s when the camera was positioned at the isocenter and the x-ray tube voltage was 100 keV with the tube current at 20 mA. Although this dose is low, estimating a damage threshold is difficult for CCDs because damage is design/manufacture-specific and is dependent on environmental conditions (for a more thorough overview, see Ref. 16). It is well recognized that the largest

radiation threat to the operation of a CCD is the bombardment by highly energetic heavy particles, such as protons and neutrons. These particles contribute most to CCD damage through impact displacements of silicon atoms which create semipermanent energy traps. These traps create energy levels which can increase Johnson noise (via promoting valence band electrons to the conduction band), create spurious noise when trapped electrons are released, and alter the operation of transistor gates by altering their flat-band voltage (for a more thorough review, see Refs. 17 and 18). Although the probability of creating protons and neutrons is extremely low at diagnostic x-ray energies studied here, it is relevant for therapeutic energies in the MV range. Cumulative doses are also important because of the increased probability for a high-energy photon interaction. It has been reported that total

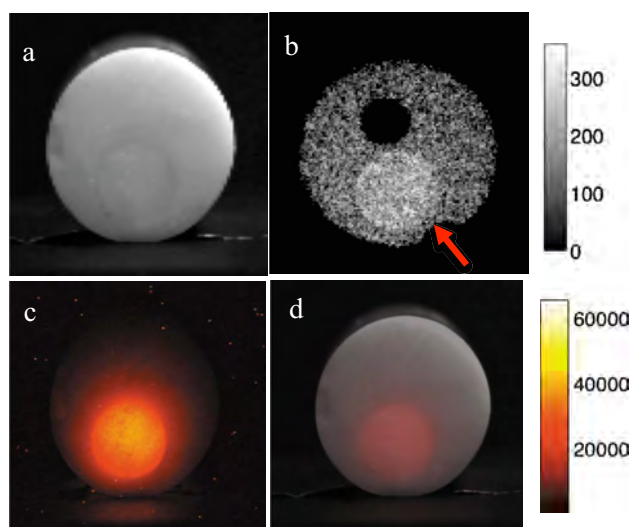


FIG. 5. Agar imaging phantom with embedded phosphors and tissue emulating optical properties. (a) White-light optical image. (b) Projection fluoroscopy image (note the distinction between the phosphor inclusion—indicated by the red arrow—around 300 units, compared to the black circle caused by a screw hole in the optical table supporting the phantom). (c) Optical emission from the phantom. (d) Overlay of the white light image (a) and the light emission (c).

doses above about 25 and 100 Gy are considered thresholds for increased noise and permanent damage, respectively¹⁹ (though again, these numbers are highly camera-dependent). Thus, it is important to keep radiation dose on the CCD as low as possible to minimize cumulative dose and increase the life of the camera. The dose deposited in this experiment of 1–3 $\mu\text{Gy/s}$ is minimal, and damage due to radiation should be insignificant in the lifetime of the camera.

The lanthanide dopants examined in this study are known to have extremely sharp peaks; for example, we measured the full width at half maximum (FWHM) of the GOS:Tb sample at 3 nm, while the GOS:Eu sample had a FWHM of 2 nm for the largest peak [both shown in Fig. 3(a)]. This is in contrast to common fluorophores like indocyanine green, which have often have emission peak FWHM of about 60 nm. This enables the possibility of multiplexing contrast agents with very little cross-talk, allowing the simultaneous measurement of several markers for disease.

A major concern of these x-ray excitable phosphor contrast agents is that they require ionizing dose to activate. Thus, lower concentrations of phosphors will necessitate higher doses. We analyzed the practical detection limit of phosphors using the knowledge of concentration and dose linearity and luminescence efficiencies found in the literature for similar nanophosphors. For detection at the surface of tissue, x-ray mammographic dose should be sufficient to allow the detection of picomolar (ng/ml) concentrations of phosphor. This finding is corroborated with our experimental results shown in Fig. 3. If the data in Fig. 3(d) are extrapolated to 10 counts/pixel, adequate signal-to-noise ratio is achieved using an EM-CCD camera (with dark noise of 0.05 counts/pixel for this acquisition). Placing the camera within a few cm (compared to 20 cm in this experiment) would result in the detection of approximately two orders of magnitude more light. Further, if the dose is increased by an order of magnitude [from the 4 mGy dose administered for Fig. 3(d)] to mammography levels, and EM gain is increased to the maximum, concentrations of ng/ml (picomolar) may be realized.

At deeper depths, however, light attenuates rapidly; for example, in breast tissue, a depth of 3 cm would attenuate detected light by approximately three orders of magnitude.²⁰ This would effectively decrease phosphor sensitivity during mammographic dose to nanomolar concentrations. In a radiation oncology setting, however, high doses are delivered to treat disease (such as the 20 Gy single-fraction therapy, which is used during intraoperative radiation therapy²¹). This technique could aid a surgeon and radiation oncologist to identify the distribution of disease around a tumor margin, such as during breast lumpectomy. In this case, the patient would be injected with a phosphor contrast agent before or during surgery, depending on the pharmacokinetics of the tracer. The tracer could be imaged during the first 1% or 10% (e.g., 0.2 or 2 Gy) of the radiotherapy treatment dose, which would provide the clinicians with more confidence about the treatment dose or volume, or enable an adjustment to the dose distribution.

The other area of concern with these particles is biological compatibility. This is an issue for all nanoparticle systems, and much work is being done to develop strategies to ensure stability and compatibility.²² In fact, multiple groups have successfully used upconversion phosphors in biological small-animal models.^{23,24} The increased interest in phosphors should aid in the rapid advancement in biocompatibility, which will aid this modality.

We found that the contrast to background ratio was over 2.5 orders of magnitude higher for optical detection of the luminescent phosphors compared to x-ray fluoroscopy. The actual contrast amplification is much higher since the optical photons emitted from the inclusion exhibit extensive scatter in the background and subsequently are detected by the CCD. These scatter effects would be greatly minimized via modeling of the light propagation. In comparison, x-ray photon scatter is relatively nonexistent so that the signal contribution from the background originating from the inclusion is negligible. Considering the photon scatter should greatly improve the contrast of these phosphors for optical detection compared to fluoroscopy.

Although this work demonstrated the potential of x-ray luminescence imaging for imaging a superficial object, imaging of lesions centimeter deep should be possible, with contrast-resolution limitations depending on tissues' properties, concentration, and nonspecific uptake. The development of deep-tissue x-ray luminescence imaging will require the incorporation of optical tomographic models. With x-ray luminescent imaging, the x-ray source must be modeled in tissue to give an accurate description of dose. There are many sophisticated tools to model dose, such as Monte Carlo or analytical models, which have been shown to be accurate [e.g., within 4% (Ref. 25)] in biological tissues. Concurrent x-ray structural imaging will further improve these calculations. After dose distribution is calculated, tomographic imaging may be performed with a reconstruction model that uses a model of the light propagation in tissue to minimize the difference between calculated and optical measurements. This is very similar to the fluorescence molecular imaging problem.²⁶ Once again, the knowledge of anatomical information will aid the optical reconstruction problem by providing structural detail which may be used to improve optical modeling²⁷ and reconstruction.²⁸

The joint use of x-ray activated phosphors for molecular imaging offers several advantages to x-ray imaging and to all-optical fluorescent imaging. For x-ray imaging, contrast agent imaging is currently limited to high concentrations of nonspecific iodine or barium sulfate. Optimal concentrations for these contrasts have been reported around 300–500 mg/ml.²⁹ These high concentrations are impractical for imaging biological targets.² The ability to image cellular targets would be a great benefit to x-ray imaging, which, despite being the most prominent modality in use in the clinic today, is generally limited to imaging structural anatomy. The use of phosphors combined with the sensitivity of optical imaging allows lower, more biologically feasible concentrations of contrast agents than is currently available with x-ray imaging alone.

The use of x-ray activated phosphors offers three unique advantages to all-optical approaches. First, this dual-modality instrument offers inherent spatial coregistration between anatomical features and optical contrasts. This registration is critical for imaging functional pathology in deep tissue [hence, the need for positron emission tomography (PET)/CT imaging systems].³⁰ Next, the use of x-ray excitation eliminates the optical autofluorescence issue in optical imaging. Since the x-ray excitation spectrum is undetectable with photo-optical detectors, autofluorescence is avoided, which potentially reduces the detection limit for low concentrations. Finally, this technique is also expected to have increased depth performance over optical imaging, because of the high penetration of x-ray photons in tissues. X-ray photons have nearly two orders of magnitude lower effective attenuation coefficient compared to optical photons; this opportunity offers the potential to use clinically available instrumentation as an external source.

V. CONCLUSIONS

This study focused on the instrumentation and material feasibility of inorganic downconversion phosphors toward the realization of x-ray molecular imaging. Significant recent advances in PET,⁴ optical imaging,¹¹ magnetic resonance imaging,¹² and to a lesser extent, single positron emission computed tomography, and ultrasound have invigorated the search for disease-specific protein receptors that may be targeted with imaging agents. This approach has already been applied to numerous pathologies to identify atherosclerosis and thrombosis,³¹ to determine treatment efficacy via apoptosis markers,³² to identify cancer, and to monitor cellular activity. The incorporation of these markers into x-ray imaging may have significant impact on medical imaging.

In this work, we demonstrate, for the first time to our knowledge, the feasibility of using inorganic phosphors to enable optical detection under x-ray irradiation, which may enable x-ray molecular imaging. We first investigated the practical feasibility of operating a CCD within an x-ray excitation field at clinically relevant energies, taking into consideration noise and potential damage. We found that the dose distribution to air was sufficiently low to prevent damage during operation. Additionally, the noise on the CCD due to incoming high-energy irradiation is manageable. We demonstrated the ability of several phosphors to emit light in the optical regime under x-ray excitation. These phosphors should be effective for tuning light output to a specific application. We found that the light output was linearly proportional to both dose and concentration. Future work will focus on quantitative imaging. We calculated minimum detectable concentrations based on these data and values found in literature; these concentrations are sufficient for certain biological imaging applications. Finally, we demonstrated the potential of inorganic phosphors to image lower concentrations than is possible with x-ray alone. We found a 430 times improvement in contrast recovery for optical detection compared to fluoroscopic detection. This improvement is expected to be greater with modeling of photon propagation

and imaging. We envision hybrid x-ray/optical imaging may have significant application in the detection and diagnosis of disease, especially during image-guided intervention.

ACKNOWLEDGMENTS

The authors would like to thank Dr. Catherine Klifa from the University of California, San Francisco for the use of the diffuse optical spectroscopy system. They gratefully acknowledge funding sources from the NSF (Grant No. 0854492), NIH (Grant No. R01 CA133474), and NCI IC-MIC (Grant No. P50 CA114747).

- ^aElectronic mail: colincarpenter@stanford.edu
- ¹F. A. Jaffer and R. Weissleder, "Molecular imaging in the clinical arena," *JAMA, J. Am. Med. Assoc.* **293**(7), 855–862 (2005).
- ²U. Speck, "Contrast agents: X-ray contrast agents and molecular imaging—A contradiction?," *Handb. Exp. Pharmacol.* **185**, 167–175 (2008).
- ³R. Weissleder and M. J. Pittet, "Imaging in the era of molecular oncology," *Nature (London)* **452**(7187), 580–589 (2008).
- ⁴S. S. Gambhir, "Molecular imaging of cancer with positron emission tomography," *Nat. Rev. Cancer* **2**(9), 683–693 (2002).
- ⁵J. Bushberg, J. Seibert, E. Leidholdt, and J. Boone, *The Essential Physics of Medical Imaging*, 2nd ed. (Lippincott Williams & Wilkins, Philadelphia, 2002).
- ⁶W. M. Yen and M. J. Weber, *Inorganic Phosphors: Compositions, Preparation and Optical Properties* (CRC, Boca Raton, FL, 2004).
- ⁷H. Chander, "Development of nanophosphors—A review," *Mater. Sci. Eng. R.* **49**(5), 113–155 (2005).
- ⁸I. Kandarakis, D. Cavouras, G. Panayiotakis, T. Agelis, C. Nomicos, and G. Giakoumakis, "X-ray induced luminescence and spatial resolution of La₂O₂S:Tb phosphor screens," *Phys. Med. Biol.* **41**(2), 297–307 (1996).
- ⁹Y. Jiang, Y. Wu, Y. Xie, and Y. Qian, "Synthesis and characterization of nanocrystalline lanthanide oxysulfide via a La(OH)(3) gel solvothermal route," *J. Am. Ceram. Soc.* **83**(10), 2628–2630 (2000).
- ¹⁰D. Cavouras, I. Kandarakis, T. Maris, G. S. Panayiotakis, and C. D. Nomicos, "Assessment of the gain transfer function of phosphors for application in medical imaging radiation detectors," *Eur. J. Radiol.* **35**(1), 70–77 (2000).
- ¹¹B. W. Pogue and M. S. Patterson, "Review of tissue simulating phantoms for optical spectroscopy, imaging and dosimetry," *J. Biomed. Opt.* **11**(4), 041101 (2006).
- ¹²T. Pham, O. Coquoz, J. Fishkin, E. Anderson, and B. Tromberg, "Broad bandwidth frequency domain instrument for quantitative tissue optical spectroscopy," *Rev. Sci. Instrum.* **71**(6), 2500–2513 (2000).
- ¹³C. W. E. van Eijk, "Radiation detector developments in medical applications: Inorganic scintillators in positron emission tomography," *Radiat. Prot. Dosim.* **129**(1–3), 13–21 (2008).
- ¹⁴W. Chen and J. Zhang, "Using nanoparticles to enable simultaneous radiation and photodynamic therapies for cancer treatment," *J. Nanosci. Nanotechnol.* **6**(4), 1159–1166 (2006).
- ¹⁵J. A. Parrish, "New concepts in therapeutic photomedicine: Photochemistry, optical targeting and the therapeutic window," *J. Invest. Dermatol.* **77**(1), 45–50 (1981).
- ¹⁶J. Pickel, A. Kalma, G. Hopkinson, and C. Marshall, "Radiation effects on photonic imagers—A historical perspective," *IEEE Trans. Nucl. Sci.* **50**(3), 671–688 (2003).
- ¹⁷D. Neamen, *Semiconductor Physics and Devices* (McGraw-Hill, New York, 2002).
- ¹⁸G. Hopkinson, C. Dale, and P. Marshall, "Proton effects in CCDs," *IEEE Trans. Nucl. Sci.* **43**(2), 614–627 (1996).
- ¹⁹C. Marshall and P. Marshall, "CCD radiation effects and test issues for satellite designers," NASA Electronic Parts and Packaging (2003), p. 1053.
- ²⁰D. A. Boas, D. H. Brooks, E. L. Miller, C. A. DiMarzio, M. Kilmer, R. J. Gaudette, and Q. Zhang, "Imaging the body with diffuse optical tomography," *IEEE Signal Process. Mag.* **18**, 57–75 (2001).
- ²¹U. Veronesi, G. Gatti, A. Luini, M. Intra, R. Orecchia, P. Borgen, M. Zelefsky, B. McCormick, and V. Sacchini, "Intraoperative radiation

- therapy for breast cancer: Technical notes," *Breast J.* **9**(2), 106–112 (2003).
- ²²I. Brigger, C. Dubernet, and P. Couvreur, "Nanoparticles in cancer therapy and diagnosis," *Adv. Drug Delivery Rev.* **54**(5), 631–651 (2002).
- ²³J. Shen, L. Sun, and C. Yan, "Luminescent rare earth nanomaterials for bioprobe applications," *Dalton Trans.* ■, 5687–5697 (2008).
- ²⁴C. Vinegoni, D. Razansky, S. A. Hilderbrand, F. Shao, V. Ntziachristos, and R. Weissleder, "Transillumination fluorescence imaging in mice using biocompatible upconverting nanoparticles," *Opt. Lett.* **34**(17), 2566–2568 (2009).
- ²⁵E. S. M. Ali and D. W. O. Rogers, "Benchmarking EGSnrc in the kilovoltage energy range against experimental measurements of charged particle backscatter coefficients," *Phys. Med. Biol.* **53**(6), 1527–1543 (2008).
- ²⁶S. C. Davis, B. W. Pogue, H. Dehghani, and K. D. Paulsen, "Contrast-detail analysis characterizes diffuse optical fluorescence tomography image reconstruction," *J. Biomed. Opt.* **10**(5), 050501 (2005).
- ²⁷D. Hyde, R. Schulz, D. Brooks, E. Miller, and V. Ntziachristos, "Performance dependence of hybrid x-ray computed tomography/fluorescence molecular tomography on the optical forward problem," *J. Opt. Soc. Am. A Opt. Image Sci. Vis.* **26**(4), 919–923 (2009).
- ²⁸A. Li, E. L. Miller, M. E. Kilmer, T. J. Brunkhild, T. Chaves, J. Stott, Q. Zhang, T. Wu, M. Choriton, R. H. Moore, D. B. Kopans, and D. A. Boas, "Tomographic optical breast imaging guided by three-dimensional mammography," *Appl. Opt.* **42**(25), 5181–5190 (2003).
- ²⁹Z. Szucs-Farkas, F. R. Verdun, G. von Allmen, R. L. Mini, and P. Vock, "Effect of x-ray tube parameters, iodine concentration, and patient size on image quality in pulmonary computed tomography angiography: A chest-phantom-study," *Invest. Radiol.* **43**(6), 374–381 (2008).
- ³⁰D. W. Townsend, "Multimodality imaging of structure and function," *Phys. Med. Biol.* **53**(4), R1–R39 (2008).
- ³¹R. Weissleder and V. Ntziachristos, "Shedding light onto live molecular targets," *Nat. Med.* **9**(1), 123–128 (2003).
- ³²F. G. Blankenberg, "In vivo detection of apoptosis," *J. Nucl. Med.* **49**, 81S–95S (2008).

Intraoperative Imaging of Tumors Using Cerenkov Luminescence Endoscopy: A Feasibility Experimental Study

Hongguang Liu^{*1}, Colin M. Carpenter^{*2}, Han Jiang¹, Guillem Pratx², Conroy Sun², Michael P. Buchin³, Sanjiv S. Gambhir^{1,4}, Lei Xing², and Zhen Cheng¹

¹Molecular Imaging Program at Stanford (MIPS), Department of Radiology and Bio-X Program, Canary Center at Stanford for Cancer Early Detection, Stanford University, Stanford, California; ²Department of Radiation Oncology, Stanford University, Stanford, California; ³Stanford Photonics, Inc., Palo Alto, California; and ⁴Department of Bioengineering and Materials Science and Engineering, Stanford University, Stanford, California

Cerenkov luminescence imaging (CLI) is an emerging new molecular imaging modality that is relatively inexpensive, is easy to use, and has high throughput. CLI can image clinically available PET and SPECT probes using optical instrumentation. Cerenkov luminescence endoscopy (CLE) is one of the most intriguing applications that promise potential clinical translation. We developed a prototype customized fiberoptic Cerenkov imaging system to investigate the potential in guiding minimally invasive surgical resection. **Methods:** All experiments were performed in a dark chamber. Cerenkov luminescence from ¹⁸F-FDG samples containing decaying radioactivity was transmitted through an optical fiber bundle and imaged by an intensified charge-coupled device camera. Phantoms filled with ¹⁸F-FDG were used to assess the imaging spatial resolution. Finally, mice bearing subcutaneous C6 glioma cells were injected intravenously with ¹⁸F-FDG to determine the feasibility of in vivo imaging. The tumor tissues were exposed, and CLI was performed on the mouse before and after surgical removal of the tumor using the fiber-based imaging system and compared with a commercial optical imaging system. **Results:** The sensitivity of this particular setup was approximately 45 kBq (1.21 μ Ci)/300 μ L. The 3 smallest sets of cylindric holes in a commercial SPECT phantom were identifiable via this system, demonstrating that the system has a resolution better than 1.2 mm. Finally, the in vivo tumor imaging study demonstrated the feasibility of using CLI to guide the resection of tumor tissues. **Conclusion:** This proof-of-concept study explored the feasibility of using fiber-based CLE for the detection of tumor tissue in vivo for guided surgery. With further improvements of the imaging sensitivity and spatial resolution of the current system, CLE may have a significant application in the clinical setting in the near future.

Key Words: fiber-based imaging; Cerenkov luminescence endoscopy; Cerenkov luminescence imaging; radionuclides; optical imaging; PET

J Nucl Med 2012; 53:1–6

DOI: 10.2967/jnumed.111.098541

Cerenkov luminescence imaging (CLI) has recently [AQ1] attracted increasing interest in the field of molecular imaging (1,2). CLI is a new optical imaging modality in which images are obtained by monitoring the Cerenkov photons emitted from highly energetic moving charged particles (β^+ or β^-). Conventional nuclear imaging methods, such as PET and SPECT, are the most widely used clinical molecular imaging techniques. However, these modalities usually suffer from high cost, limited availability, relatively low spatial resolution, and low throughput (3). As a technique that bridges optical imaging and radionuclide imaging, CLI has shown many advantages such as high sensitivity, high resolution, low cost, wide availability, relatively high throughput, and commercially available radionuclide probes already approved by the Food and Drug Administration.

Since its discovery in 2009, CLI has quickly become a practical molecular imaging technique, and many new applications of CLI in preclinical research continue to emerge (1,2). Several research groups have demonstrated that CLI can be a powerful tool for tumor imaging using radionuclide probes such as ¹⁸F-FDG. Important validation studies have also been performed, and it was reported that there is a good linear correlation between the tumor uptake quantified by PET and tumor CLI signals in subcutaneous xenograft models (4–7). CLI has also been found to be useful for imaging α and pure β^- emitters such as ⁹⁰Y and ²²⁵Ac, which are used for cancer treatment (4). Moreover, CLI can be applied in the monitoring of reporter gene expression. The herpes simplex virus type 1 thymidine kinase and the sodium iodide symporter reporter genes were recently successfully imaged by CLI in conjunction with

Received Nov. 1, 2011; revision accepted May 2, 2012.

For correspondence or reprints contact either of the following: Zhen Cheng, Molecular Imaging Program at Stanford, Department of Radiology, Bio-X Program, Canary Center at Stanford for Cancer Early Detection, 1201 Welch Rd., Lucas Expansion, P095, Stanford University, Stanford, CA 94305. E-mail: zcheng@stanford.edu

Lei Xing, Department of Radiation Oncology, Stanford University School of Medicine, 875 Blake Wilbur Dr., Stanford, CA 94305-5847. E-mail: lei@stanford.edu

*Contributed equally to this work.

Published online ■■■■.

COPYRIGHT © 2012 by the Society of Nuclear Medicine and Molecular Imaging, Inc.

appropriate radioactive reporter probes (4,8,9). Cerenkov photons have also been used to illuminate fluorescent dyes and nanoparticles for in vivo imaging (10–13). A recent study further showed that CLI could be used for monitoring tumor surgery in xenograft mouse models, highlighting the translational potential of the modality (14). CLI has also been used to measure the radiochemical purity of a radiolabeled compound and to image plant physiology (15). In addition to these applications, the recent advancement in CLI tomography makes this novel imaging modality even more powerful and promising for biomedical research including diagnostic imaging and therapeutic monitoring (16–19).

Because it can image clinically available radiotracers, CLI has the potential to be rapidly translated into clinical applications (4,18). However, all the studies described above have involved the use of conventional small-animal optical imaging systems, which are not compatible with routine clinical practice. In this study, we have built the first, to our knowledge, prototype system that is amenable to Cerenkov luminescence endoscopy (CLE) in the clinic. This system comprises an optical fiber bundle and an intensified charge-coupled device (CCD) camera. The small-diameter flexible endoscope is designed for minimally invasive monitoring of living tissues and organs, using a sensitive camera to produce images of the radionuclide probe. It is also expected that hollow organs (e.g., bladder and lung) or insufflated cavities (e.g., esophagus and colon) inside the body can provide natural and anatomic dark chambers for CLE. By overlaying conventional bright-field images commonly obtained from an endoscope with the Cerenkov luminescence images generated by radionuclide probes, CLE could be used to identify diseased tissues for diagnostic purposes and real-time monitoring of endoscopic surgery.

Therefore, we investigated the feasibility of CLE for guiding cancer surgical resection by performing sensitivity, spatial-resolution, and proof-of-concept experiments. The characteristic sensitivity of this system was evaluated using the natural decay of ^{18}F -FDG. Imaging resolution was determined using a phantom with cylindrical holes. Finally, imaging studies were performed to demonstrate surgical guidance in a small-animal tumor model. A well-known commercial optical imaging system was used to provide a comparison. The data presented herein outline the instrumentation and methodology; further steps needed to translate this modality into the clinic are also discussed.

MATERIALS AND METHODS

^{18}F -FDG was produced by the Radiochemistry Facility at Stanford University. The rat glioma cell line C6 was obtained from American Type Culture Collection. Female athymic nude mice (*nu/nu*) ($n = 5$) obtained from Charles River Laboratories, Inc., were 4–6 wk old. A CRC-15R PET dose calibrator (Capintec Inc.) was used for all radioactivity measurements.

Tumor Model

All animal studies were performed in compliance with federal and local institutional guidelines for the conduct of animal experimentation. C6 cells were cultured in Dulbecco modified Eagle medium supplemented with 10% fetal bovine serum and 1% penicillin/streptomycin (Invitrogen Life Technologies). The cell line was maintained in a humidified atmosphere of 5% CO_2 at 37°C, with the medium changed every other day. A 75% confluent monolayer was detached with trypsin and dissociated into a single-cell suspension for further cell culture. Approximately 1×10^6 C6 cells suspended in phosphate-buffered saline (0.1 M, pH 7.2; Invitrogen) were implanted subcutaneously in the left legs of nude mice. Tumors were allowed to grow to 150–200 mm^3 (2–3 wk), and the tumor-bearing mice were imaged in vivo.

CLI

Validation CLI was performed with an IVIS Spectrum system (Caliper Life Science). For all in vivo studies, radionuclides were diluted in phosphate-buffered saline. Animals were placed in a light-tight chamber under isoflurane anesthesia. Each acquisition took 3 min for all studies without filters. Images were acquired and analyzed using Living Image 3.0 software (Caliper life sciences). The mice were kept fasting overnight before ^{18}F -FDG imaging and anesthetized by inhalation of 2% isoflurane during the experiment.

Fiber-Based CLE System

The fiber-based CLE system used an imaging optical fiber coupled to a highly sensitive intensified CCD camera. The application of this system for surgical oncology guidance is detailed in Figure 1. Specifically, a microimaging lens (Cinegon, F/1.4, 12-mm focal length; Schneider) was coupled at the distal end of an optical imaging fiber bundle that was 108 mm long, with a 5×6.7 mm active area. The pixels of the fiber bundle are made of discrete 10- μm fibers (IG154; Schott). At the proximal end, a Pentax (F/1.4) lens provided relay optics to the camera (Supplemental Fig. 1A; supplemental materials are available online only at <http://jnm.snmjournals.org>). The camera, an image-intensified

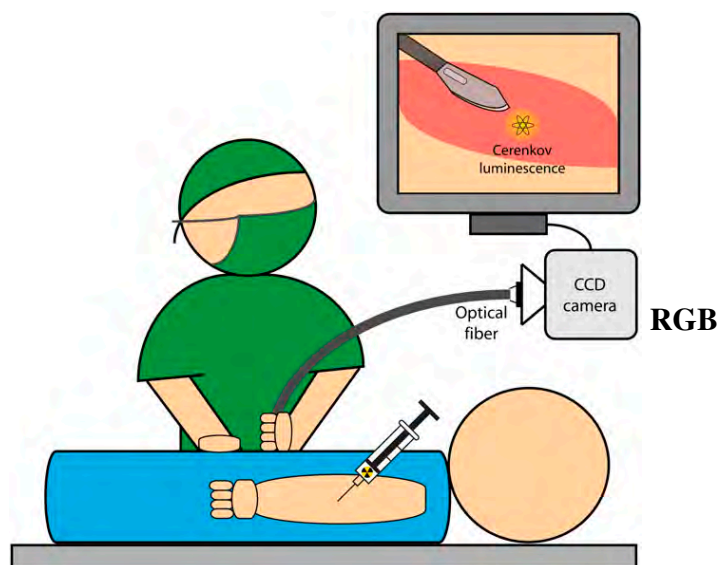


FIGURE 1. Suggested application for fiber-based system for endoscopic and laparoscopic CLI.

CCD (Turbo 640-Z; Stanford Photonics Inc.), had 640×480 pixels and single-photon imaging capability (Supplemental Fig. 1B). To minimize background light and to emulate a light-tight anatomic cavity, all images were taken in a dark box. In addition, images were postprocessed with a software thresholding technique that removed pixel values below a manufacturer-recommended value; this optimal value was chosen to remove low-intensity pixels that corresponded to thermal and read noise on the CCD. These steps reduced the noise to approximately 20 counts per second.

Imaging Using Fiber-Based System

Images were acquired at a high frame-rate of 120 Hz to allow for maximal reduction in noise. The noise-reduction step described above was performed for each frame. These frames were then accumulated for 5 min to form the raw data. The raw data were image-processed offline using an algorithm to remove cosmic and stray γ -events. This algorithm removed noisy pixels by thresholding the gradient around each pixel in its local area. An additional denoising step removed spurious bright pixels that appeared in sequential exposures.

The fiber-based CLE system was characterized for sensitivity by imaging 2 adjacent wells of a black 96-well plate (300 μ L per well). A glycerol and water mixture combined with 3.7 MBq (100 μ Ci) of ^{18}F -FDG was in 1 well, and a glycerol and water mixture only was in a nearby well. Images were sequentially acquired over approximately 10 half-lives (19 h, 43 min), and each data point was formed from 5 min of photon accumulation.

The spatial resolution of the system was characterized using a standard PET/SPECT phantom (Micro Hot-Spot Phantom; Data Spectrum Corp.) filled with 15.2 MBq (410 μ Ci) of ^{18}F -FDG; this phantom is also commonly used to evaluate the spatial resolution of PET systems. Both the 2.4- and the 1.6-mm cylindrical holes were used to form line profiles, taken from the fiber-based images. An ambient-light image and a functional Cerenkov luminescence image were acquired. The exposure time for all ambient images was less than 1 s, and the functional image acquisition time was 5 min. The subject was 5 cm from the optical system.

Fiber-Based CLE System for Surgery Monitoring

Five mice were injected with 37 MBq (1 mCi) of ^{18}F -FDG via the tail vein. The tracer was allowed to accumulate for 60–70 min, and the mice were imaged in the IVIS system to verify tumor uptake of ^{18}F -FDG. Tumors were then imaged with the IVIS and fiber-based CLE systems after removal of the skin covering the subcutaneous tumor and after excision of the tumor. To simulate an environment mimicking surgical resection, and to validate the origin of the signal, the excised tumor was also imaged after being placed adjacent to the surgical cavity. Two images were acquired for each of these steps: 1 ambient image and 1 functional Cerenkov luminescence image. The exposure time for all ambient images was less than 1 s, and the functional image acquisition time was 5 min.

Statistical Methods

Quantitative data were expressed as mean \pm SD. Means were compared using the Student *t* test. A 95% confidence level was chosen to determine the significance between groups, with *P* values of less than 0.05 indicating significant differences.

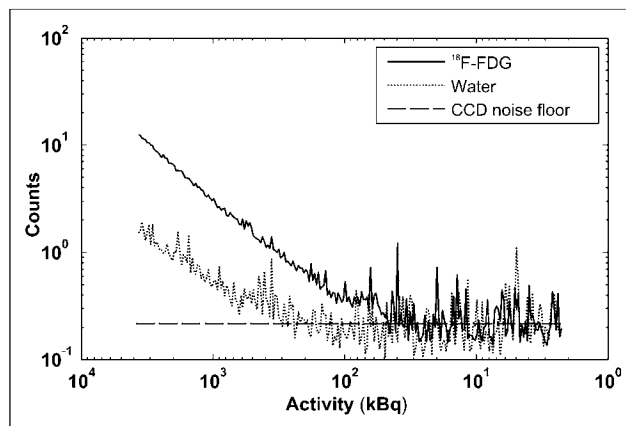


FIGURE 2. System sensitivity via sequential imaging of 3.7 MBq (100 μ Ci) of ^{18}F -FDG for approximately 20 h. Optical signals from ^{18}F -FDG and control sample were plotted.

RESULTS

System Characterization

Figure 2 shows the reduction in signal during ^{18}F -FDG decay over time for 2 wells: 1 filled with ^{18}F -FDG and 1 filled with a water and glycerol mixture only. With a 5-min integration time, a minimum of approximately 45 kBq (1.21 μ Ci) of activity can be identified as different from the control well containing the water and glycerol solution (signal-to-noise ratio > 1). There was a decrease in signal in the control well due to stray γ -photons from the ^{18}F -FDG well interacting with the optical fiber and creating scintillation background light in the image.

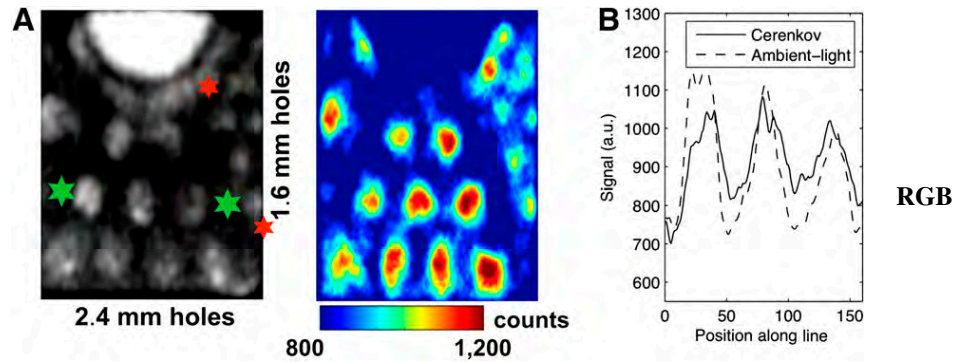
Visually, the photographic and Cerenkov images taken using the standard IVIS imaging system (Supplemental Fig. 2) are similar to the photographic and Cerenkov images taken with the fiber-based system (Fig. 3A). The line profiles demonstrate a high correlation between the Cerenkov and photographic line profiles. For the 2.4-mm holes (Fig. 3B), the line profile limits depicted by the large green stars in Figure 3A had a Pearson correlation coefficient of 0.78 (significance, $P < 1e-5$). For the 1.6-mm holes (Supplemental Fig. 3), the line profile limits depicted by the smaller red stars had a Pearson correlation coefficient of 0.71 (significance, $P < 1e-5$). The peaks were also in near-identical locations; the difference in peak locations between the holes for the line profiles of the photographic and Cerenkov-emission images was 3.8%, a difference of only a few pixels.

System Demonstration

The images comparing both systems before removal of the tumor for mouse 1 are shown in Figure 4 (IVIS system [Fig. 4] [Fig. 4A] and fiber-based CLE system [Fig. 4B]). Figure 5A [Fig. 5] shows the images produced by the IVIS system, and Figure 5B shows images from the fiber-based CLE system after removal of the tumor in mouse 1.

Comparing images in Figure 5B quantitatively, we determined the tumor-to-background ratio for the Cerenkov signal by computing the ratio of the median value in the

FIGURE 3. Characterization of fiberoptic system spatial resolution. (A) Respective ambient (left) and Cerenkov images (right) of PET/SPECT phantom (4.3-cm inner diameter). (B) Quantitative line profiles of ambient and Cerenkov images for 2.4-mm holes; line sampled is indicated by green stars in A. a.u. = arbitrary units.



region of interest encircling the excised tumor to the median value in the cleared tumor cavity. This ratio was 1.28 (for comparison, the tumor-to-background ratio from the IVIS system was 1.16 for the 3-min scan). For mice 2, 3, 4, and 5, the tumor-to-background ratios for the removed tumor were 1.41, 1.21, 1.02, and 1.17, respectively. Tumor tissue light emission was significantly higher than the exposed cavity for all mice (Student *t* test for paired samples, *P* < 0.05 for all). Much of the low tumor-to-background value in mouse 4 can be explained by the reflection of the light emitted from the tumor by the tumor cavity, which was directly adjacent. Residual tumor tissue after surgery is also possible.

DISCUSSION

In this study, we demonstrated the methodology and performance of an optical fiber system built to image tumor margins during surgical resection. Cerenkov imaging has been proposed for small-animal drug discovery and surgical guidance, yet previous studies have used an imaging box with a lens-mounted imaging system; this setup is not realistic for subjects that are larger (e.g., large animals and humans). ~~To our knowledge, this was the first study that investigated a Cerenkov endoscope for surgical resection.~~ We have shown that this system is capable of imaging 1.2-mm structures, using phantom experiments. We determined the sensitivity of the system for ^{18}F -FDG (~45 kBq [1.21 μCi]/300 μL). We then demonstrated the ability to visualize the accumulation of ^{18}F -FDG in a tumor using this system and could track the contrast as the tumor was excised from the mouse.

A benefit of a Cerenkov endoscope is that it provides higher image spatial resolution than PET and SPECT cameras, because the optical photons emitted from the tissue surface are detected with optical lenses and a high-resolution CCD chip. Cho et al. demonstrated a limit of 350 μm (in full width at half maximum) with a system designed for visualizing a microfluidic chip setup (26). This resolution is affected by the imaging system, the range of the β -particles in the tissue, and tissue optical scatter. Levin and Hoffman showed that the mean β -particle track of ^{18}F -FDG had a full width at half maximum value of 102 μm in water (27), which determines the physical resolution limit of a Cerenkov scope when imaging ^{18}F -

FDG. Improved resolution may be achieved using a radioisotope with a β -particle decay of lower energy, such as ^{131}I , although this would result in lower sensitivity because there is an inverse relationship between resolution and sensitivity. We do note some inconsistency in the image of the 1.2-mm holes, but many of these holes are clearly visualized. The high spatial resolution of the system requires accurate focus of the optics both at the distal fiber-lens junction and at the proximal fiber-camera junction—an optical focus that will be improved in our further studies. In the case of our phantom, the resolution of the Cerenkov luminescence images was also degraded by reflections within the translucent phantom and the signal-to-noise ratio of the single-photon-counting camera,

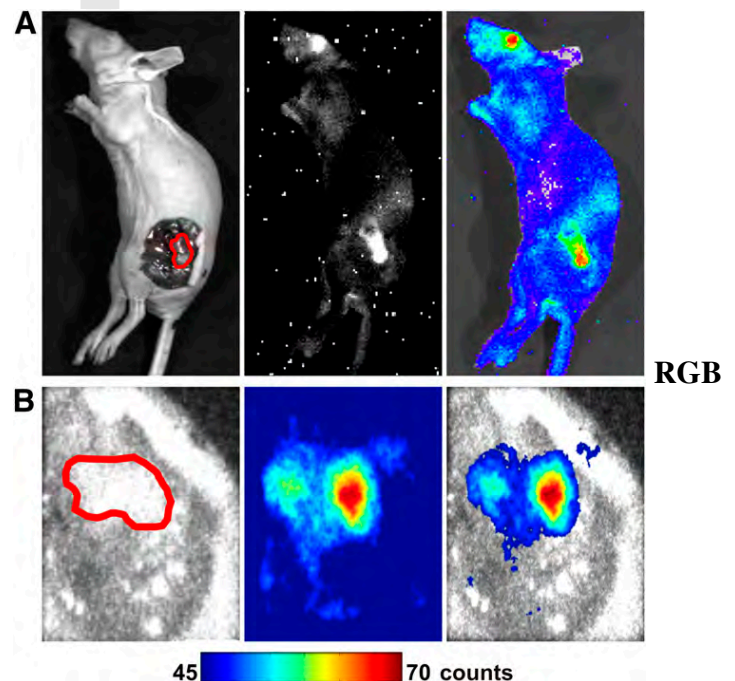


FIGURE 4. Mouse 1 bearing C6 glioma after tail-vein administration of 37 MBq (1 mCi) of ^{18}F -FDG. (A) Mouse was imaged by commercially available optical IVIS system, and images were compared with those from prototype fiber-based system (B). Tumor tissues are outlined by red lines. Ambient-light images are on left, luminescent images are in middle, and fused images are on right.

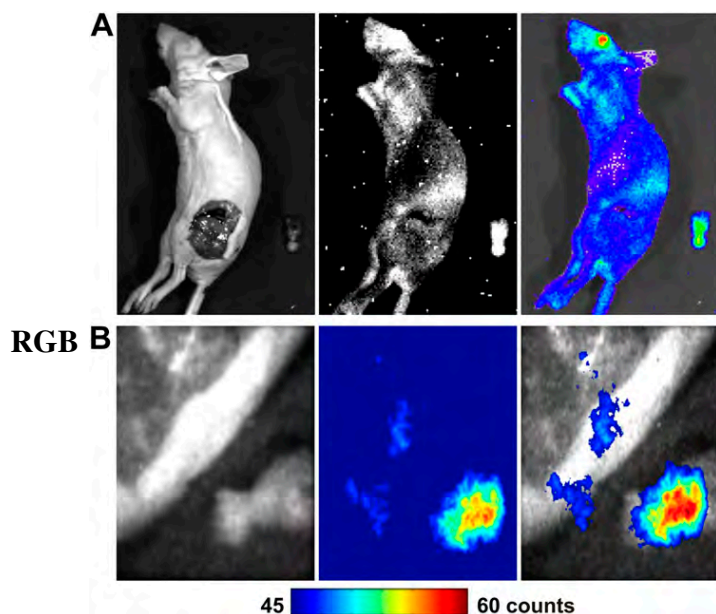


FIGURE 5. Mouse 1 was imaged by IVIS optical system (A) and fiber-based system (B) after surgery to remove tumor tissues. Ambient-light images are on left, luminescent images are in middle, and fused images are on right.

which was not entirely optimized. The signal-to-noise ratio of our ambient-light image was also affected by a slightly imperfect focus and the suboptimal settings of the illumination source and camera. Thus, although we demonstrated the ability to visualize many of these 1.2-mm cylindric holes in a phantom with this endoscope-based system, we expect to be able to image submillimeter lesions with a more optimized system.

The sensitivity limit of this system was 45 kBq (1.2 μ Ci)/300 μ L with ^{18}F -FDG. To put this in a practical perspective, if this system were used for head and neck tumors of the oropharynx (with a standardized uptake value of 5.17), 2.1 GBq (54 mCi) would have to be injected intravenously into a 70-kg patient to have enough activity to visualize a 300- μ g tumor (22) in a 5-min scan; a more sensitive scope would enable the identification of smaller structures or similar structures with a reduction in ionizing dose to the patient and clinical staff. Increased sensitivity may be realized with more sensitive optics (such as an F/0.95 lens) or fiber optic glass, which transmits farther into the violet and ultraviolet emissions. The fiberglass used in this experiment was Schott-75 glass, which transmits 40% light at 500 nm; thus, it is not optimized for detecting the short-wavelength-dominant Cerenkov emission. In addition, γ -photons emitted from the radiotracer scintillate impurities in the glass, resulting in undesired background noise. The use of fused silica, which is much more sensitive to the ultraviolet and violet emissions and has fewer impurities, would improve sensitivity.

As a prototype device, the off-the-shelf optical lens on this system was too large (3-cm diameter) for many

endoscopic or laparoscopic applications. However, smaller custom optics could be designed to enable imaging through smaller apertures. Meanwhile, optimized optic lenses and fibers can provide better sensitivity and shorter integration time in upcoming systems. We leave this investigation for future studies using more customized optical systems.

The main advantage of this system over other optical techniques, such as fluorescence imaging, is that it is able to use standard PET tracers, such as ^{18}F -FDG, which are already available in the clinic. Many novel tracers such as 3'-deoxy-3'- ^{18}F -fluorothymidine, engineered proteins, and labeled arginine-glycine-aspartic acid peptides are in the pipeline of clinical trials required by the Food and Drug Administration because of their utility in PET. This is a significant advantage for this technique, because much effort and innovation is being dedicated to PET tracers. In contrast, because of the lack of a standardized imaging device for optical imaging, optical contrast agents are not being sufficiently developed to keep pace with radiotracers. Thus, the main advantage of a Cerenkov emission surgical scope is that it is readily clinically translatable. The combination of PET and Cerenkov imaging provides an opportunity to use an identical signal origin, and perhaps an identical injection, to localize tumors for excision.

CONCLUSION

This proof-of-concept study demonstrated the feasibility of using fiber-based CLE for the detection of tumor tissue in vivo and demonstrated its potential use for image-guided surgery. With further improvement in imaging sensitivity and resolution of the current system, it is expected that Cerenkov imaging might soon be translated into clinical applications.

DISCLOSURE STATEMENT

The costs of publication of this article were defrayed in part by the payment of page charges. Therefore, and solely to indicate this fact, this article is hereby marked "advertisement" in accordance with 18 USC section 1734.

ACKNOWLEDGMENTS

We acknowledge support from the National Cancer Institute (NCI) (R01 CA128908), the National Institutes of Health (ICMIC P50CA114747), the Department of Defense Breast Cancer Postdoctoral Fellowship (W81XWH-11-1-0087, W81XWH-11-1-0070, and W81XWH-10-1-0506), the Center for Biomedical Imaging at Stanford, the Canary Foundation, and the Friends for an Earlier Breast Cancer Test. No other potential conflict of interest relevant to this article was reported.

REFERENCES

- Xu Y, Liu H, Cheng Z. Harnessing the power of radionuclides for optical imaging: Cerenkov luminescence imaging. *J Nucl Med*. 2011;52:2009–2018.
- Lucignani G. Cerenkov radioactive optical imaging: a promising new strategy. *Eur J Nucl Med Mol Imaging*. 2011;38:592–595.

3. Massoud TF, Gambhir SS. Molecular imaging in living subjects: seeing fundamental biological processes in a new light. *Genes Dev.* 2003;17:545–580.
4. Liu H, Ren G, Miao Z, et al. Molecular optical imaging with radioactive probes. *PLoS ONE.* 2010;5:e9470.
5. Robertson R, Germanos MS, Li C, Mitchell GS, Cherry SR, Silva MD. Optical imaging of Cerenkov light generation from positron-emitting radiotracers. *Phys Med Biol.* 2009;54:N355–365.
6. Boschi F, Calderan L, D'Ambrosio D, et al. In vivo ^{18}F -FDG tumour uptake measurements in small animals using Cerenkov radiation. *Eur J Nucl Med Mol Imaging.* 2011;38:120–127.
7. Ruggiero A, Holland JP, Lewis JS, Grimm J. Cerenkov luminescence imaging of medical isotopes. *J Nucl Med.* 2010;51:1123–1130.
8. Liu H, Ren G, Liu S, et al. Optical imaging of reporter gene expression using a positron-emission-tomography probe. *J Biomed Opt.* 2010;15:060505.
9. Jeong SY, Hwang MH, Kim JE, et al. Combined Cerenkov luminescence and nuclear imaging of radioiodine in the thyroid gland and thyroid cancer cells expressing sodium iodide symporter: initial feasibility study. *Endocr J.* 2011;58:575–583.
10. Liu H, Zhang XF, Xing BG, Han PZ, Gambhir SS, Cheng Z. Radiation-luminescence-excited quantum dots for in vivo multiplexed optical imaging. *Small.* 2010;6:1087–1091.
11. Dohager RS, Goiffon RJ, Jackson E, Harpstrite S, Pivnicka-Worms D. Cerenkov radiation energy transfer (CRET) imaging: a novel method for optical imaging of PET isotopes in biological systems. *PLoS ONE.* 2010;5:e13300.
12. Lewis MA, Kodibagkar VD, Oz OK, Mason RP. On the potential for molecular imaging with Cerenkov luminescence. *Opt Lett.* 2010;35:3889–3891.
13. Sun C, Pratz G, Carpenter CM, et al. Synthesis and radioluminescence of PE-Glylated $\text{Eu}(3+)$ -doped nanophosphors as bioimaging probes. *Adv Mater.* 2011;23:H195–H199.
14. Holland JP, Normand G, Ruggiero A, Lewis JS, Grimm J. Intraoperative imaging of positron emission tomographic radiotracers using Cerenkov luminescence emissions. *Mol Imaging.* 2011;10:177–186.
15. Park JC, An GI, Park SI, et al. Luminescence imaging using radionuclides: a potential application in molecular imaging. *Nucl Med Biol.* 2011;38:321–329.
16. Hu Z, Liang J, Yang W, et al. Experimental Cerenkov luminescence tomography of the mouse model with SPECT imaging validation. *Opt Express.* 2010;18:24441–24450.
17. Li C, Mitchell GS, Cherry SR. Cerenkov luminescence tomography for small-animal imaging. *Opt Lett.* 2010;35:1109–1111.
18. Spinelli AE, Kuo C, Rice BW, et al. Multispectral Cerenkov luminescence tomography for small animal optical imaging. *Opt Express.* 2011;19:12605–12618.
19. Xu Y, Chang E, Liu H, Jiang H, Gambhir SS, Cheng Z. Proof-of-concept study of monitoring cancer drug therapy with Cerenkov luminescence imaging. *J Nucl Med.* 2012;53:312–317.
20. Cho JS, Taschereau R, Olma S, et al. Cerenkov radiation imaging as a method for quantitative measurements of beta particles in a microfluidic chip. *Phys Med Biol.* 2009;54:6757–6771.
21. Levin CS, Hoffman EJ. Calculation of positron range and its effect on the fundamental limit of positron emission tomography system spatial resolution. *Phys Med Biol.* 1999;44:781–799.
22. Allal AS, Slosman DO, Kebdani T, Allaoua M, Lehmann W, Dulguerov P. Prediction of outcome in head-and-neck cancer patients using the standardized uptake value of 2-[^{18}F]fluoro-2-deoxy-d-glucose. *Int J Radiat Oncol Biol Phys.* 2004;59:1295–1300.

V1